ΕΘΝΙΚΟ ΚΑΙ ΚΑΠΟΔΙΣΤΡΙΑΚΟ ΠΑΝΕΠΙΣΤΗΜΙΟ
ΑΘΗΝΩΝ

ΜΕΤΑΠΤΥΧΙΑΚΗ ΔΙΠΛΩΜΑΤΙΚΗ ΕΡΓΑΣΙΑ

“Mercury- and silver-rich sphalerite from modern seafloor polymetallic mineralization, Kolumbo shallow-submarine arc-volcano, Santorini,Greece: deposition model and environmental significance”

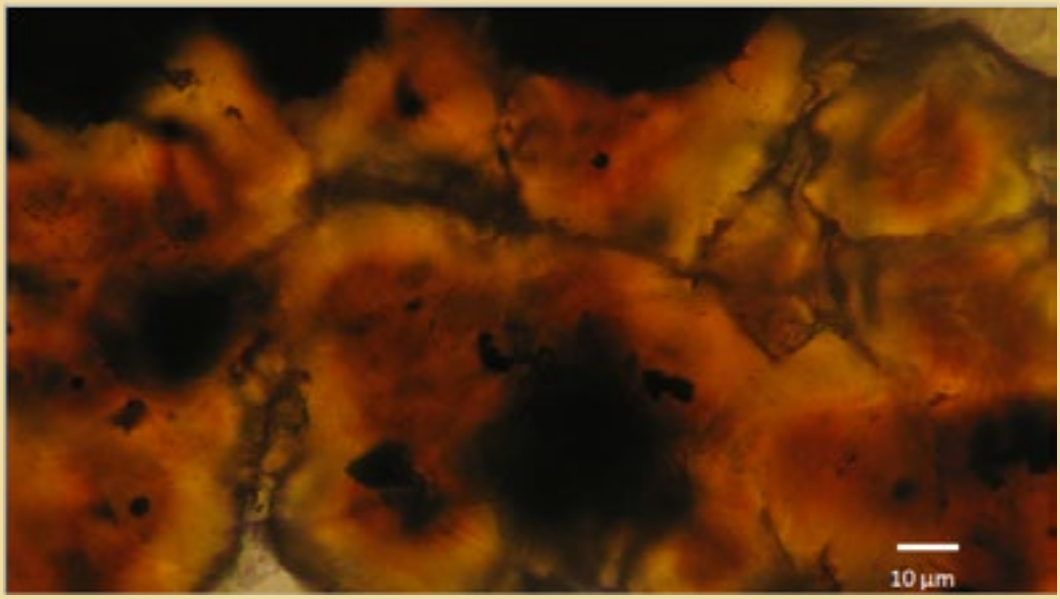

ΜΑΡΙΑ -ΔΕΣΠΟΙΝΑ ΧΡΥΣΑΦΕΝΗ ©

ΕΠΙΒΛΕΠΩΝ:

ΣΤΕΦΑΝΟΣ ΚΙΛΙΑΣ,
Καθηγητής Ε.Κ.Π.Α.

ΕΞΕΤΑΣΤΙΚΗ ΕΠΙΤΡΟΠΗ:

Αριάδνη Αργυράκη
Αναπληρώτρια Καθηγήτρια Ε.Κ.Π.Α.

Ηλίας Χατζηθεοδωρίδης
Αναπληρωτής Καθηγητής Ε.Μ.Π.Α.

ΑΘΗΝΑ , ΦΕΒΡΟΥΑΡΙΟΣ 2016

ΕΘΝΙΚΟ ΚΑΙ ΚΑΠΟΔΙΣΤΡΙΑΚΟ ΠΑΝΕΠΙΣΤΗΜΙΟ ΑΘΗΝΩΝ

ΣΧΟΛΗ ΘΕΤΙΚΩΝ ΕΠΙΣΤΗΜΩΝ
ΤΜΗΜΑ ΓΕΩΛΟΓΙΑΣ ΚΑΙ ΓΕΩΠΕΡΙΒΑΛΛΟΝΤΟΣ

ΠΡΟΓΡΑΜΜΑ ΜΕΤΑΠΤΥΧΙΑΚΩΝ ΣΠΟΥΔΩΝ
"ΕΦΑΡΜΟΣΜΕΝΗ ΠΕΡΙΒΑΛΛΟΝΤΙΚΗ ΓΕΩΛΟΓΙΑ"

ΜΕΤΑΠΤΥΧΙΑΚΗ ΔΙΠΛΩΜΑΤΙΚΗ ΕΡΓΑΣΙΑ

"Mercury- and silver-rich sphalerite from modern seafloor polymetallic mineralization, Kolumbo shallow-submarine arc-volcano, Santorini,Greece: deposition model and environmental significance"

© ΜΑΡΙΑ -ΔΕΣΠΟΙΝΑ ΧΡΥΣΑΦΕΝΗ

ΕΠΙΒΛΕΠΩΝ:
ΣΤΕΦΑΝΟΣ ΚΙΛΙΑΣ,
Καθηγητής Ε.Κ.Π.Α.

ΕΞΕΤΑΣΤΙΚΗ ΕΠΙΤΡΟΠΗ:

Αριάδνη Αργυράκη
Αναπληρώτρια Καθηγήτρια Ε.Κ.Π.Α.

Ηλίας Χατζηθεοδωρίδης
Αναπληρωτής Καθηγητής Ε.Μ.Π.Α.

ΑΘΗΝΑ, ΦΕΒΡΟΥΑΡΙΟΣ 2016

I hereby declare that I am the sole author of this Thesis.

I authorize the National and Kapodistrian University of Athens to display the whole Thesis text on the web.

MARIA-DESPOINA CHRYSAFENI

ABSTRACT

The active hydrothermal vent field on the floor of the Kolumbo shallow-submarine arc-volcano, near Santorini, Hellenic volcanic arc features striking bulk enrichment of polymetallic spires in trace metals of economic and environmental importance: Sb, Tl, Hg, As, Au, Ag, Pb and Zn indicating a new hybrid seafloor analogue of epithermal-to-volcanic-hosted-massive-sulfide deposits. The Kolumbo submarine hydrothermal vent field marks an Hg and Ag geochemical anomaly compared to the only three reports of low Hg and Ag concentrations in the Hellenic Volcanic Arc.

Sphalerite is an important host mineral for a wide range of minor and trace elements. We have used Environmental Scanning Electron Microscopy (ESEM) and electron microprobe analyses (EMPA) to investigate the distribution of Hg, Ag, Pb, Sb, As, Cd and Cu in samples from the active hydrothermal vent field of Kolumbo (Santorini) submarine volcano. The samples consist predominantly of pyrite/marcasite, barite, sphalerite, galena, unidentified Sb-Pb sulfosalts and opal. Additionally, rare stibnite and an unidentified non-stoichiometric Zn-sulfide phase were also detected, for the first time. Mercurian (Hg) and argentiferous (Ag) sphalerite was detected for the first time in the Hellenic Volcanic Arc, in shallow seafloor (~500 mbsl) hydrothermal vent edifices (i.e. chimneys, mounds etc.) of the active hydrothermal vent system of Kolumbo shallow-submarine arc-volcano.

The bulk trace metal enrichment of Hg and Ag in the chimneys is controlled by the modal abundance of sphalerite and its modifications that accompany the course of dissolution–reprecipitation processes during evolving hydrothermal activity and chimney growth. Kolumbo sphalerite occurs in three textural varieties, interpreted as a result of increasing maturity following dissolution–reprecipitation processes within the vent edifices during hydrothermal evolution of the chimney mineralogy. They are designated as Types 1 to 3, and represent different generations which in order of increasing maturity are: i) Type1: microglobular and zoned colloform sphalerite, ii) Type 2: sphalerite with porous core and massive rim and iii) Type 3: inclusion-rich and compositionally zoned massive sphalerite.

Mercury (Hg) correlates closely with Cd in sphalerite and the distribution of Hg in sphalerite is probably controlled by: (i) Direct substitutions of divalent cations as $Zn^{2+} \leftrightarrow (Hg^{2+}, Cd^{2+})$ along systematic growth zones in primary colloform type 1 sphalerite, possibly due to variable solubility of Hg during sphalerite growth due to changes in the

physicochemical parameters of the discharging fluid phase; and, (ii) inclusions of sulfosalt micro-particles of Hg and Cd in sphalerite 3 following dissolution-reprecipitation mechanisms; these particles which are visible in BSE images, probably represent solid inclusions of the ZnS–HgS solid solution series incorporated in sphalerite.

Silver (Ag) correlates with Cu-As-Sb-Pb. Its distribution is controlled by micro-, and/or nano-inclusions of galena–tetrahedrite–tennantite (galena–'fahlore') associations [PbS─$(Cu,Ag)_{10}(Fe,Zn)_2(As,Sb)_4S_{13}$]. Moreover, the strong co-variation between Ag and Sb along geochemical profiles in sphalerite 2 and 3 can also be explained by coupled substitution in the sphalerite lattice: $2Zn^{2+} \leftrightarrow Ag^{+}+Sb^{3+}$, alongside nano-scale inclusions of Ag–Sb-bearing tetrahedrite-tennantite.

We conclude that fluid temperature variations, boiling subseafloor and during venting processes and possibly variable amounts of fluid-seawater mixing represent important variables controlling the distribution of Hg and Ag in the submarine hydrothermal systems and associated sulfide deposits.

Table of Contents

ABSTRACT 1

Acknowledgements 5

LIST OF TABLES 6

LIST OF FIGURES 7

LIST OF ABBREVIATIONS 19

1. Introduction 20

2. Scope of thesis 26

3. Previous work 27

3.1 Sphalerite as a carrier of Hg and Ag 27

3.1.1 Mercury(Hg)- and Silver(Ag)-rich sphalerite from the modern ocean-floor 29

3.2 Hg in the geoenvironment: what we know and what we don't know 30

3.2.1 The international scene: Health concerns and related Hg-reduction policies 30

3.2.2 Emissions of Hg to the atmosphere 32

3.2.3 Hg in terrestrial ore deposits 36

3.2.4 Hg bioaccumulation in the marine environment 40

3.3 Silver in the geoenvironment: what we know and what we don't know 41

3.3.1 Health effects caused by silver 42

3.3.2. Silver in marine/submarine hydrothermal systems 42

3.3.3 Silver occurrence in the environment 43

3.3.4 Transport of silver in magmatic-hydrothermal systems 44

3.3.5 Silver bioaccumulation 45

4. Hg and silver in the unique shallow–submarine volcano, Kolumbo (Santorini), Hellenic Volcanic Arc (HVA) 46

4.1 Geodynamic and geological setting of the HVA 46

4.2 The Kolumbo submarine volcano and hydrothermal system 49

4.2.1 Kolumbo volcanic field 49
4.2.2 Kolumbo hydrothermal field 52
5. Materials and methods 53
5.1 Sampling 54
5.2 Sample preparation 57
5.3 Analytical methods 57
6. Results 60
6.1. Mineralogy and sphalerite textures of the 'Inner Sulfide-Sulfate Core' (ISSC) 60
6.1.1. Type 1: Microglobular and colloform zoned sphalerite 65
6.1.2. Type 2: Zoned sphalerite with porous core and massive rim 71
6.1.3. Type 3: Inclusion-rich and compositionally zoned massive sphalerite 78
6.2. Quantitative EPMA analysis, compositional mapping and element distribution and correlation trends of sphalerite type 3 80
7. Discussion 94
7.1 Structural and chemical variation of sphalerite crystals and control of trace element distribution 94
7.2. Trace elements in sphalerite: element substitution versus micro-, and/or nano-inclusions 98
7.3 Genetic considerations 100
7.3.1. Mechanisms of sphalerite precipitation 101
7.3.2 Effects of phase separation and metal complexation on sphalerite composition 102
7.4 Environmental considerations 104
8. Conclusions 105
References 107
Internet Sources 127
Appendix 127

Acknowledgements

I would like to express my deep gratitude to my dedicated supervisor, Professor Stephanos Kilias for his patient guidance, enthusiastic encouragement and useful critiques of this Master thesis. I would also like to thank my Professors Ariadne Argyraki (National and Kapodistrian University of Athens) and Elias Chatzitheodoridis (National Technical University of Athens) for their support and helpful indications.

I would also like to extend my thanks to Dr. Magnus Ivarsson of the Swedish Museum of Natural History, for assistance with ESEM-WDS, Optical Microscopy at Stockholm University and the Swedish Museum of Natural History. At this point I wish to thank Marianne Ahlbom, operator of the Environmental Scanning Electron Microscope and Dr. Curt Broman for the Raman spectroscopy analyses, from the Department of Geological Sciences in Stockholm University, and professor Henrik Skogby for the X-Ray Diffraction analyses at the Swedish Museum of Natural History.

I am grateful for the useful advice and general help of Dr. Paraskevi Nomikou, Assistant Professor, and I also thank the M.Sc student Danae Labridou for helping me with the bathymetric map. In addition, I would like to thank the director of the Department of Mineral Natural Resources in the Institute of Geological and Mineral Researches, George Oikonomou, for his kind and prompt support for the preparation of the polished thin sections and blocks, and Pantelis Patsis for carrying out the aforementioned process.

Last but not least, I would like to thank Dr. Paraskevi Polymenakou for contributing the samples and SeaBioTech program for funding the sampling campaign.

My special thanks go to my parents for supporting me in various ways as without their contribution my further education and consequently this thesis, would not have been possible. Finally, I would like to thank my close friends for the constant encouragement and emotional help to accomplish this thesis.

LIST OF TABLES

Table 1 IMA recognized Hg-minerals **(Hazen et al. 2012)**……. 39

Table 2 List of samples used for mineralogical study in this M.Sc. thesis…… 59

Table 3 Single EPMA analyses showing the concentrations (wt %) of the elements contained in the Zn-rich sulfide phase. Spots of EPMA analyses are represented by crosses accompanied by "Spectrum +number X" designation (Fig. 27)……. 64

Table 4 EMPA main results from the microglobular and colloform zoned sphalerite (type 1). Minimum, maximum, mean, corresponding standard deviation (1σ SD), and limit of detection (LOD) are presented…..…… 68

Table 5 EPMA main results for zoned sphalerite with porous core and massive rim (Type 2). Minimum, maximum, mean, corresponding standard deviation (1σ SD), and limit of detection (LOD) are presented ……..… 74

Table 6 EMPA main results from the massive sphalerite and the compositionally zoned massive sphalerite (type 3). Minimum, maximum, mean, corresponding standard deviation (1σ SD), and limit of detection (LOD) are presented. …… 83

Table 7 EMPA-WDS main results of Hg from the Hg-Cd sulfosalt inclusions of massive sphalerite (type 3) in samples SB-3-E and SB-7-A. Minimum, maximum, mean, corresponding standard deviation (1σ SD), and limit of detection (LOD) are presented.……..……. 84

Table 8 Single EPMA analyses showing the element concentrations (wt %) of the core, sector and rim of zoned, massive type 3 sphalerite. The points of analysis are shown in Figure 60a…….…… 85

LIST OF FIGURES

Figure 1 Geochemical spidergram comparing the Kolumbo vent samples with other seafloor hydrothermal deposits from various tectonic settings (modified after **Kilias et al. 2013**). Concentrations are normalized to Upper Continental Crust (UCC) **(Rudnick & Gao 2003)** for selected noble (Ag, Au), potentially life-essential (Cu, Zn) and potentially toxic (Sb, Hg, Cd, As, Tl) elements. The average and maximum concentrations of Tl (510 ppm and >1,000 ppm respectively) and Sb (8,333 ppm and 2.2 wt %, respectively) are among the highest reported from modern seafloor hydrothermal systems. Average Sunrise deposit **(Iizasa et al. 1999)**, Sunrise Myojin knoll **(Hannington et al. 2005)**, Sunrise Myojinsho **(Hannington et al. 2005)**, Sunrise Sujo Seamount **(Hannington et al. 2005)**, Brothers **(Hannington et al. 2005)**, Rumble II **(Hannington et al. 2005)**, Average JADE site **(Glasby et al. 2008)**, Izena cauldron **(Hannington et al. 2005)**, Average JADE **(Halbach et al. 1989)**, Franklin Seamount **(Hannington et al. 2005)**, Tyrrhenian sea Palinuro **(Hannington et al. 2005)**, Tyrrhenian sea Palinuro mean **(Dekov & Savelli 2004, Tufar 1991)**, Lake Taupo massive sulfides **(de Ronde 2002)**, Lake Taupo pseodochimney **(de Ronde 2002)** Lake Taupo red-yellow material (de Ronde 2002), Conical seamount-mineralized samples average **(Petersen et al. 2002)**, Conical seamount gold-rich samples average **(Petersen et al. 2002)**..... 22

Figure 2 Upper Continental Crust (UCC)-normalized (according to **Rudnick and Gao (2003)**) spidergram of trace elements in marine hydrothermal precipitates of the Hellenic Volcanic Arc. Average values of Methana siliceous sediments **(Huebner et al. 2004)**: red thick line and solid square; Average values of Methana carbonate sediments **(Huebner et al. 2004)**: darker red-brown thick line and solid lozenges; Milos Island sediment **(Cronan & Varnavas 2001, Varnavas & Cronan 2005)**: blue thick line and plus symbol correspond to Voudia Bay samples, light blue thick line and asterisk in lighter blue background correspond to Palaeochori, dark blue thick line and cross correspond to Rivari, respectively; Yali Island (Yali Bay) sediments **(Varnavas & Cronan 1991, 2005)**: gray thick line and open circle; Kos Island

(Kephalos Bay) sediments **(Rudnick & Gao 2003)** gray thick line and closed circle; Average values of Santorini caldera metalliferous marine sediments **(Varnavas & Cronan 1988)**: green thick line and open triangle correspond to Nea Kameni islet, light green thick line and closed triangle correspond to Palaea Kameni islet, yellow thick line and green triangles with yellow filling color correspond to Santorini "channel" situated between Palaea and Nea Kameni islets **(Gamaletsos et al. 2013)**…… 23

Figure 3 Log/log plot of Ag versus Au, showing a positive correlation **(Kilias et al. 2013-Supplementary information)**……..…..… 24

Figure 4 Crystal structures of the two main forms of ZnS, showing the tetrahedral relationship between Zn and S atoms. A. Cubic structure of sphalerite. B. Hexagonal structure of wurtzite **(Images reproduced from Wikipedia)**…….. 25

Figure 5 Relative contributions of estimated Hg emissions to the atmosphere from natural sources **(Varekamp & Buseck 1986)**…… 33

Figure 6 Relative contributions of estimated Hg emissions to the atmosphere from current anthropogenic sources **(Varekamp & Buseck 1986)**…….. 34

Figure 7 Spatial distribution of anthropogenic Hg emissions to the atmosphere for the year 2000 **(Pacyna et al. 2005, Selin et al. 2009)**…….…… 35

Figure 8 Relative contributions of estimated Hg emissions to the atmosphere from historical anthropogenic sources **(Friedli et al. 2009)**..... 36

Figure 9 Silver input to the environment from industrial applications. The arrow sizes indicate the total amount of silver flowing to each environmental receiver **(Urcell & Eters 1998)**…… 44

Figure 10 Location of study area in the center of the Aegean Volcanic Arc. The modern Aegean volcanic arc is developed behind the Hellenic Arc, the Peloponnese–

Crete island arc and the Cretan back-arc basin. The African plate to the south subducts beneath the Eurasian plate to the north along the red lines just to the south of Crete. Yellow arrows indicate the GPS rates (approximately 40 mm/y) of the Aegean towards the African plate (considered stable) (modified after **Nomikou et al. 2013**).……..……...……. 47

Figure 11 Geodynamic setting of the Santorini - Kolumbo volcanic field. (a–d): Schematic cartoons of different geodynamic environments where seafloor hydrothermal vents occur. (a) Mid-Ocean Ridges along divergent plates. (b) Intra-Oceanic Arcs within convergent boundaries (e.g. Philippines). (c) Marginal back-arc basins and island arcs along active continental margins with oceanic subduction (e.g. Japan). (d) ‘‘Hellenic Subduction System’’. The ‘‘Hellenic Volcanic Arc’’, within active continental margin, developed behind the molassic back-arc basin, hosted over thinned continental crust. (e) Swath bathymetry map of Santorini-Kolumbo volcanic field (modified after ref. 5-permission to publish the original map was provided by Elsevier Science) and location of the geological transect (red line). (f) Schematic cartoon depicting the geological cross section through the Hellenic Volcanic Arc, from the molassic back-arc Cretan Basin to the Cycladic island of Ios in the back-arc area **(Kilias et al. 2013)**.……..…….. 48

Figure 12 Swath bathymetry map of Christianna-Santorini-Kolumbo volcanic field (CSK) and tectonic zone (red line) **(Nomikou et al. 2013)**.…..…… 49

Figure 13 Swath bathymetry of Kolumbo volcano (modified after **Nomikou et al. 2013**). (The red square is the area of which a detailed bathymetric map of Kolumbo hydrothermal vent field is given in Figure 16)……..…….. 51

Figure 14 SW-NE striking multi-channel reflection seismic profile across Kolumbo. Upper part shows seismic data, lower part shows interpretation. Grey shaded area smark pyroclastic flows or mass-transport deposit. K1-K5: the five circular stratigraphic units labeled bottom-up. SK3 and SK4 refer to intercalated units. VC: Volcanic Cone. VC numbers according to **Nomikou et al. (2013)**. **(Hübscher et al. 2015)**. ……. 51

Figure 15 a. “Politeia Vent Complex”: Field of multiple inactive and active sulfide/sulfate, spires up to 2 m high on top of a hydrothermal mound with spire fragments draped by Fe-bearing bacterial mats. Clear fluids vent from active spires (not visible). b. “Champagne Vent Complex”: Active high-temperature (220°C) vent discharging both gases (>99 % CO_2) and fluids. c. “Diffuser II Vent Complex”: Vent with bacterial covering and gas bubbling. d. “Poet’s Candle”: The largest observed (height ~ 4 m) inactive vent with bacterial covering **(Kilias et al. 2013)**. e. Sulfide/sulfate spire on the top of a hydrothermal mound from the vent V16b. f. Vent with slight gas discharging from V08. g. Vent displaying gas bubbling from V59(2). h. Active vent discharging gases and fluids from the vent V65 (for vent location see Figure 16)…….…... 53

Figure 16 Detailed bathymetric map of Kolumbo hydrothermal vent field located in the northern part of the crater floor (red square in Figure 13) (modified after **Kilias et al. 2013**), with the locations of hydrothermal vents, Politeia, Champagne and Diffuser II, and the samples studied in this MSc thesis along with ex situ photographs immediately after recovery from the sea. ……. 54

Figure 17 Ex-situ photographs of broken off and/or sectioned parts (SB-3-D, SB-3-E, SB-3-F) of sample SB-3 with marked bottom-up growth orientation. (a) Samples SB-3-D and SB-3-E represent the ISSC zone. (b) Sample SB-3-F is the top part of this hydrothermal chimney. (c) Individual samples assembled together to represent original positions in chimney sample SB-3. The brown exterior surface of the samples represents the OAsL zone.…..……..... 55

Figure 18 Ex-situ photograph of sectioned chimney sample SB-7-A representing the ISSC zone.…… 55

Figure 19 Ex-situ photographs of the hydrothermal spire sample No. SB-9 showing (a) the whole sample which is covered by the OAsL zone (i) while its interior represents the ISSC zone (ii); (b) its massive sulfide (ISSC)-dominated basal part of spire. …… 56

Figure 20 Ex-situ photographs of the hydrothermal chimney sample SB-10-A showing (a) the whole sample in which the zone ISSC (i) dominates and (b) its base with a thin orange rim of the OAsL zone (ii)....…….. 56

Figure 21 Ex-situ photographs of the hydrothermal chimney sample SB-12-A showing (a),(b) different aspects from the whole sample coated by the OAsL zone (i) while its interior consists of massive sulfide core (ISSC zone) (ii) and (c) its massive sulfide base (ISSC zone) (ii) with open-space filling barite crystals (Ba).…….... 56

Figure 22 Photomicrographs of commonly seen textures in the inner sulfide-sulfate core (ISSC). Transmitted light microphotograph (TLP) of (a) barite (Ba) laths and rosettes forming the substrate for disseminated colloform zoned sphalerite (Sph) (oil lens and // Nichols). (b) pyrite/marcasite (Py) microglobules and colloform zoned sphalerite (Sph) overlaying barite (Ba) matrix (oil lens and // Nichols). (c) Reflected light microphotograph (RLP) of anhedral Sb-Pb-sulfosalt inclusions in concentrically laminated pyrite/marcasite (Py), mantled by barite laths (Ba) and anhedral sphalerite (Sph) with scattered Sb-Pb-sulfosalts inclusions (oil lens and // Nichols). (d) Reflected light microphotograph (RLP) of As-sulfides (As-S) overgrowing barite (Ba) blades along their edges (oil lens and crossed Nichols)..……..... 61

Figure 23 Photomicrographs of commonly seen textures in the inner sulfide-sulfate core (ISSC). Reflected light microphotograph (RLP) of (a) finely concentrically laminated spheroids of pyrite/marcasite (Py) mantled by anhedral to subhedral intergrowths of Sb-Pb-sulfosalts and sphalerite (Sph) (oil lens and // Nichols). (b) Concentrically laminated spheres of pyrite/marcasite (Py) surrounded by sphalerite (Sph) with inclusions of Sb-Pb-sulfosalts (oil lens and // Nichols). (c) Finely laminated pyrite-marcasite fabric with (micro)stromatolitic morphology (oil lens and // Nichols). (d) Radial rim of pyrite/marcasite encircling concentrically banded, radial, spheroidal masses of pyrite/marcasite (oil lens and // Nichols). (e) Anhedral porous, pyrite/marcasite

spongy rims around concentrically laminated pyrite/marcasite (oil lens and // Nichols)……..... 62

Figure 24 ESEM photographs of (a) anhedral galena (Gn) with anhedral sphalerite (Sph) and intricate closely packed, colloform banded pyrite/marcasite (Py) fabric. (b) Galena rim (Gn) encircling concentrically laminated spheroid of pyrite/marcasite (Py). (c) Anhedral inclusions of galena (Gn) into anhedral sphalerite (Sph). (d) ESEM backscatter image showing anhedral galena (points 7a213 and 7a216), with spherical pyrite (point 7a215) and barite blades (point 7a214) .…… 63

Figure 25 ESEM backscatter images of (a), (b) stibnite fibers (noted green points) with barite blades (Ba). (c) anhedral to subhedral and fibrous stibnite in open space……..... 63

Figure 26 ESEM backscatter image showing anhedral Sb-Pb-sulfosalts inclusions (noted green) into laminated concentric spheres of pyrite/marcasite …… 64

Figure 27 ESEM photograph of biomorphous bundles of unidentified Zn-rich sphalerite-like sulfide phase..…… 64

Figure 28 ESEM photograph of sphalerite (Sph) colloform microglobules (Type 1)…… 65

Figure 29 Transmitted light microphotograph (TLP) of colloform zoned sphalerite (Type 1) (oil lens and //Nichols).…….. 65

Figure 30 Raman analyses of the dark red (1) and yellow zones (2) of microglobular and colloform zoned sphalerite, compared with Raman spectra of (a) pure sphalerite **(http://rruff.info)**, (b) Cd-rich sphalerite **(Kharbish 2007)** and (c) sphalerite containing Fe **(http://rruff.info)**.……..... 66-67

Figure 31 Histogram showing the variation in Fe in sphalerite type 1 from Kolumbo hydrothermal precipitates……..…… 67

Figure 32 Histogram showing the variation in Sb in sphalerite type 1 from Kolumbo hydrothermal precipitates. ……. 68

Figure 33 Energy dispersive spectroscopy map of colloform zoned sphalerite (Sph) for Hg, Cd, Sb, Fe, S, Cu, Zn ..…….... 69

Figure 34 Binary correlation plots of (a) Zn vs. Fe, (b) Zn vs. Sb, (c) Zn vs. Cu, (d) Zn vs. Cd, (e) Zn vs. As, (f) Zn vs. Ag, in microglobular and colloform zoned sphalerite (Type 1)……..…….……. 70

Figure 35 ESEM photograph of type 2 sphalerite with porous core (pSph) and massive rim (mSph) with voids (dark). The latter contains randomly distributed galena (Gn) inclusions....……..……..….. 71

Figure 36 ESEM photograph showing the association between sphalerite type 2 and pyrite (Py), galena (Gn) and opal (Opl)…… 71

Figure 37 BSE-ESEM photograph of type 2 sphalerite exhibiting textural and chemical zoning, consisting of sphalerite with porous core (pSph) which contains pyrite (Py) microglobules and is surrounded by massive sphalerite (mSph). Galena (Gn) inclusions appear into massive sphalerite. These inclusions mainly separate porous from massive sphalerite ……. 72

Figure 38 ESEM photograph of closely packed anhedral type 2 sphalerite consisting of porous cores (pSph) and massive rims (mSph) with voids (dark). Sphalerites contain inclusions of anhedral (i), skeletal assemblages (ii), and filaments and or needles (iii) of galena (Gn). …….. 72

Figure 39 XRD spectra showing the association of barite and sphalerite. The pie chart shows how well the spectra for each mineral match the XRD-diagram…….…… 72

Figure 40 Histogram showing the variation of Fe in sphalerite type 2 from Kolumbo hydrothermal precipitates ……..……..… 73

Figure 41 Histogram showing the variation of Sb in sphalerite type 2 from Kolumbo hydrothermal precipitates.……..……... 73

Figure 42 Geochemical profile across a zoned type 2 sphalerite crystal with porous core and massive rim. (A) Spots of EPMA analyses are represented by crosses accompanied by "Spectrum +number X" designation, including "Spectrum 170, 171, and 172" for the porous core, and all the rest "Spectrum number X" designations for the massive rim. (B) Enrichment of Ag, Sb, Cu towards the outer massive parts of the sphalerite crystal……..……..…. 75

Figure 43 Binary correlation plot of Zn vs. Sb in zoned sphalerite with porous core and massive rim (Type 2)…….…….……..…. 76

Figure 44 Binary correlation plot of Zn vs. Fe in zoned sphalerite with porous core and massive rim (Type 2)…….…….……..…. 76

Figure 45 Binary correlation plot of Zn vs. Cu in zoned sphalerite with porous core and massive rim (Type 2)……..……. 77

Figure 46 Binary correlation plot of Zn vs. Cd in zoned sphalerite with porous core and massive rim (Type 2).……..……. 77

Figure 47 Binary correlation plot of Zn vs. As in zoned sphalerite with porous core and massive rim (Type 2).……..……. 78

Figure 48 ESEM photograph of (a) inclusion-rich, massive sphalerite (type 3) with randomly dispersed inclusions, in association with barite (Ba). (b) galena (Gn) inclusions and symplectites of Pb–Sb-bearing phases in inclusion-rich, massive sphalerite of Type 3…….....……...……. 78

Figure 49 ESEM-BSE photograph of inclusion-rich, massive sphalerite (type 3) containing ubiquitous galena (Gn) inclusions arranged mainly in thick linear patterns..…… 79

Figure 50 ESEM photograph showing the association between massive sphalerite of type 3 and colloform pyrite (Py), and barite (Ba) blades.…..... 79

Figure 51 ESEM photograph of (a) massive, zoned sphalerite (Sph) with Cu-rich zones. (b) Massive, zoned sphalerite (Sph) with Cu-rich zones, galena (Gn) inclusions and pyrite (Py)……. 79

Figure 52 ESEM photograph of Hg-Cd sulfosalt inclusions in massive sphalerite (type 3) (a) in the form of "star-like" inclusions (b) in the form of "star-like" inclusion encircled in Hg-Cd-rich rim.……. 80

Figure 53 Histogram showing the variation in Fe in massive sphalerite of type 3 from Kolumbo hydrothermal precipitates..……..……..…… 80

Figure 54 Histogram showing the variation in Sb in massive sphalerite of type 3 from Kolumbo hydrothermal precipitates ……..…… .. 81

Figure 55 Histogram showing the variation in Cd in massive sphalerite of type 3 from Kolumbo hydrothermal precipitates …… 81

Figure 56 Histogram showing the variation in Fe in compositionally zoned, massive sphalerite of type 3 from Kolumbo hydrothermal precipitates..……..……..……..... 81

Figure 57 Histogram showing the variation in Sb in compositionally zoned, massive sphalerite of type 3 from Kolumbo hydrothermal precipitates …… 82

Figure 58 Histogram showing the variation in Cd in compositionally zoned, massive sphalerite of type 3 from Kolumbo hydrothermal precipitates.…….…. 82

Figure 59 Geochemical profile across a massive type 3 sphalerite crystal. (a) Spots of EPMA analyses are represented by crosses accompanied by "Spectrum +number X" designation. (b) Enrichment of Ag, Sb, Cu towards the outer parts of the sphalerite crystal……. 85

Figure 60 Geochemical profile across a zoned, massive type 3 sphalerite crystal. Analyses 1-4 refer to the core, 5-8 to the sector and 9-11 are from the rim of zoned, massive sphalerite crystal. (a) Spots of EPMA analyses are represented by the orange numbers. (b) The core contains Cd, Fe and Sb (analyses 1-4), the sector contains Ag, Cd, Fe, Sb and Cu (analyses 5-8) and the rim contains Sb and Fe (analyses 9-11).…….…….. 86

Figure 61 EDS elemental map of the inclusion-rich massive sphalerite of Figure 48b for S, Fe, Zn, Sb, Hg and Pb. The anhedral inclusions contain Fe and Pb, while the symplectites are consisted of Sb, Pb and Hg……..…….. 87

Figure 62 EDS elemental map of a Hg-Cd inclusion in massive type 3 sphalerite for S, Zn, Hg, Fe and Cd……..…. 88

Figure 63 EDS elemental map of a Hg-Cd inclusion into a Sb-rich area of massive type 3 sphalerite for S, Zn, Hg, Fe, Sb and Cd…… 89

Figure 64 Binary correlation plot of Zn vs. Fe in massive sphalerite (Type 3)……... 90

Figure 65 Binary correlation plot of Zn vs. Sb in massive sphalerite (Type 3)…….. 90

Figure 66 Binary correlation plot of Zn vs. Cd in massive sphalerite (Type 3)…….. 91

Figure 67 Binary correlation plot of (a) Zn vs. As, (b) Zn vs. Ag and (c) Zn vs. Cu in massive sphalerite (Type 3)…….….. 91

Figure 68 Binary correlation plot of Zn vs. Fe in zoned, massive sphalerite (Type 3)…….. 91

Figure 69 Binary correlation plot of Zn vs. Sb in zoned, massive sphalerite (Type 3)…….….. 92

Figure 70 Binary correlation plot of Zn vs. Cd in zoned, massive sphalerite (Type 3)…… 92

Figure 71 Binary correlation plot of Zn vs. Cu in zoned, massive sphalerite (Type 3)…….. 93

Figure 72 Binary correlation plot of Zn vs. Ag in zoned, massive sphalerite (Type 3)…… 93

Figure 73 The three sphalerite textural varieties arranged in order of maturity. a) Transmitted light microphotograph (TLP) of colloform zoned sphalerite (Type 1) (oil lens and //Nichols). b) ESEM photograph of sphalerite (Sph) colloform microglobules (Type 1). c) Reflected light microphotograph (RLP) of zoned sphalerite with porous core and massive rim (Sph) (Type 2), having inclusions of colloform pyrite/marcasite (Py) and being in association with blades of barite (Ba) (oil lens and // Nichols). d) ESEM photograph of sphalerite with porous core (pSph) and massive rim (mSph) (Type 2) with voids (dark) and galena (Gn) inclusions. g) Reflected light microphotograph (RLP) of inclusion-rich and compositionally zoned massive sphalerite (Sph) (Type 3) with inclusions of closely-packed pyrite globules (Py) and anhedral Sb-Pb-sulfosalts (oil lens and // Nichols). h) ESEM photograph of compositionally zoned massive sphalerite (Sph) (Type 3) containing galena inclusions (Gn) and barite (Ba) blades……. 96

Figure 74 Box-whisker plot showing the concentration of (a)Fe, (b) Zn, (c) Sb, (d) Cu in each sphalerite type. Boxes represent the 25th and 75th data percentiles, whiskers represent the 10th and 90th percentiles, and symbols represent outliers (outside the 10th and 90th percentiles). The horizontal line in each box represents the median…… 97

Figure 75 Dendrogram based on statistical correlation of the elements contained in Kolumbo sphalerite samples clustered into two main groups with similarity level >54%. The first group is subdivided into 2 subgroups: subgroup 1 includes Fe and Zn (similarity 62 %) and subgroup 2 includes Cd and Hg (similarity level 74 %). The second group includes Sb, Pb, Cu, Ag and As with similarity level 60%..... 100

Figure 76 The solubility of sphalerite as a function of pH for 1 and 12 wt % NaCl fluids at 150 and 300°C and mΣS = 0.05. The thin vertical lines represent the boundary between the predominance of chloride species (to the left of the lines) and bisulphide species. It is clear from this figure that sphalerite solubility is significantly higher at low pH, where chloride species predominate. If Zn is transported under such conditions, it can be seen that its solubility will significantly decrease if the fluid undergoes a decrease in temperature or increase in pH, potentially resulting in precipitation of sphalerite. After **Tagirov & Seward (2010)**…… 102

LIST OF ABBREVIATIONS

CNMNC	Commission on New Minerals, Nomenclature and Classification
CSK	Christiana – Santorini – Kolumbo
EPMA	Electron Probe Microanalysis
EPA	Environmental Protection Agency
HSA	Hellenic Sedimentary Arc
HSS	Hellenic Subduction System
HVA	Hellenic Volcanic Arc
IMA	International Mineralogical Association
IPCN	Interior Porous Conduit Networks
IR	Intrusion Related
ISSC	Inner Sulfide-Sulfate core
KHF	Kolumbo Hydrothermal Field
MVT	Mississippi-Valley-Type
MOR	Mid-ocean Ridge
OAsL	Outer As-sulfide-dominated layer
R/V	Research Vessel
ROV	Remotely Operated Vehicle
SEDEX	Sedimentary Exhalative
SFeC	Surface Fe crust
VMS	Volcanogenic Massive Sulfide

1. Introduction

Seafloor hydrothermal venting systems constitute the link between deep-seated processes (volcanism, tectonism) and the seafloor, are responsible for chemical and thermal exchanges that sustain ecosystems in extreme conditions, and have produced some of the most valuable metal deposits mined to date **(Hannington et al. 2005, *and references therein*)**. Practically two-thirds of all known modern sea-floor hydrothermal systems, with associated mineral deposits and chemosynthetic microbial biomes, occur at intermediate and slow-spreading mid-ocean ridges (MORs). Several others occur in convergent plate margins: (i) along volcanic arcs that have a submarine component, and (ii) in intraoceanic back-arc basins and arc-related rifts at continental margins. The majority of these hydrothermal vents occur typically at water depths from 2,000 to 4,000 m, and it is only recently that hydrothermal research has been conducted to submarine arc volcanoes, where active hydrothermal vents are located at surprisingly shallow water depth (95% at <1,600 m water depth) **(de Ronde et al. 2003)**. Research at shallow hydrothermal systems on arc volcanoes, e.g. Kolumbo (Santorini, Hellenic Volcanic Arc) **(Kilias et al. 2013)** and Palinuro (Aeolian island arc, Italy) **(Petersen et al. 2014)** has important consequences for the style of venting, the nature of associated mineral deposits (i.e. Volcanogenic Massive Sulfides (VMS)), the local biological communities, potential hazards (i.e. tsunamis, explosive eruptions) and identify sources of toxic metals (e.g. Sb, Hg, Tl) in the world's oceans.

The hydrothermal vent field located on the floor of the density-stratified acidic (pH ~ 5) crater of the Kolumbo shallow-submarine arc-volcano, near Santorini, Hellenic volcanic arc (HVA) **(Sigurdsson et al. 2006, Carey et al. 2011, Kilias et al. 2013)** features considerable bulk enrichments of polymetallic spires in trace metals of economic and environmental importance: Sb, Tl, Hg, As, Au, Ag, Pb and Zn indicating a new hybrid seafloor analogue of epithermal-to-volcanic-hosted-massive-sulfide deposits **(Kilias et al. 2013)**. The average and maximum bulk concentrations of Hg (397 ppm and 1070 ppm respectively) and Ag (871 ppm and 1910 ppm) are among the highest reported from modern seafloor hydrothermal systems worldwide **(Fig. 1) (see Kilias et al. 2013)**, whereas there are only four reports for Hg and Ag in the HVA: Ag has been mentioned in Ag-rich sulphides in Vani Cape, Milos Island **(Voudouris et al. 2014)** and up to 10 ppm Ag in Mn-oxides in Vani Cape, Milos Island **(Hein et al. 2000)**, whereas very low contents of Hg (80-179 ppb) have exclusively been reported from hydrothermal sediments, Santorini **(Smith & Cronan 1983)** and a recent conference

abstract reports the occurrence of cinnabar in the submarine hydrothermal vents at Palaeochori Bay, Milos Island **(Kati et al. 2015)**. However, these two metals together have not been detected neither in marine hydrothermal precipitates, hydrothermal fluids and associated hydrothermal sediments, nor the metamorphic basement, of the whole Hellenic Volcanic Arc **(Varnavas and Cronan 1988; 1991; 2005, Valsami-Jones et al. 2005) (Fig. 1, 2**); Therefore, the Kolumbo submarine hydrothermal vent field marks an Hg and Ag geochemical anomaly compared to the rest of the HVA; it is worth mentioning that Ag from the hydrothermal vent field of Kolumbo is positively related to Au **(Kilias et al. 2013) (Fig. 3)**. The major Powder X-Ray Diffraction (PXRD)-crystalline phases comprising the Kolumbo hydrothermal precipitates are barite ($BaSO_4$) together with galena (PbS), sphalerite (ZnS) and pyrite/marcasite (FeS_2). Bulk trace element concentrations are controlled by the modal abundance of the various minerals present and by the trace metal enrichment within these mineral phases. Whereas it is known so far that Sb is present in pyrite/marcasite, it occurs as unidentified non-stoichiometric $Pb_nSb_mS_p$ and $Zn_mSb_nS_p$ sulfosalts, and it is also associated with poorly crystalline ferrihydrite-like phases **(Kilias et al. 2013, Gousgouni 2014)**, no Tl- , Au-, Ag- and Hg-bearing minerals have been detected; therefore the identification of mineral carriers for these metals constitutes a goal with important economic and environmental significance.

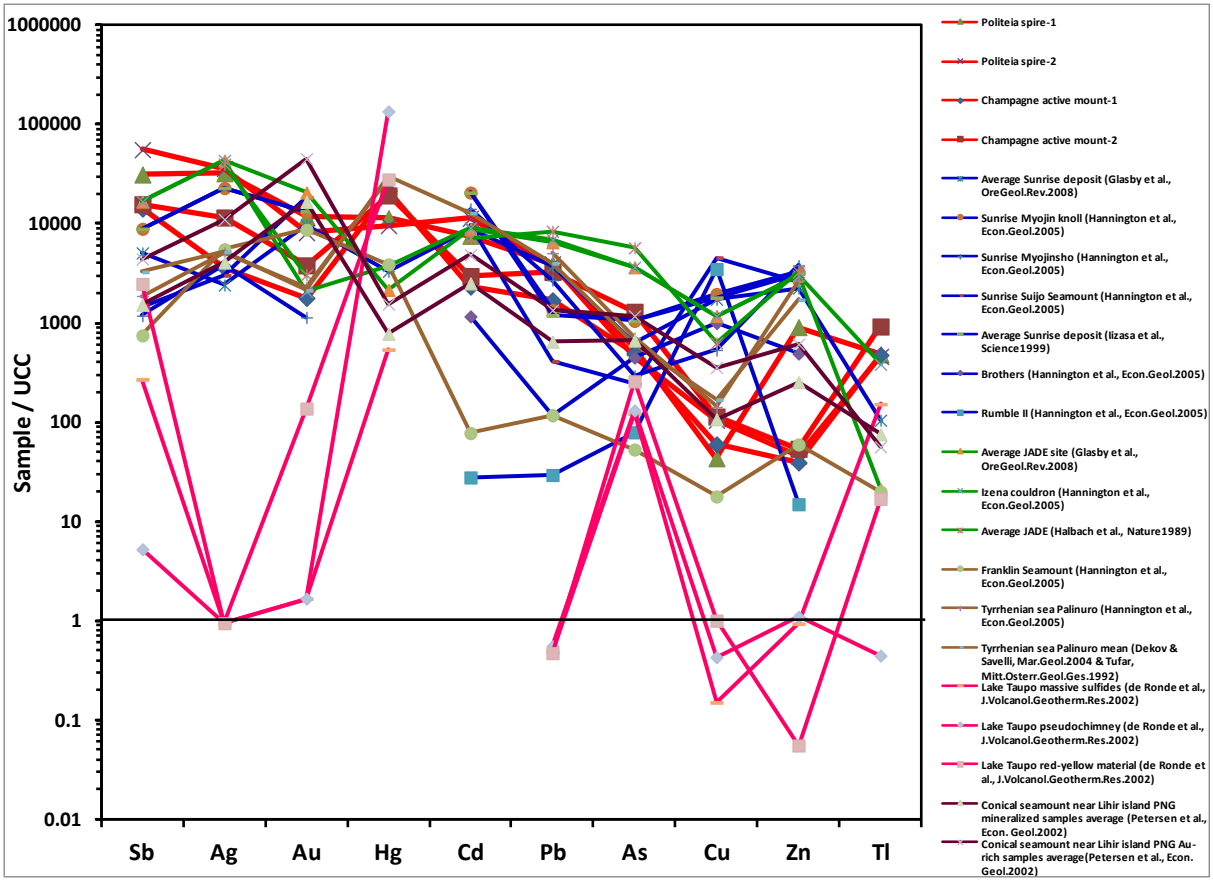

Figure 1. Geochemical spidergram comparing the Kolumbo vent samples with other seafloor hydrothermal deposits from various tectonic settings (modified after Kilias et al. 2013). Concentrations are normalized to Upper Continental Crust (UCC) (Rudnick & Gao 2003) for selected noble (Ag, Au), potentially life-essential (Cu, Zn) and potentially toxic (Sb, Hg, Cd, As, Tl) elements. The average and maximum concentrations of Tl (510 ppm and >1,000 ppm respectively) and Sb (8,333 ppm and 2.2 wt %, respectively) are among the highest reported from modern seafloor hydrothermal systems. Average Sunrise deposit (Iizasa et al. 1999), Sunrise Myojin knoll (Hannington et al. 2005), Sunrise Myojinsho (Hannington et al. 2005), Sunrise Sujo Seamount (Hannington et al. 2005), Brothers (Hannington et al. 2005), Rumble II (Hannington et al. 2005), Average JADE site (Glasby et al. 2008), Izena cauldron (Hannington et al. 2005), Average JADE (Halbach et al. 1989), Franklin Seamount (Hannington et al. 2005), Tyrrhenian sea Palinuro (Hannington et al. 2005), Tyrrhenian sea Palinuro mean (Dekov & Savelli 2004, Tufar 1991), Lake Taupo massive sulfides (de Ronde 2002), Lake Taupo pseodochimney (de Ronde 2002) Lake Taupo red-yellow material (de Ronde 2002), Conical seamount-mineralized samples average (Petersen et al. 2002), Conical seamount gold-rich samples average (Petersen et al. 2002).

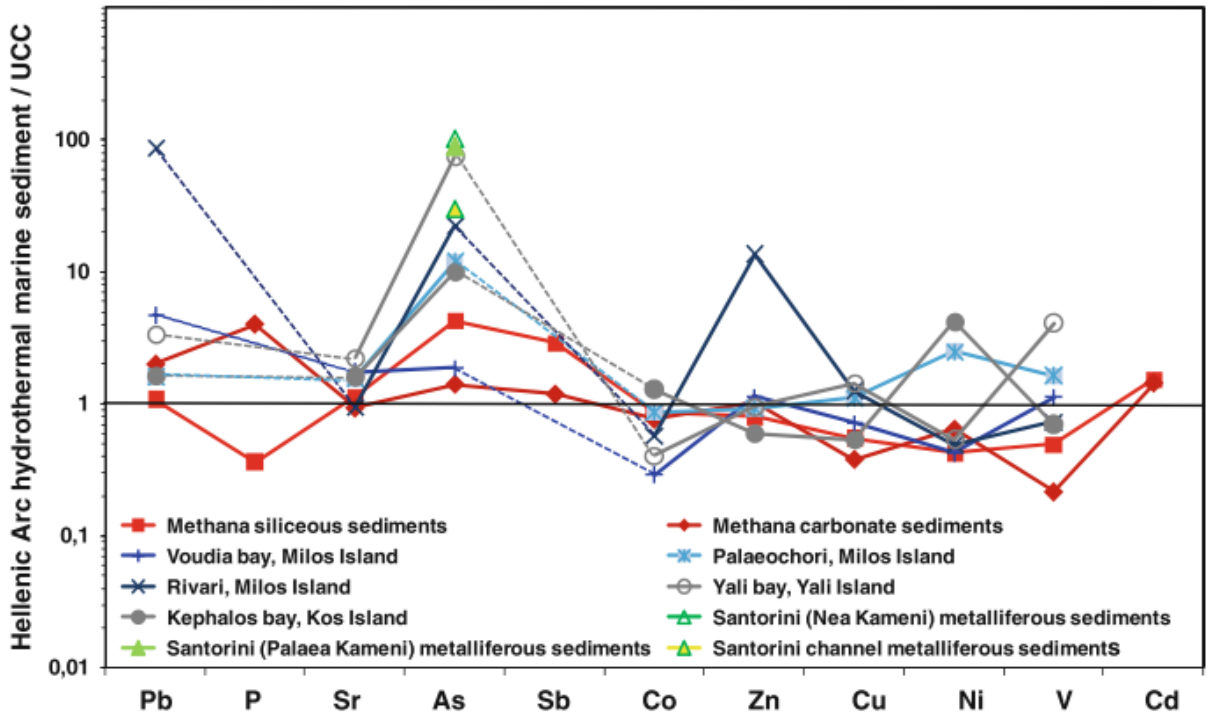

Figure 2. Upper Continental Crust (UCC)-normalized (according to Rudnick and Gao (2003)) spidergram of trace elements in marine hydrothermal precipitates of the Hellenic Volcanic Arc. Average values of Methana siliceous sediments (Huebner et al. 2004): red thick line and solid square; Average values of Methana carbonate sediments (Huebner et al. 2004): darker red-brown thick line and solid lozenges; Milos Island sediment (Cronan & Varnavas 2001, Varnavas & Cronan 2005): blue thick line and plus symbol correspond to Voudia Bay samples, light blue thick line and asterisk in lighter blue background correspond to Palaeochori, dark blue thick line and cross correspond to Rivari, respectively; Yali Island (Yali Bay) sediments (Varnavas & Cronan 1991, 2005): gray thick line and open circle; Kos Island (Kephalos Bay) sediments (Rudnick & Gao 2003) gray thick line and closed circle; Average values of Santorini caldera metalliferous marine sediments (Varnavas & Cronan 1988): green thick line and open triangle correspond to Nea Kameni islet, light green thick line and closed triangle correspond to Palaea Kameni islet, yellow thick line and green triangles with yellow filling color correspond to Santorini "channel" situated between Palaea and Nea Kameni islets (Gamaletsos et al. 2013).

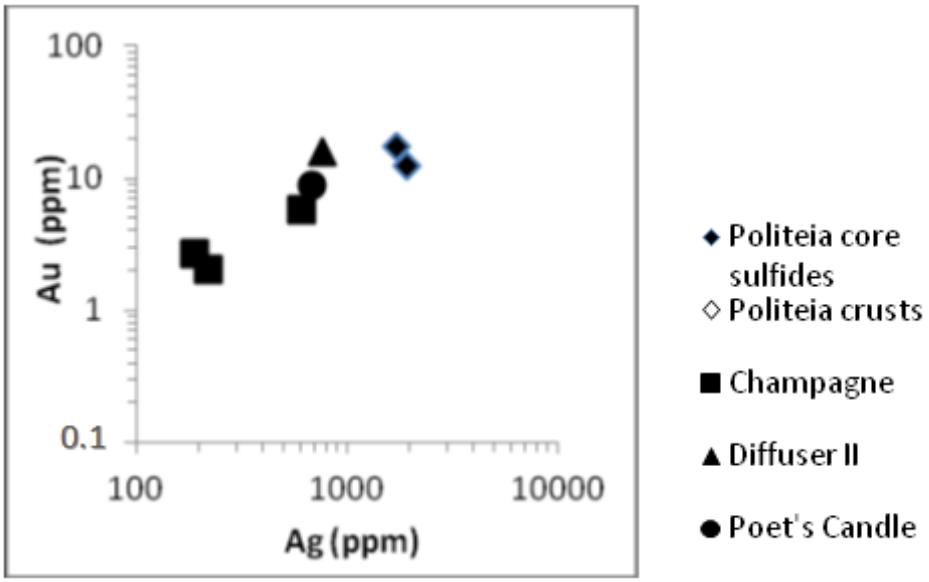

Figure 3. Log/log plot of Ag versus Au, showing a positive correlation (Kilias et al. 2013-Supplementary information).

Except for pyrite (e.g. **Keith et al. 2016, *and references therein***), sphalerite is a notoriously important host mineral for a wide range of minor and trace elements, such as Cd, Co, Ga, Ge, In, Mn, Sn, As, Tl, Hg, Sb, Cu, Ni, Ag, Mo, Pb, Se, Te, Bi, U, Au either as solid solution and/or as nanoparticles and micro-inclusions (**Oftedahl 1940, Grammatikopoulos et al. 2006, Cook et al. 2009, Ye et al. 2011, Radosavljević et al. 2012, Keith et al. 2014, Wohlgemuth-Ueberwasser et al. 2015**); this feature is the primary reason for the wide variety of colors with which sphalerite crystallizes, varying from red, orange (and pale brown varieties referred as honey blende) and green, to white (cleiophane variety) and black (marmatite variety) (**Boyce et al. 2015**). Consequently, spalerite is a major candidate to host the metals of interest (Hg and Ag) regarding the Kolumbo hydrothermal precipitates.

Sphalerite, the most abundant primary ore mineral of Zn, it is found in a large variety of ore deposit types, but its greatest abundance is in Volcanogenic Massive Sulfide (VMS), Sedimentary Exhalative (SEDEX), or Mississippi-Valley-Type (MVT) deposits (**Deer et al. 1992, Hannington 2014, Wilkinson 2014**). It crystallizes in the cubic crystal system and has a cubic unit cell of ~ 0.541 nm (5.41 Å) (**Deer et al. 1992**). Each S atom in the sphalerite structure is coordinated with four Zn atoms, forming a regular tetrahedron, with the Zn atoms surrounded by S in a similar manner (**Fig. 4A**). The crystal habit of sphalerite is generally hextetrahedral, resulting primarily in the development of {111} crystal faces (**Barrie et al. 2009**). Apart from sphalerite, wurtzite is the high-temperature polymorph of ZnS that crystallizes in the hexagonal crystal system with a similar arrangement of the Zn and S atoms

(**Fig. 4B**) and it commonly occurs in modern ocean-ridge hydrothermal vent systems rather than in ore deposits (**Herzig & Hannington 1995, Boyce et al. 2015**).

Sphalerite's capacity to incorporate a variety of trace elements can reach high levels posing either an economic resource for rare metals such as Ga, Cd, In and Ge, or an environmental hazard, as deleterious elements like Cd, Hg, As, etc., may appear in significant concentrations (**Boyce et al. 2015**). Therefore, spalerite is a major candidate mineral to host the metals of interest regarding the Kolumbo hydrothermal precipitates.

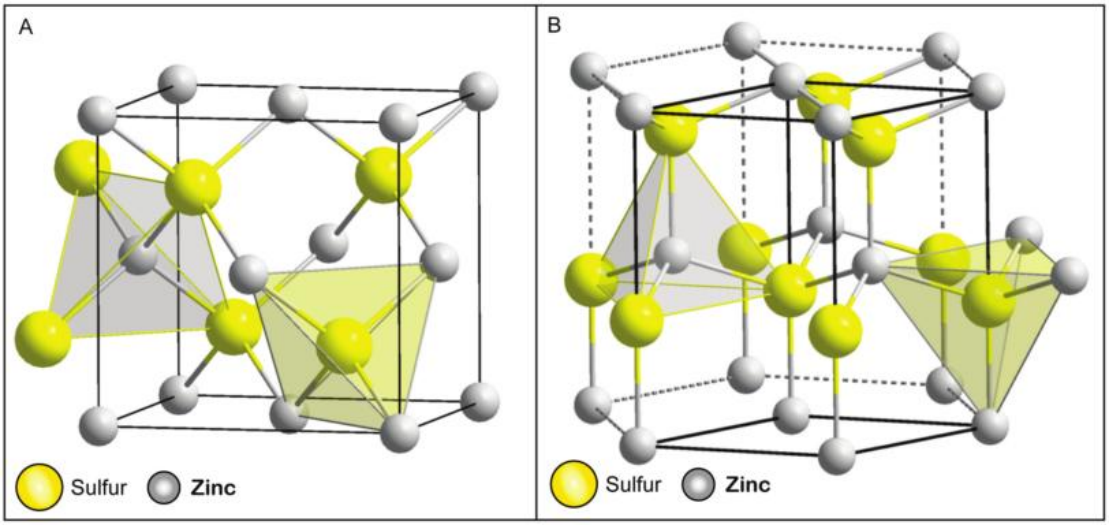

Figure 4: Crystal structures of the two main forms of ZnS, showing the tetrahedral relationship between Zn and S atoms. A. Cubic structure of sphalerite. B. Hexagonal structure of wurtzite. (Images reproduced from Wikipedia).

Many elements enter the sphalerite structure via simple substitution of similar-sized ions ($Zn^{2+} \leftrightarrow Fe^{2+}$, Cd^{2+}, Mn^{2+}, Co^{2+} or $S^{2-} \leftrightarrow Se^{2-}$), by coupled substitution (e.g., $2Zn^{2+} \leftrightarrow Cu^{+} + In^{3+}$) **(Ye et al. 2011)** or they may be incorporated as mineral nanoparticles in sphalerite **(Ciobanu et al. 2011)** (e.g. As and Sb may be tetrahedrite–tennantite micro-inclusion controlled in galena–"fahlore" associations **(Cook et al. 2009, Maslennikov et al. 2009, Wohlgemuth-Ueberwasser et al. 2015)**).

In this thesis, we describe mercury (Hg)─ and silver (Ag)─rich sphalerite mineralization associated with the shallow-submarine hydrothermal vent field of the Kolumbo volcano, Santorini, Greece. The Kolumbo sphalerite is unique in as much that it constitutes the first report of sphalerite notably enriched in either or both Hg and Ag, that is associated with polymetallic deposits found in modern ocean-floor hydrothermal systems, the recent analogues of ancient volcanogenic massive sulfide (VMS) deposits and an important resource of e.g. Zn, Cu, Pb, Ag, and Au (**Wohlgemuth-Ueberwasser et al. 2015, Keith et al. 2014,**

Petersen et al. 2014). This thesis describes sampled sphalerites, their textural, chemical and paragenetic characteristics, presents analyses of various trace metals with special emphasis to Hg and Ag, proposes a genetic model, and discusses the environmental implications of the release of these potentially toxic metals to the Aegean Sea.

2. Scope of thesis

This study aims to contribute to a better understanding of the concentration, distribution, and geochemical/geological controls of trace and minor metals in natural sphalerite samples from the modern shallow seafloor, with special emphasis on Hg and Ag, using Kolumbo hydrothermal field (KHF) as an example; furthermore, to discuss the possible sphalerite forming mechanisms, and relevant ore processing and environmental implications. Additionally, it is essential to probe the role of Kolumbo submarine hydrothermal activity as a possible source of toxic metals in modern seafloor which may affect both microbial metabolism and, through the food chain, humans into a high-touristic area. Ag is not only toxic, but also a precious metal, consequently the study of sphalerite will give important information about submarine mineralization and accumulation of Ag.

Towards this scope, the main objectives are:

- Define the main textural variations (types) of sphalerite; determine the concentrations of trace and minor metals, and especially Hg and Ag in the various sphalerite types as determined by ESEM-WDS.
- Define trace element distribution and correlation trends and discuss trace metal substitution mechanisms in sphalerite.
- Investigate the distribution and redistribution of trace elements among sphalerites of differing textures, and further discuss the mobility of trace metals during the course of hydrothermal diagenesis and maturity.
- Propose a genetic model for Hg- and Ag-rich sphalerite in polymetallic hydrothermal modern seafloor mineralization (i.e. source of metals, deposition mechanism etc.).
- Discuss ore processing and environmental implications.

3. Previous work

3.1 Sphalerite as a carrier of Hg and Ag

Mercurian (Hg) sphalerite and/or argentiferous (Ag) sphalerite have been reported from a few localities worldwide in association with various geological settings. In some deposits, sphalerite may be the dominant Hg-carrier. Exceptionally high contents of 0.08–16.35 wt % Hg are reported in sphalerite from the Eskay Creek VMS deposit (Canada) **(Grammatikopoulos et al. 2006)**. Further, sphalerite with low contents of Hg (up to 149 ppm) has been reported from the Broken Hill SEDEX deposit (Australia) **(Ryall 1979)**, the Linares intrusion-related gold deposit (Spain) **(Di Benedetto et al. 2005)** (mean Hg value: 707 ppm), and the Akoluk epithermal deposit (Turkey) (max.: 4.815 wt % Hg) **(Çiftçi 2009).** The main characteristic of Hg-bearing sphalerite in these deposits is its association with Hg minerals (e.g. cinnabar/metacinnabar (HgS), schwatzite $(Cu,Hg)_{12}Sb_4S_{13}$)), while in the Akoluk epithermal gold deposit, it is associated with stibnite and Sb–Pb sulfosalts without Hg minerals. **Radosavljević et al. (2012)** report variable Hg content in sphalerite between 0.30 and 6.47 wt % in the Rujevac polymetallic [Sb(As)–Pb–Zn] vein-type ore deposit in Serbia. **Jonasson & Sangster (1974)** conducted a study on the distribution of Hg in sphalerite from a number of Canadian VMS deposits and they determined the highest Hg concentrations in the most Zn-rich ores occur in the presence of Ag-Pb-bearing sulfosalts, which typically represent minor components of the ore. Similar trends were also observed at the Woodlawn VMS deposit in eastern Australia by **Ryall (1979)**. **Roth (2002)** reports the average Hg content of the low-Hg sphalerite group of the Eskay Creek VMS deposit (BC, Canada) (0.62 wt % Hg), which is one order of magnitude higher than the maximum detected by **Jonasson & Sangster** (**1974**; 0.045 wt % Hg), two orders of magnitude higher than the maximum at Woodlawn (18 ppm; **Ryall 1979**), and two to three orders of magnitude greater than typical values (10^{-3} to 10^{-4} wt % Hg) for sphalerite found in most polymetallic deposits **(Tauson & Abramovich 1980).** Metamorphosed VMS and SEDEX sulfide deposits may contain sphalerite with measurable and relatively consistent concentrations of Hg, i.e. ≤300 ppm difference between the lowest and highest mean values. Well defined negative correlations between Hg and Zn, as well as the relatively consistent Hg concentrations and generally low standard deviations relative to the means, indicate that Hg is most likely lattice-bound ($Zn^{2+} \leftrightarrow Hg^{2+}$) in sphalerite **(Grammatikopoulos et al. 2006; Radosavljević et al. 2012; Lockington et al. 2014)**.

Several authors have suggested that significant amounts of silver may be incorporated in sphalerite (e.g., **Taylor & Radtke 1969**). Although sometimes regarded as an Ag-carrier, practice indicates that in fact higher concentrations are almost always related to microscopic or submicroscopic inclusions of discrete Ag-minerals (e.g. tetrahedrite-tennantite) **(Cook et al. 2009**). Despite that, concentrations up to 100 ppm, rarely higher, are reported for a small number of ore deposits (e.g., Red Dog, Alaska (SEDimentary EXhalative deposit) (SEDEX) **(Kelley et al. 2004)**. **Cabri et al. (1985)** reported values from 12 ppm to 308 ppm from Kidd Creek VMS deposit (Ontario, Canada); an exception to the generally low Ag contents is 650–700 ppm obtained by the same authors for sphalerite from the Nanisivik, N.W.T., Mississippi-Valley-Type deposit (MVT). **Huston et al. (1995; 1996)** report low levels of Ag (below 30 ppm) in the sphalerite lattice of Australian ores, and values between 30–110 ppm from the Agincourt VMS deposit. Using ion microprobe techniques, **Chryssoulis & Surges (1988)** illustrated that ppm levels of Ag within sphalerite make it a minor Ag-carrier in mill circuits of VMS deposit at New Brunswick, NB, Canada. Microanalysis of sphalerite often reveals heterogeneous distributions within individual datasets reflecting the significance of (micro)inclusions of Ag-minerals **(Cook et al. 2009**). According to **Ye et al. (2011)** Ag concentrations from Bainiuchang and Dabaoshan SEDEX deposits (South China) reach up to 188 – 198 ppm, respectively.

Moreover, Ag-rich sphalerite has been reported from: (1) Carbonate-hosted Mississippi-Valley Type (MVT) deposits and vein-type deposits (0.40-0.82 ppm), Germany (**Pfaff et al. 2011**); incorporation mechanisms may include most likely the presence of nano- or micro-inclusions of Ag-hosting phases, and to a lesser extent substitution of Ag into the crystal lattice of the host sphalerite (**Pfaff et al. 2011**); (2) Vein and replacement-type Sn-polymetallic-Zn deposits ((≤0.95-1.05 wt %) (**Murakami & Ishihara 2013**). The highest Ag content has been interpreted as a result of the presence of sub-micron-scale inclusions of Ag- and Pb-Sb-bearing sulfides, rather than the coupled substitutions such as $(2Zn^{2+}) \leftrightarrow (Cu^{+}$ or $Ag^{+}, In^{3+})$; (3) Vein-type Zn–Ge–Ag–(Pb–Cd) deposit (≤ 1,000 ppm) **(Belissont et al. 2014)**. Crystallographic controls on the incorporation of Ag and other trace elements (e.g. Ge, Sb, and As) have been suggested, i.e. coupled substitution mechanisms $(3Zn^{2+} \leftrightarrow Ge^{4+} + 2Ag^{+})$; (4) Epithermal Au–Cu–Zn–Pb–Ag deposit (max 0.03-0.05 wt %) (Dill et al., 2013); (5) Metamorphosed VMS and SEDEX sulfide deposits **(Lockington et al. 2014)** where concentrations of Ag are typically a few ppm in all samples except for those from Mt. Isa, where means of 23 and 66 ppm have been measured. In lower-temperature deposits such as SEDEX, sphalerite is likely to be an important Ag carrier but such Ag will be remobilised to

form discrete Ag minerals during metamorphism **(Lockington et al. 2014)**; (6) Skarn, syngenetic massive sulfide, MVT deposits in China which contain sphalerite with measurable quantities of Ag **(Ye et al. 2011)**; the highest Ag concentrations are observed in Bainiuchang (max: 188 ppm) and Dabaoshan deposit (SEDEX) (max: 198 ppm) (means 64 and 35 ppm, respectively). Interestingly, the two skarns have the lowest deposit means in the dataset (6.0 and 8.3 ppm for Luziyuan and Hetaoping, respectively). The dataset expands the understanding of sphalerite mineral chemistry by also indicating that elements, whose ability to enter the crystal structure of sphalerite has been previously debated (Ag, Sn, Tl, Sb), may also be in solid solution **(Ye et al. 2011)**. **Maslennikov et al. (2009)** reported that the majority of sphalerite in hydrothermal chimneys from the Silurian Yaman-Kasy VMS deposit in the Southern Urals is characterized by high concentrations of Ag (338 ppm) as well as Co, Sn, Cd, Mn, Ag, Au, Pb, As, and Sb. Silver is likely to reside in sulfosalts (Ag-rich enargite, tennantite, and tetrahedrite) which are common inclusions in sphalerite.

3.1.1 Mercury(Hg)- and Silver(Ag)-rich sphalerite from the modern ocean-floor

Studies of mercurian and argentiferous sphalerite from the modern ocean-floor are extremely scarce; in the mainstream literature there is a single recent relevant report. This sphalerite has been derived from a drilled subseafloor massive sulfide deposit that occurs in shallow waters at the Palinuro volcanic complex, Tyrrhenian Sea, Italy (Italy) **(Petersen et al. 2014).** Sphalerite hosts Hg (<0.1–7.4 wt %, average 0.8 wt %), Ag (<0.1– 0.22 wt %, average 0.02 wt %) along with a large variety of other trace metals, such Pb, As, Cd, Sb,; Hg is likely present in solid solution **(Petersen et al. 2014).** Further recent studies of trace elements in hydrothermal black smoker sulfides **(Wohlgemuth-Ueberwasser et al. 2015; Keith et al. 2016)** do not report either Hg-bearing and/or Ag-bearing sphalerite, but only they report high bulk Hg contents (PACMANUS) and pyrites that have highly variable concentrations of elements like Au, Co, Cu, Se, Mo, Ag and Sb that are most likely related to fluid evolution and changes in fluid composition.

Wohlgemuth-Ueberwasser et al. (2015) studied sphalerite from 27 black smoker samples from active and inactive vents derived from three different seafloor hydrothermal fields: the ultramafic-hosted Logatchev hydrothermal field and the basaltic-hosted Turtle Pits field on the Mid-Atlantic Ridge, and the felsic-hosted PACMANUS field in the Manus basin (Papua New Guinea). Sphalerite from these fields hosts a large variety of trace elements such as Fe, As, Sb, Au, Pb, and Cu but no Hg or Ag. **Keith et al. (2014)** report major and minor

element concentrations in pyrite from submarine hydrothermal vents at mid-ocean ridges, back-arc spreading centers, and island arc volcanoes hosted in sedimentary and magmatic rocks of variable composition. The conclusion according to the same authors is that sphalerite from sediment-covered and sediment-starved vents can be distinguished by higher Fe/Zn ratios and elevated sulfur contents of the former. This study does not report anything about sphalerite content in trace elements, consequently not also about Hg and Ag.

3.2 Hg in the geoenvironment: what we know and what we don't know

Unless otherwise noted, the following synthesis is based on **Selin (2009), Barkay & Wagner-Döbler (2005)**, **Colaço et al. (2006)**, **Taylor et al. (2001)**, **Belzile et al. (2008)**. **Hazen et al. (2012)** and **Gaffney & Marley (2014).**

3.2.1 The international scene: Health concerns and related Hg-reduction policies

Mercury (Hg) is a naturally occurring toxic heavy metal that is found everywhere throughout the environment. Hg occurs in three common valence states: 0, 1+, and 2+: Hg^0 [Hg 0](elemental Hg), Hg_2^{2+} [Hg I] (mercurous Hg), and Hg^{2+} [Hg II] (mercuric Hg). Hg(I), rapidly and reversibly disproportionates to give elemental Hg and mercuric Hg, as:

$$Hg_2^{2+} \leftrightarrow Hg^0 + Hg^{2+}$$

Hg exists naturally in many minerals, including cinnabar (HgS), corderoite ($Hg_3S_2Cl_2$), and livingstonite ($HgSb_4S_8$) (see below **Section 3.2.3.1 "Hg minerals"**). Cinnabar, the most common Hg ore, is usually found associated with recent volcanic activity and alkaline hot springs; however, Hg also occurs as an impurity in nonferrous metals and fossil fuels, coal in particular. It is transported throughout the global environment after being released from these geological reservoirs by either natural or anthropogenic processes. After release, it cycles between the atmosphere, land, and surface waters through a complex web of physical and chemical transformations that have a dramatic effect on its chemical properties, environmental impacts, and biological toxicity.

Human activities have increased the amount of Hg-concentrations in the atmosphere, ocean, and terrestrial systems (**Mason & Sheu 2002**). Although all forms of Hg are toxic, they differ in their degree of toxicity and in their biological effects. Exposure to elemental Hg occurs primarily through inhalation of the Hg-vapor. Atmospheric concentrations are sufficiently low that acute toxicity exposures happen only when there is an Hg-spill or at

highly contaminated sites. However, increased levels in the atmosphere may have long-term chronic effects. Approximately 80% of inhaled elemental Hg is absorbed, in contrast with less than 1% absorption after dermal exposure, and almost none (0.1%) after ingestion **(Bernhoft 2012, Broussard et al. 2002).** The half-life of elemental Hg in the body is reported to be approximately 60 days **(Broussard et al. 2002).**

The toxicity and biological effects for both Hg_2^{2+} and Hg^{2+} compounds are reported together under the generic term "inorganic Hg". Exposure to inorganic Hg can occur both through ingestion of inorganic Hg salts or inhalation of the aerosols, with absorption rates of about 10% for both ingested and inhaled inorganic Hg compounds **(Bull 2011).** Inorganic Hg compounds have low lipid solubility and therefore do not easily cross biological membranes. The half-life of inorganic Hg compounds in the body is reported to be approximately 40 days **(Broussard et al. 2002).**

Hg^{2+}can be converted to methylmercury ($CH_3Hg^{2+}X$, where "X" is a ligand, typically Cl^- or OH^-) by microorganisms in the intestinal tract **(Rowland et al. 1984**). Methylmercury is the most common organometallic Hg^{2+}compound in environmental systems. The major source of human exposure to methylmercury is ingestion of contaminated fish **(Bernhoft 2012, Mergler et al. 2007).** Methylmercury is produced biochemically by microorganisms and is taken up by aquatic plants and animals and is biomagnified through the aquatic food chain, with the highest concentrations found in the top predators. It is highly lipid-soluble, thus it is readily transported across membranes. Methylmercury is slowly broken down to Hg(II) by demethylation, presumably by microflora in the intestines, which leads to increased elimination. The half-life of methylmercury in the body is reported to be 70–80 days **(Clarkson et al. 1984).**

The disease of human poisoning by methylmercury is known as "minamata" named after Minamata City (SW Japan) where it was diagnosed for the first time in 1956, when human ingested fish and shellfish contaminated by methylmercury discharged in waste water from a chemical factory (Chisso Co. Ltd). Humans exposed to methylmercury suffer from neurological damages such as visual, auditory, and sensory disturbances, numbness, and difficulty in walking (**Harada 1995**). The effects on embryos were more serious, like mental retardation, cerebral palsy, deafness, and blindness (**Comm. Toxicol. Eff. Methylmercury 2000, Harada 1995**). One single incident of bread made with grain treated with a Hg-containing fungicide occurred in Iraq in the 1970s and the associated health effects included numbness, problems with vision, speech, and hearing, as well as deaths in adults and more serious neurological effects in the offsprings of exposed pregnant women (**Comm. Toxicol.**

Eff. Methylmercury 2000, Marsh et al. 1987). According to recent epidemiological studies exposure to methylmercury in pregnant women contributes to neurological and developmental effects in their offspring.

The Environmental Protection Agency (EPA) set the reference dose (RfD) for Hg at 0.1 μg kg body weight^{-1} day^{-1} (**US Environ. Prot. Agency (EPA) 2001**). Estimations from studies analysis from Faroe Islands, New Zealand and Seychelles revealed that offspring lose 0.18 IQ-points for each part per million increase in maternal hair Hg (**Axelrad et al. 2007**).

Wildlife health is also affected by methylmercury when exposed to high levels through their diet. Some health effects are behavioral, neurochemical, hormonal, and reproductive (**Wolfe 1998, Scheuhammer 1987**). Methylmercury occurs in both marine and freshwater fish.

3.2.2 Emissions of Hg to the atmosphere

Hg is emitted to the atmosphere by both natural processes and human activities. The latter release larger amounts of Hg compared to the natural flux of Hg derived from primary geological sources.

The sources of Hg emissions can be grouped into three major categories **(United Nations Environmental Program 2013)**: 1) natural sources or releases due to the natural mobilization of geological Hg from the earth's crust, 2) current anthropogenic sources including both release of Hg from raw materials as well as release of Hg used intentionally in products and processes and 3) historic anthropogenic sources that result from remobilization of Hg previously deposited from the atmosphere to soil, water and vegetation.

Natural, geological sources and land and ocean surfaces release Hg in its elemental form Hg^0. Apart from Hg^0, anthropogenic sources can also emit both divalent Hg^{2+} and particulate-matter-associated Hg [Hg(P)].

The global Hg assessment issued by the United Nations Environment Program in 2013 estimated that 5,500 to 8,900 tonnes (1 tonne =1 Mg) of Hg are emitted directly to the atmosphere each year, and of this, approximately 10% is from natural sources, 30% is from current anthropological sources, and 60% is from re-emission of historical anthropogenic Hg deposits **(United Nations Environmental Program 2013)**.

3.2.3.1 Natural sources

Natural sources of Hg emissions to the atmosphere are those that arise from totally natural processes without any anthropogenic intervention. There are: geothermal activities, volcanic eruptions, natural volatilization from the ocean surfaces, and weathering of Hg-containing minerals. Natural emissions of Hg to the atmosphere are low compared with the total global Hg emissions with an estimated total amount of 643 tonnes annually **(Pirrone et al. 2010, Pacyna et al. 2010).** The current estimate for the global emission of Hg to the atmosphere from geothermal activity is 60 tonnes annually, which is 9% of the total atmospheric emissions from natural sources **(Fig. 5) (Varekamp & Buseck 1986).**

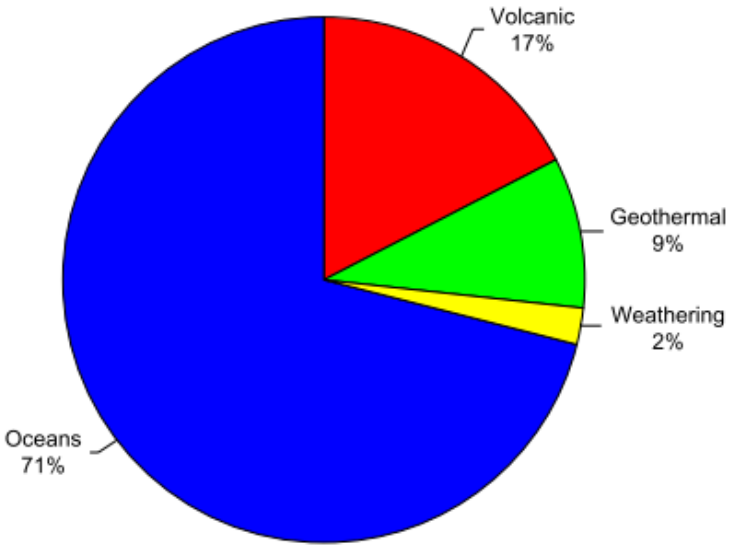

Figure 5: Relative contributions of estimated Hg emissions to the atmosphere from natural sources (Varekamp & Buseck 1986).

3.2.3.2 Current anthropogenic sources

According to the 2013 United Nations Environment Program, global Hg assessment, the relative contributions of major current anthropogenic sources to atmospheric Hg emissions are shown in **Figure 6 (Varekamp & Buseck 1986).**

The current anthropogenic sources of Hg emission to the environment are divided in two major categories. The first category includes processes where release of Hg takes place because it is present in fuels or raw materials as an impurity. For these emissions, the terms “unintentional” or “byproduct” emissions are used. The main sources of atmospheric Hg in this category are coal burning releasing about 647 tonnes to the atmosphere each year (33% of

the total current anthropogenic emissions) **(Varekamp & Buseck 1986)** and mining and smelting activities (22%), with minor contributions from combustion of oil and natural gas (1%) and oil refining (1%). The second category includes releases from products or processes where Hg is used intentionally. The largest source of atmospheric Hg in this category is small-scale gold mining (37%), followed by disposal or processing of waste from consumer products (5%). Other intentional sources of Hg emissions arise from its use in the chloro-alkali industry (1%) and release from dental fillings during human cremation (<1%).

The largest amount of current anthropogenic atmospheric Hg emissions (specifically from coal combustion) is from Asia, with a total of 931 tonnes per year, representing 47.6% of total global Hg emissions (**Figure 7**). Emissions from Asia are increasing due to increased demands for energy. Approximately 75% of Asian emissions come from the People's Republic of China **(Varekamp & Buseck 1986).**

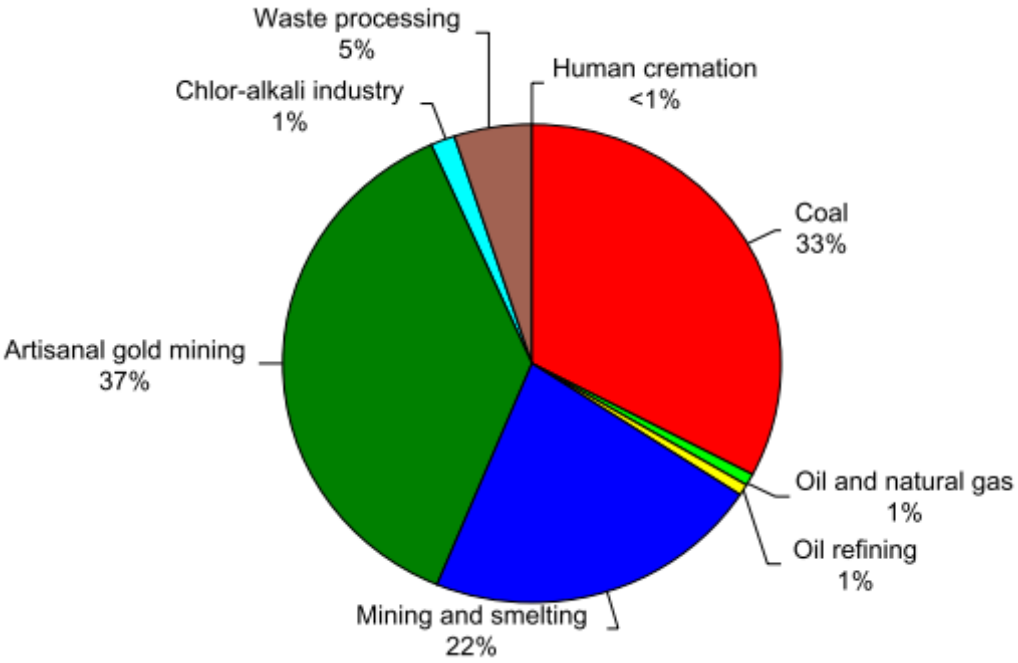

Figure 6: Relative contributions of estimated Hg emissions to the atmosphere from current anthropogenic sources (Varekamp & Buseck 1986).

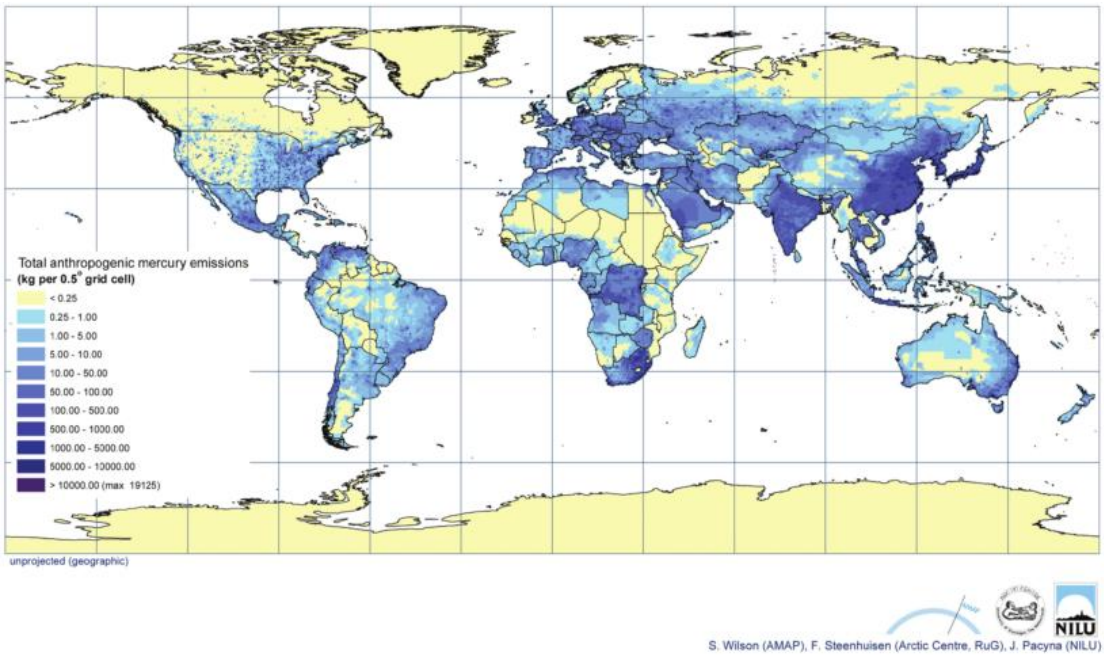

Figure 7: Spatial distribution of anthropogenic Hg emissions to the atmosphere for the year 2000. (Pacyna et al. 2005, Selin et al. 2009).

3.2.3.3 Historical anthropogenic sources

Hg from historical anthropogenic emissions that has been previously deposited from the atmosphere to soil, water, and vegetation surfaces can be re-emitted back into the atmosphere. For this to occur, stable inorganic and organic Hg compounds in terrestrial and aqueous reservoirs must be converted into volatile Hg species, principally elemental Hg. After this occurs, re-emission is then generally dependent on temperature, with higher re-emission rates occurring at higher temperatures and lower re-emissions at lower temperatures. The amount of Hg deposited to soil, water, and vegetation surfaces is a mixture of natural, recently deposited current anthropogenic, and cycled anthropogenic Hg. However, according to **Amos et al. (2013)** only 10% of Hg deposited from the atmosphere to surfaces is estimated to be of natural origin, and the levels of atmospheric Hg have increased by 70% since the beginning of the industrial era.

One major pathway of Hg re-emission is through biomass burning; from 1997 to 2006 the average global re-emission of Hg due to biomass burning has been estimated at approximately 675 tonnes per year, accounting for 14% of total historical anthropogenic emissions **(Fig. 8) (Friedli et al. 2009).** Hg is deposited from the atmosphere onto plant surfaces by dry and wet deposition where it is assimilated into plant tissues by stomatal uptake. The major source of historical Hg emissions to the atmosphere is ocean basins. It is

generally assumed that elemental Hg is the major Hg species emitted to the atmosphere from surface waters.

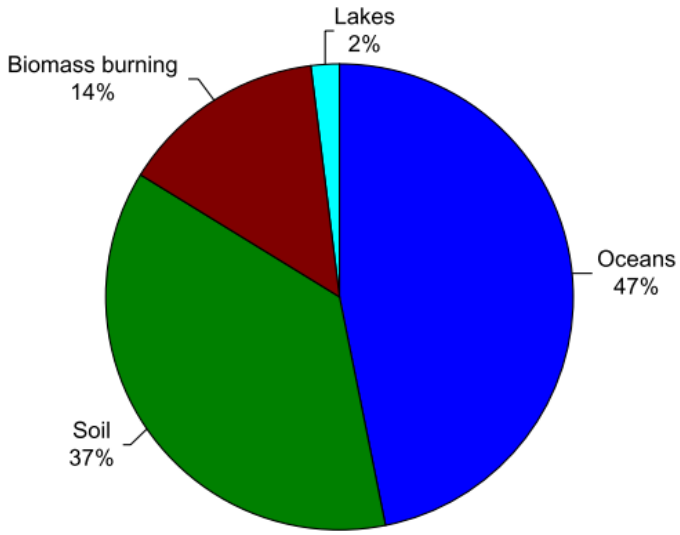

Figure 8: Relative contributions of estimated Hg emissions to the atmosphere from historical anthropogenic sources (Friedli et al. 2009).

3.2.3 Hg in terrestrial ore deposits

The rare element Hg is present in Earth's upper, middle, and lower crust at concentrations of ~0.05, 0.0079, and 0.014 ppm, respectively **(Rudnick & Gao 2004)**.

Hg is commonly distributed in most mineral deposit types that contain Zn. Zinc occurs mainly as independent minerals in nature and is typically closely associated with sphalerite **(Ozerova et al. 1975)**.

A review of the largest and/or best described Hg deposits of the world conducted by **Fein et al. (1977)** revealed that Hg deposits typically form at low temperature, commonly in epithermal environments and in most cases have close association with hydrocarbons or organic matter.

According to **Phelps & Buseck (1980)** and **Varekamp & Buseck (1984)** Hg ores are typically formed at shallow depths and relatively low temperatures between 100° and 200°C. The requirements for their deposition from a hydrothermal system are (i) a source rock enriched in Hg, (ii) high Hg solubility in a wide range of temperatures and fluid compositions and (iii) low Hg solubility in a restricted range of conditions. Deposition of Hg is usually correlated with active geothermal systems. Hg enrichments are found in hot spring halos and around sulfide ore bodies. Hg concentrations in hot springs can reach several tens of ppm. The

main factors for Hg deposition in dilute hydrothermal systems are cooling, increase of pO_2 and decrease in pH.

The principal geochemical mechanism for the concentration and precipitation of Hg minerals is hydrothermal reworking of marine black shales **(White 1981, Barnes 1997)**. The form of the Hg in black shales may be bound to organic matter, incorporated into pyrite, or present as a distinct Hg mineral such as cinnabar **(Hazen et al. 2012)**. Marine black shales are typically enriched in Hg compared to other sedimentary rocks **(Lehmann et al. 2004, Parsons & Percival 2005a, Sanei et al. 2012)**, probably as a consequence of the affinity of Hg for organic matter, notably through binding with organic thiols **(Xia et al. 1999, Hesterberg et al. 2001, Haitzer et al. 2002, Rytuba 2005)**.

For example, in China, Zn mineralization mainly occurs in four ore types, namely: sedimentary-exhalative deposits (SEDEX), Mississippi Valley-Type (MVT), volcanic hosted massive sulfides (VMS) and intrusion related (IR) types **(Dai et al., 2005)**. From these, SEDEX deposits have the highest Hg content ranging from 27 to 1198 ppm Hg **(Schwartz 1997)**. The reason may be due possibly to the relative higher Hg background in sediments providing the ore-forming fluid **(Yin et al. 2012).** VMS and MVT deposits have moderate Hg concentrations. In VMS deposits Hg minerals are generally not present and Hg is primarily present in solid solution within sphalerite, which can contain up to 41.1 wt % Hg in its structure **(Tauson & Abramovich 1980).** VMS deposits probably received Hg from a mantle source **(Yin et al. 2012)**. The mean Hg content from the major MVT deposits in China is 10.1 ppm. The source of Hg in MVTs may be the low-temperature hydrothermal solutions formed by diagenetic recrystallization of the carbonates. Generally, Hg exhibits a widespread association with organic material. Hg–bitumen deposits are among the largest Hg producers **(Peabody 1993)**. Hg deposits have certain features in common with MVT deposits: (i) the deposits formed at shallow depths (ii) the ore-forming fluids had low temperatures (usually <200 ˚C) and (iii) hydrothermal aquifers composed of sedimentary rocks played a major role in the ore- forming process. Finally, IRs have the lowest content of Hg (2.4 ppm Hg), possibly because of the high temperature in the fluid phase during Zn mineralization **(Yin et al 2012)**.

3.2.3.1 Hg-minerals

The Commission on New Minerals, Nomenclature and Classification (CNMNC) of the International Mineralogical Association (IMA) has approved eighty–eight (88) minerals, plus two (2) minerals published but not yet approved by CNMNC, in which Hg is an essential or important constituent **(Table 1)**. These species include native metals and intermetallic

alloys, halides, sulfides, arsenides, selenides, antimonides, tellurides, sulfosalts, oxides, carbonates, and sulfates, and occur in various magmatic, hydrothermal, evaporitic, and surface weathering environments **(Tunell 1968, White 1981, Barnes 1997, Parsons & Percival 2005a; 2005b, Hazen et al. 2012)**.

3.2.3.2 Hg in marine/submarine hydrothermal vents

Hg is very particle reactive and therefore has a short residence time in ocean water of about 350 yr **(Gill & Fitzgerald 1988)**. Hg in oceans occurs in the elemental form Hg^0, divalent form Hg^{2+}, methylmercury (CH_3Hg^{2+}), dimethylmercury [$(CH_3)_2Hg^0$] and particulate and colloidal Hg **(Mason & Fitzgerald 1993, Morel et al. 1998)**. In its elemental form, Hg is present in the oceans at concentrations $<5 \times 10^{-7}$ppm (**Emsley 1991, Li & Schoonmaker 2004**). However, Hg concentrations differ among global oceans: According to **Lamborg et al. (2002)** the average Hg concentration in oceans is about 1.5 picomolar (pM), while in contrast measurements from the Mediterranean **(Cossa et al. 1997)** and North Atlantic **(Mason et al. 1998)** are higher (2.5 pM and 2.4 pM, respectively). On the other hand, in the Pacific Ocean lower concentrations are reported (1.2 pM) **(Laurier et al. 2004, Sunderland & Mason 2007)**. Generally, Hg concentrations of ocean water below the thermocline are low and vary over only a small range (about 1–5 pM kg^{-1}) (**Gill & Fitzgerald 1988)**.

Stoffers et al. (1999) were the first who reported the occurrence of elemental Hg^0 on the seafloor from submarine hydrothermal vents from paralic hot springs in the Bay of Plenty, active geothermal area of Taupo volcanic zone in New Zealand. The abundance of Hg may be due to an enriched source in the underlying basement rocks or in volatiles rising from a subvolcanic magma. Liquid hydrocarbons and Hg are closely associated and this may be evidence for a common origin in the sedimentary basement, remobilized by hydrothermal fluids. **Miedaner et al. (2005)** conducted experiments proving that hydrocarbons could play a significant role in transporting Hg in natural systems, which may explain the high concentrations of metallic Hg in some crude oils, as well as the common occurrence of petroleum in epithermal Hg deposits.

Hydrothermal vents form in volcanically active areas, often on mid-ocean ridges; hydrothermal fluids in these vents can reach temperatures as high as 400°C under the high pressures of the ocean floor. As in terrestrial geothermal systems, high temperatures and

Table 1. IMA recognized Hg-minerals (Hazen et al. 2012).

Name	Formula
Cinnabar	HgS
Hg	Hg
Hyperchinnabar	HgS
Metachinnabar	HgS
Eglestonite	$[Hg^{1+}]_6\ O(OH)Cl_3$
Temagamite	Pd_3HgTe_3
Potarite	PdHg
Coloradoite	HgTe
Vaughanite	$Tl[Hg^{1+}]Sb_4S_7$
Aktashite*	$Cu_6[Hg^{2+}]_3As_4S_{12}$
Galkhaite	$(Cs,Tl)(Hg,Cu,Zn)_6(As,Sb)_4S_{12}$
Routheirite	$TlCu[Hg^{2+}]_2As_2S_6$
Tvalchrelidzeite	$[Hg^{2+}]_3SbAsS_3$
Atheneite	$Pd_2(As0.75Hg_{0.25})$
Tiemannite	HgSe
Eugenite	$Ag_{11}Hg_2$
Paraschachnerite	$Ag_{1.2}Hg_{0.8}$
Schachnerite	$Ag_{1.1}Hg_{0.9}$
Luanheite	Ag_3Hg
Moschellandsbergite	Ag_2Hg_3
Imiterite	Ag_2HgS_2
Perroudite	$5HgS{\cdot}Ag_4I_2Cl_2$
Balkanite	$Cu_9Ag_5HgS_8$
Calomel	HgCl
Schuetteite	$Hg_3O_2(SO_4)$
Petrovicite	$Cu_3HgPbBiSe_5$
Terlinguaite	$[Hg^{1+}][Hg^{2+}]OCl$
Weishanite	$(Au,Ag)_{1.2}Hg_{0.8}$
Gortdrumite	$Cu_{18}FeHg_6S_{16}$
Leadamalgam	$Hg_{0.3}Pb_{0.7}$
Arzakite*	$[Hg^{2+}]_3[(Br,Cl)_2S_2]$
Grechishchevite	$[Hg^{2+}]_3S_2BrCl_{0.5}I_{0.5}$
Kadyrelite	$[Hg^{1+}]_6Br_3O_{1.5}$
Lavrentievite	$[Hg^{2+}]_3[Cl_2S_2]$
Kuznetsovite	$[Hg^{1+}]_2[Hg^{2+}][(AsO_4)Cl]$
Kuzminite	$[Hg^{1+}]_2(Br,Cl)_2$
Poyarkovite	$[Hg^{1+}]_3OCl$
Corderoite	$[Hg^{2+}]_3Cl_2S_2$
Montroydite	HgO
Artsmithite	$[Hg^{1+}]_4Al(PO_4)_{1.74}(OH)_{0.26}$
Livingstonite	$HgSb_4S_8$
Edgarbaileyite	$[Hg^{1+}]_6[Si_2O_7]$
Moschelite	$[Hg^{1+}]_2I_2$
Shakhovite	$[Hg^{1+}]_4SbO_3(OH)_3$
Kleinite	$[Hg^{2+}]_2N(Cl,SO_4){\cdot}nH_2O$

Name	Formula
Belendorffite	Cu_7Hg_6
Capgaronnite	AgHgClS
Coccinite	$[Hg^{2+}]I_2$
Hakite	$Cu_{10}Hg_2Sb_4Se_{13}$
Tischendorfite	$Pd_8Hg_3Se_9$
Chursinite	$[Hg^{1+}]_3[AsO_4]$
Velikite	Cu_2HgSnS_4
Gruzdevite	$Cu_6[Hg^{2+}]_3Sb_4S_{12}$
Laffittite	$Ag[Hg^{2+}]AsS_3$
Marrucciite	$[Hg^{2+}]_3Pb_{16}Sb_{18}S_{46}$
Rouxelite	$Cu_2HgPb_{22}Sb_{28}S_{64}(O,S)_2$
Christite	$Tl[Hg^{2+}]AsS_3$
Tillmannsite	$Ag_3[Hg^{1+}]VO_4$
Iltisite	$[Hg^{2+}]S{\cdot}AgCl$
Kelyanite	$[Hg^{1+}]_{12}(SbO_6)BrCl_2$
Stalderite	$TlCu(Zn,Fe,Hg^{2+})_2As_2S_6$
Kolymite	Cu_7Hg_6
Donharrisite	$Ni_8Hg_3S_9$
Fettelite	$Ag_{24}[Hg^{1+}]As_5S_{20}$
Kenhsuite	$[Hg^{2+}]_3Cl_2S_2$
Danielsite	$(Cu,Ag)_{14}HgS_8$
Magnolite	$[Hg^{1+}]_2TeO_3$
Polhemusite	(Zn,Hg)S
Comancheite	$[Hg^{2+}]_{13}O_9(Cl,Br)_8$
Pinchite	$[Hg^{2+}]_5Cl_2O_4$
Terlinguacreekite	$[Hg^{2+}]_3Cl_2O_2$
Gianellaite	$[Hg^{2+}]_4SO_4N_2$
Mosesite	$\{[Hg^{2+}]_2N\}(Cl,SO_4,MoO_4,CO_3).]_2H_2O$
Mazzettiite	$Ag_3[Hg^{2+}]PbSbTe_5$
Daliranite	$Pb[Hg^{2+}]As_2S_6$
Grumiplucite	$HgBi_2S_4$
Simonite	$Tl[Hg^{2+}]As_3S_6$
Brodtkorbite	Cu_2HgSe_2
Radtkeite	$[Hg^{2+}]_3[ClIS_2]$
Aurivilliusite	$[Hg^{1+}][Hg^{2+}]OI$
Clearcreekite	$[Hg^{1+}]_3(OH)(CO_3){\cdot}2H_2O$
Deansmithite	$[Hg^{1+}]_2[Hg^{2+}]_3(CrO_4)OS_2$
Edoylerite	$[Hg^{2+}]_3(CrO_4)S_2$
Hanawaltite	$[Hg^{1+}]_6[Hg^{2+}][O_3Cl_2]$
Peterbaylissite	$[Hg^{1+}]_3[(OH)(CO_3)]{\cdot}2H_2O$
Szymańskiite	$[Hg^{1+}]_{16}Ni_6(CO_3)_{12}(OH)_{12}(H_3O)_8\cdot 3H_2O$
Tedhadleyite	$[Hg^{1+}]_{10}[Hg^{2+}]O_4I_2(Cl,Br)_2$
Vasilyevite	$[Hg^{1+}]_{20}[O_6I_3Br_2Cl(CO_3)]$
Wattersite	$[Hg^{1+}]_4[Hg^{2+}][(CrO_4)O_2]$
Vrbaite	$Tl_4[Hg^{2+}]_3Sb_2As_8S_{20}$

* Aktashite and arzakite are inadequately described species not yet IMA approved.

reducing conditions can leach elemental Hg from Hg-enriched substrate. Concentrations of Hg in hydrothermal fluids are found to be 1,000 times higher than that in ambient seawater **(Vetriani et al. 2005)**. As these geothermal fluids mix with cold, oxidized seawater, Hg^{2+} is formed, resulting in precipitation of cinnabar on the sea floor, enhancing Hg concentrations in the vicinity of the hydrothermal vents. This particulate Hg^{2+} can also be re-reduced to elemental Hg, releasing it back into the water column. It has been shown that thermophilic bacteria surrounding these hydrothermal vents are capable of reducing Hg^{2+} to elemental Hg^{0}, thus detoxifying the local environment while releasing the volatile elemental Hg into the open ocean where it can be carried to surface waters **(Vetriani et al. 2005)**.

Hein et al. (2005) report ferromanganese oxide crusts rich in Hg (up to 10 ppm) at water depths of 1,750 to 1,300 m from La Victoria knoll, California. Discrete Hg minerals or discrete minerals with high Hg content were not found. Hg was derived from leaching of organic matter-rich sediments from neighboring basins by hydrothermal fluids, and, to a lesser extent, from underlying continental basement rocks. The main fluid transport pathway was faults, and hydrothermal circulation was driven by high heat flow associated with thinned crust.

In New Zealand, substantial amounts of Hg metal, in the form of cinnabar, deposited in a shallow submarine geothermal environment, closely associated with liquid hydrocarbons may be evidence for a common origin from the sedimentary rocks of the basement. The presence of liquid hydrocarbons implies strongly reducing conditions that would allow for the transport of aqueous Hg in the reduced state, and the formation of liquid Hg droplets suggests that the submarine vents are close to saturation with $Hg^{0}_{(aq)}$ **Stoffers et al. (1999)**.

3.2.4 Hg bioaccumulation in the marine environment

Marine shallow-water hydrothermal discharges frequently precipitate large amounts of Fe and Mn oxide and sulfide minerals enriched in several trace elements, i.e. Fe, Zn, Ba, Pb **(Dando et al. 1999, Marani et al. 1997)**. However, some quantity of potentially toxic elements might remain dissolved in the surrounding seawater. This can contribute to the emergence of environmentally stressful conditions for biota near coastal hydrothermal venting sites, which can be potentially hazardous for the local human population **(Price & Pichler 2005, Francesconi & Edmonds 1993)**. It is known that for microbial communities thriving near shallow-water hydrothermal vents, hydrothermal fluids may serve as a source of bioessential metals (i.e. Cu, Zn, Mo, Mn, Fe etc) and nutrients (o, H, P, N, C) **(Tarasov et al.**

2005); marine life, such as seaweeds, are capable of accumulating high concentrations of potentially toxic elements and may subsequently transfer them up to higher levels in the food chain **(Rahman et al. 2012, Philips 1994, Jayasekera & Rossbach 1996)**.

Microbial communities are known to convert Hg^{2+} to methylmercury (CH_3Hg^{2+}) and dimethylmercury [$(CH_3)_2Hg^0$], which significantly affects the near-surface geochemical cycling of Hg **(Compeau & Bartha 1985, Choi et al. 1994, Morel et al. 1998, King et al. 2000, Goulding et al. 2002, Gray et al. 2004, Krabbenhoft et al. 2005, Kritee et al. 2008; 2009)**. In both aquatic and coastal sediments, microbes and sulfate-reducing bacteria respectively, are the main agents controlling methylmercury production (**Gilmour et al. 1992**, **Compeau & Bartha 1985**, **King et al. 1999).** The timing of this microbial innovation of Hg methylation is as yet unknown. Living organisms accumulate methylmercury which is biomagnified through the food chain. By this is meant that the Hg amounts predators obtain by eating contaminated preys are higher than those contained in their food (**Monteiro et al. 1996**). Microbes also may have a significant effect on Hg mineralization through their metabolic byproducts.

Leal-Acosta et al. (2013) studied the seaweed contamination by Hg in the shallow-water marine ecosystem of Concepcion Bay in the western Gulf of California, which was at a moderate level, constituting an anomaly in the sediments neighboring the vent.

There is very little information on the methylmercury levels of hydrothermal vent fauna; **Martins et al. (2001)** reported that the methylmercury in hydrothermal mussels (B. azoricus) was under the detection limit (<6 ng g^{-1}) and the methylmercury concentration in hydrothermal mollusks from Tonga Arc (Pacific Ocean) was extremely low **(Lee et al. 2015)**. One explanation for this could be the low Hg methylation in the hydrothermal vent environments. The role of endosymbiotic bacteria in mussels and snails cannot be excluded as an explanation for the low methylmercury accumulation, particularly in gills and digestive glands that show lower % methylmercury than other organs, in general. Hg could be reduced to a less toxic form of Hg^0 by mercuric reductase, a prominent detoxifying enzyme in the bacterial kingdom **(Colaço et al. 2006, Lee et al. 2015).**

3.3 Silver in the geoenvironment: what we know and what we don't know

Silver (Ag) is the 47th element in the periodic table having an atomic weight of 107.8. It also has two isotopes: 106.90 Ag and 108.90 Ag in 52% and 48% abundance, respectively

(**Panyala et al. 2008**). Silver occurs naturally in the earth's crust, usually in quite low concentrations (**Janes & Playle 1995, Urcell & Eters 1998**) (average concentration around 0.1 mg kg^{-1} (**Etris 1997, Renner 1993, Lockhart 1983**)). Silver occurs in the environment in four oxidation states: 0, 1+, 2+ and 3+. Oxidation states 0 and 1+ are the most common, while 2+ and 3+ are present only naturally in the environment (**Etris 1997, Urcell & Eters 1998**).

It is proven that silver is one of the most toxic, easily accumulated trace metals, coming next after Hg (**Luoma et al. 1995, Ratte 1995, Reinfelder & Chang 1999, Barriada et al. 2007, Gallon & Flegal 2014**). The extent of silver toxicity ranges, depending on silver species or compound (**Cooper & Jolly 1970, LeBlanc et al. 1984, Janes & Playle 1995, Urcell & Eters 1998**). Silver is listed in the 1977 US EPA (Environmental Protection Agency) priority pollutant list and in the EEC 1976 Dangerous Substance Directive List II (76/464/EEC), so silver discharges are under regulation (**Fabrega et al. 2011**). Despite silver's significance, there is a scarcity of data for its global biogeochemical cycle, so a brief summary of studies concerning silver is following.

3.3.1 Health effects caused by silver

Even though silver was thought to be harmless, high exposure to silver compounds may cause "*argiria*", an irreversible condition which results is deep-blue/grey skin discoloration by Ag deposition in body tissues (**Hill 1941, Rosenman et al. 1979, Panyala et al. 2008, Fabrega et al. 2011, Reidy et al. 2013**). Another possible effect of silver is affecting the population size of specific bacteria species living in gut microflora (**Sawosz et al. 2007**, **Fabrega et al. 2011**).

Apart from health effects in humans, dissolved silver ions are highly toxic to prokaryotes, marine invertebrates and fish (**Bianchini et al. 2002, Erickson et al. 1998, Fisher & Wang 1998, Hogstrand & Wood 1998, Fabrega et al. 2011**).

3.3.2. Silver in marine/submarine hydrothermal systems

Silver-rich submarine hydrothermal systems are not common. **Iizasa et al. (2004)** report a Ag-rich active dacite-hosted submarine hydrothermal field associated with sulfide chimneys less than 10 m high in the Bayonaise Knoll caldera which is located in a nascent rift zone west of the Izu-Ogasawara (Bonin) volcanic arc, Japan. The main hydrothermal field is

500m×700m across and is located at a water depth of 820 to 680m. The deposit contains on average 37.2% Zn, 3.1% Pb, 1% Cu, 5.6% Ba, 6 ppm Au, 692 ppm Ag, 1310 ppm As and 14 ppm Hg **(Glasby et al. 2008)**.

Low-temperature Zn-rich chimneys (~122 °C) of the hydrothermal system at Brothers volcano, Kermadec intraoceanic arc (New Zealand) contain a suite of elements seen in epithermal environments, including Ag, Sb and Ga (up to ~1000 ppm), As (up to ~1 wt %), Pb (up to ~1.2 wt %) and Hg (up to ~102 ppm) **(De Ronde et al. 2011).**

3.3.3 Silver occurrence in the environment

Apart from mineral deposits, silver is found on land, in areas where silver has been deposited because of human activity, in the atmosphere as a result of coal mining activities and smelting, or in aquatic environments as the results of erosion, mining and industrial waste, or in sewage treatment plants **(Lockhart 1983, The Silver Institute 1995, CPM Group 1995, Scow et al. 1995, Urcell & Eters 1998**). According to **Scow et al. (1995)** estimations of Ag disposal in 1978, were 4% to the air, 39% to water and 68% to land. Industrial silver releases to the environment are shown in **Figure 9**.

The majority of studies on silver concern its occurrence in aquatic (**Fabrega et al. 2011**) and especially marine environments after anthropogenic inputs (**Barriada et al 2007**, **Morford et al. 2008**, **Gallon & Flegal 2014, Reidy et al. 2013**). Concentrations of Ag in surface oceanic waters are controlled by riverine, atmospheric and anthropogenic contribution (**Klein & Mulvey 1978, Ndung'u et al. 2001, Zhang et al. 2001, Ranville & Flegal 2005, Morford et al. 2008**).

The monovalent ion is usually found in surface waters in the form of sulfide, bicarbonate, sulfate salts, or absorbed in organic or inorganic materials (**Urcell & Eters 1998**).

Silver accumulation in marine sediments is controlled by Ag flux to sediments and sediment conditions which may or may not help authigenic accumulation to occur (**Morford et al. 2008**).

In soils, silver occurs as sulfides, associated with iron, lead or tellurides and sometimes is found with gold (**Urcell & Eters 1998**).

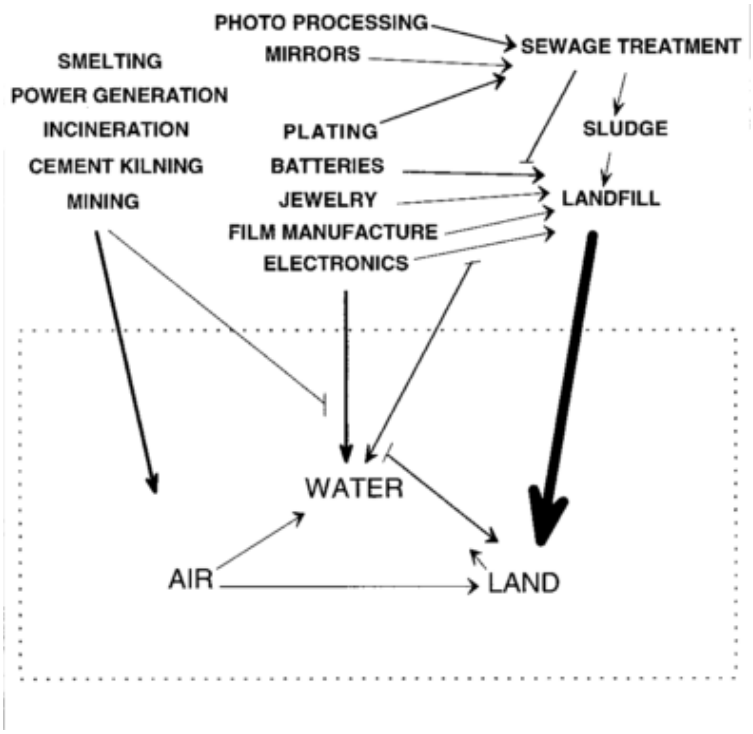

Figure 9: Silver input to the environment from industrial applications. The arrow sizes indicate the total amount of silver flowing to each environmental receiver (Urcell & Eters 1998).

3.3.4 Transport of silver in magmatic-hydrothermal systems

The ore fluid in many magmatic-hydrothermal systems may be composed in significant part and even predominantly by a hydrothermal vapor **(Henley & McNabb 1978, Heinrich et al. 2004, Williams-Jones & Heinrich 2005, Mavrogenes et al. 2010)**. Water vapor can dissolve weakly volatile metallic compounds in concentrations that are orders of magnitude greater than predicted by their volatility **(Galobardes et al. 1981, Bischoff et al. 1986, Armellini & Tester 1993, Williams-Jones et al. 2002)**. This ability of water vapor to dissolve metals may be attributed to its highly non-ideal behavior, which allows it to form gaseous hydrogen-bonded H_2O clusters (e.g., $AgCl:(H_2O)_n$) in which n is the hydration number, i.e., the number of molecules in the hydration shell **(Galobardes et al. 1981, Armellini & Tester 1993, Migdisov et al. 1999; Archibald et al. 2001; 2002)**.

Vapor-rich fluids are capable of transporting tens of ppm of Ag **(Audetat et al. 1998, Ulrich et al. 1999)**. Hydration numbers do not change significantly with pressure and at any given temperature, the compound of interest can be described by the presence of one predominant H_2O cluster **(Migdisov et al. 1999, Archibald et al. 2001)**. The ability of water vapor to transport metals increases with the hydration number. Silver reaches its highest concentration (86.06 ppm) in chlorine-bearing water vapor in the temperature range 400–

550˚C. This would therefore be the optimum temperature range for the transport of silver as AgCl–water clusters in low density hydrothermal fluids. However, deposition of silver from such fluids would also occur at lower temperature. Significantly, in a number of silver-bearing ore deposits, a low density hydrothermal fluid is interpreted to have transported or deposited Ag at temperatures similar to those referred above (e.g. fluid inclusion data from Mole Granite, Australia contained up to 108 ppm Ag at temperatures between 400 and 530˚C **(Audetat et al. 2000a;b)**. The solubility of silver chloride in low-density aqueous fluids can be explained by the formation of hydrated clusters $AgCl:(H_2O)_n$. The data also suggest that the hydration number of the predominant cluster increases systematically with increasing pressure, and that each of the gaseous solutions contains a mixture of different clusters that predominate at different pressures **(Migdisov & Williams-Jones 2013)**.

3.3.5 Silver bioaccumulation

Silver ions have such chemical properties that can be bioconcentrated in organisms (bacteria, fungi and plants), passing through their cell walls and reaching the plasma membrane (**Luoma 2008, Fabrega et al. 2011**). The production of diatoms and dinoflagellate remove Ag from surface waters by adsorption or incorporation as being developed (**Fisher & Wente 1993, Morford et al. 2008**). Although silver nanoparticles contained in consumer products do not have any proven negative direct effects to humans, they may be bioaccumulated indirectly, after being released in the environment (**Benn & Westerhoff 2008, Geranio et al. 2009, Gottschalk et al. 2009, Woodrow 2009, Fabrega et al. 2011**).

Luoma & Rainbow (2005) stated that both bioavailability and bioaccumulation of Ag nanoparticles are dependent on the combination of (i) their concentration, (ii) their nature, (iii) the environment's nature, (iv) the route of exposure, (v) the biology and functional ecology of the involved organism(s). **Navarro et al. (2008)** added that the bioavailability and bioaccumulation of Ag nanoparticles by every organism depend on the size, shape, chemical composition, charge, surface structure and area, solubility and aggregation state of the particle or material. The same authors also noted that the aggregation or stabilization of Ag nanoparticles is affected by the interaction of pH, ionic strength, composition, temperature, nanoparticle composition and natural organic macromolecules.

4. Hg and silver in the unique shallow–submarine volcano, Kolumbo (Santorini), Hellenic Volcanic Arc (HVA)

4.1 Geodynamic and geological setting of the HVA

The Santorini-Kolumbo volcanic-tectonic field forms part of the central HVA **(Fig. 11)**. The 5 Ma-to-present Hellenic Volcanic Arc (HVA) belongs to the Hellenic orogenic arc, which is located along the convergent plate boundary of the northwards subducting African plate underneath the active margin of the European plate (**Angelier 1979, Dewey et al. 1973, Le Pichon & Angelier 1979, McKenzie 1972, Ninkovich & Hays 1972, Nomikou et al. 2013**). The HVA exemplifies a unique case of volcanism and hydrothermal activity occurring on thinned continental crust in a setting of convergent boundaries: the Hellenic Subduction System (HSS) (**Fig. 10**) (**Kilias et al. 2013**). Specifically, the HSS represents a totally different situation from the typical Pacific geodynamic setting (**Kearey et al. 2009**) because the Cretan basin separates the Hellenic Sedimentary Arc (HSA) (Peloponnesus, Crete, Rhodes) from the HVA (Methana, Milos, Santorini, Nisyros) (**Fig. 11**) **(Kilias et al. 2013)**. Cretan basin is a "back-arc" mollasic basin (Middle-Late Miocene – Quaternary age) which is the result of extension north of Crete, while in contrast the Hellenic trench and fore arc basin of the HSS south of Crete is dominated by compression (**Le Pichon & Angelier 1979**).

The volcanic activity along the main volcanic centers of the HVA (Methana-Poros, Milos, Santorini, Kos, Nisyros) lasted from Pleistocene until the Holocene (**Fytikas et al. 1984**). Apart from the onshore volcanoes (Soussaki, Methana, Aegina, Milos, Santorini, Nisyros, Kos), submarine ones occupy a significant area in the active HVA either in the form of independent features or as an offshore continuation of the volcanic islands. Some of the studied submarine volcanoes and hydrothermal vents of the HVA are: i) Paphsanias submarine volcano in the Methana group, ii) three volcanic domes to the east of Antimilos Volcano and hydrothermal activity in southeast Milos in the Milos group, iii) three volcanic domes east of Christiana and a chain of about twenty volcanic domes and craters in the Kolumbo zone northeast of Santorini in the Santorini group and iv) several volcanic domes and a volcanic caldera together with very deep slopes of several volcanic islands in the Nisyros group (**Nomikou et al. 2013**).

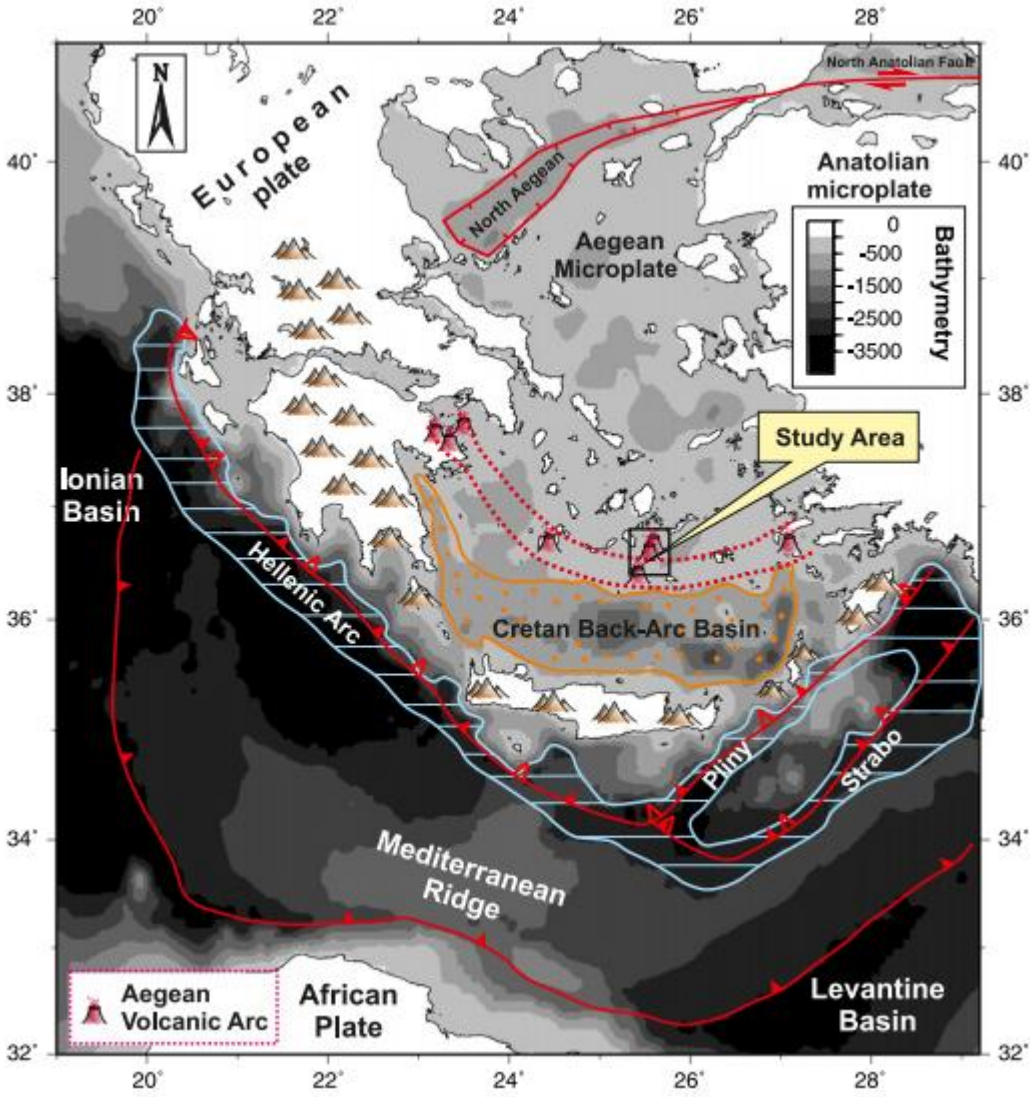

Figure 10: Location of study area in the center of the Aegean Volcanic Arc. The modern Aegean volcanic arc is developed behind the Hellenic Arc, the Peloponnese–Crete island arc and the Cretan back-arc basin. The African plate to the south subducts beneath the Eurasian plate to the north along the red lines just to the south of Crete. Yellow arrows indicate the GPS rates (approximately 40 mm/y) of the Aegean towards the African plate (considered stable) (modified after Nomikou et al. 2013).

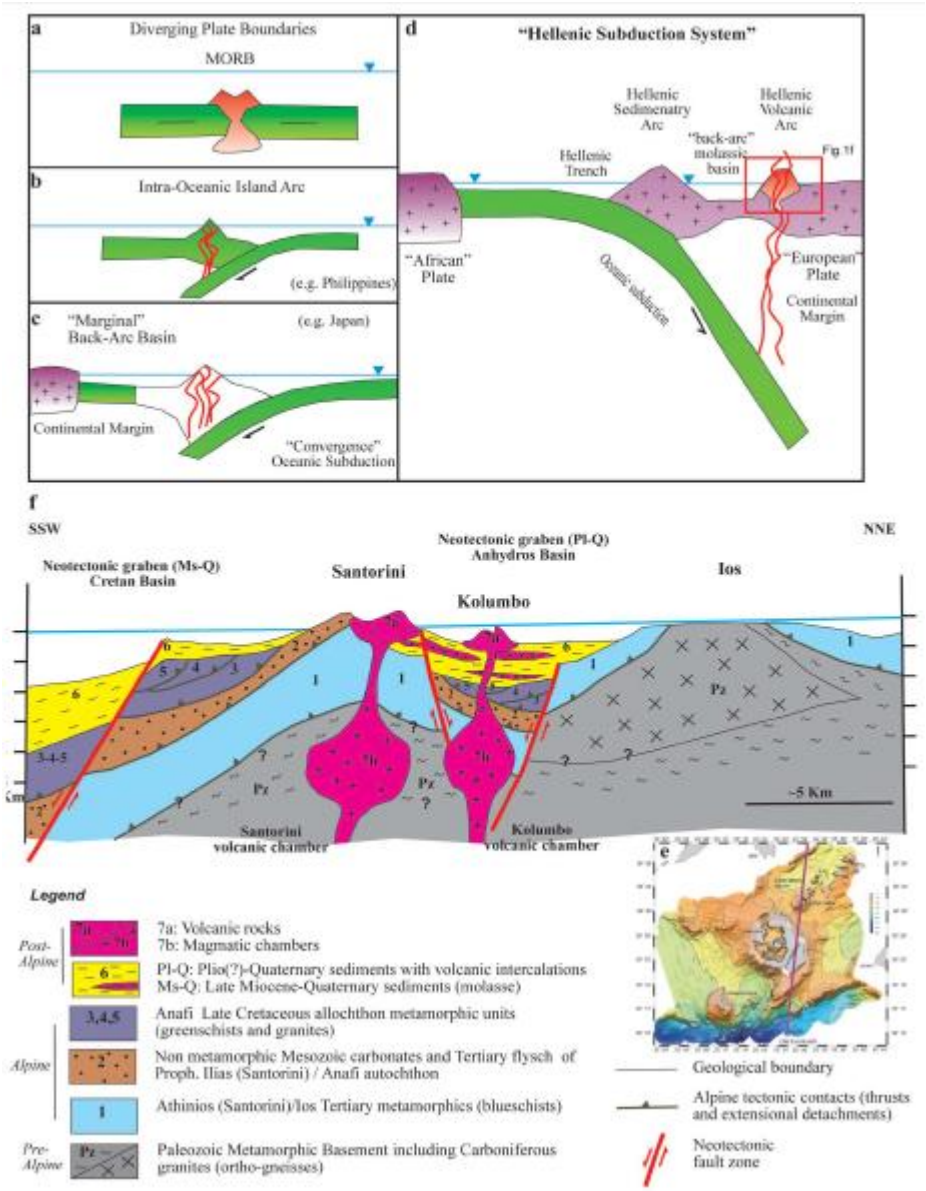

Figure 11: Geodynamic setting of the Santorini - Kolumbo volcanic field. (a–d): Schematic cartoons of different geodynamic environments where seafloor hydrothermal vents occur. (a) Mid-Ocean Ridges along divergent plates. (b) Intra-Oceanic Arcs within convergent boundaries (e.g. Philippines). (c) Marginal back-arc basins and island arcs along active continental margins with oceanic subduction (e.g. Japan). (d) ''Hellenic Subduction System''. The ''Hellenic Volcanic Arc'', within active continental margin, developed behind the molassic back-arc basin, hosted over thinned continental crust. (e) Swath bathymetry map of Santorini-Kolumbo volcanic field (modified after ref. 5- permission to publish the original map was provided by Elsevier Science) and location of the geological transect (red line). (f) Schematic cartoon depicting the geological cross section through the Hellenic Volcanic Arc, from the molassic back-arc Cretan Basin to the Cycladic island of Ios in the back-arc area (Kilias et al. 2013).

4.2 The Kolumbo submarine volcano and hydrothermal system

The Santorini-Kolumbo volcanic group comprises three distinct volcanic structures occurring along a NE–SW direction. Christiana form the southwestern part of the group, Santorini occupies the middle part and Kolumbo extends towards the northeastern part **(Fig. 12)**. Kolumbo volcanism, tectonism and hydrothermal activity occurred along the aforementioned NE-SW tectonic zone named as Christianna-Santorini-Kolumbo (CSK) line **(Nomikou et al. 2013)**.

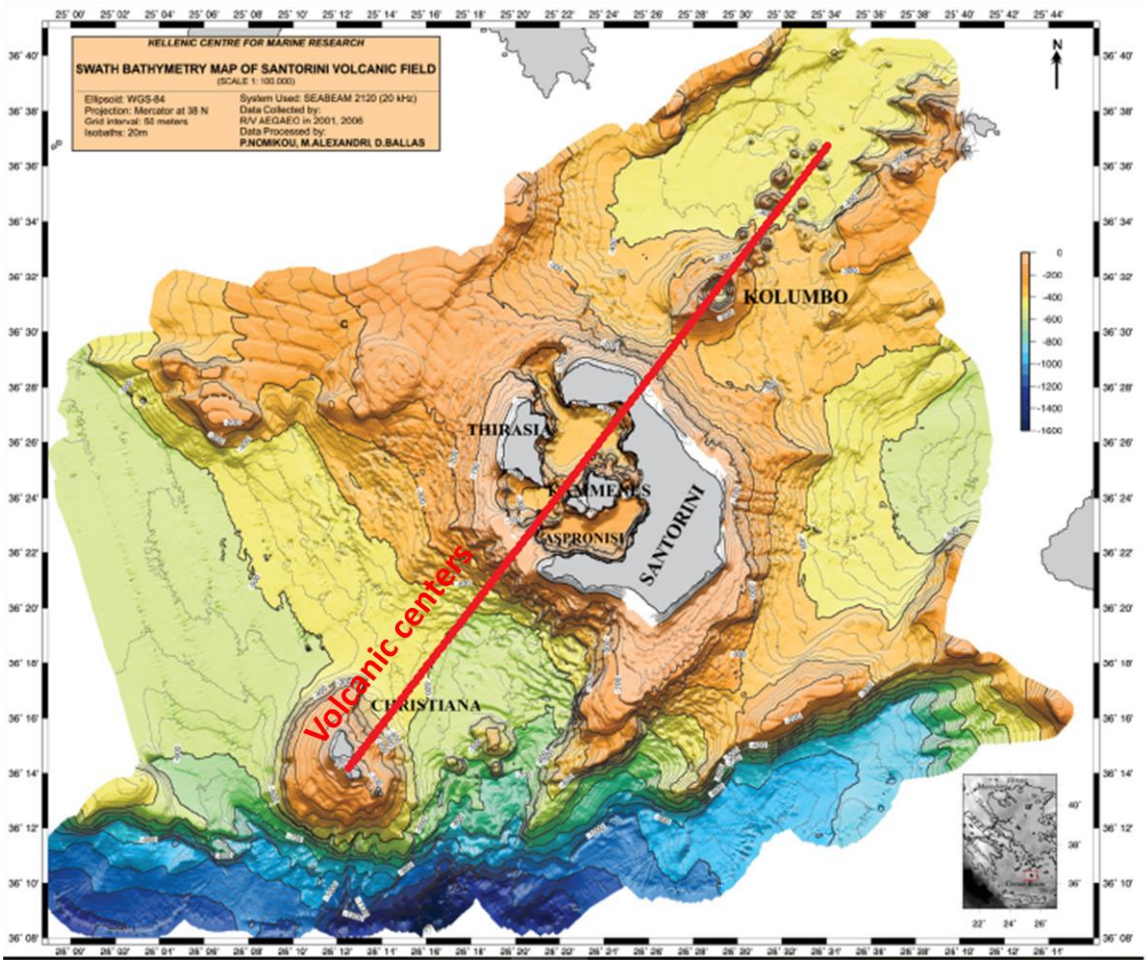

Figure 12: Swath bathymetry map of Christianna-Santorini-Kolumbo volcanic field (CSK) and tectonic zone (red line) (Nomikou et al. 2013).

4.2.1 Kolumbo volcanic field

Kolumbo underwater volcano is located 7 km north-east of Thera, the main island of Santorini volcanic group, in the southern Aegean Sea (**Figs. 10, 12, 13**). According to **Nomikou et al. (2013)** more than 20 volcanic cones are present north-east of Kolumbo, which

appear to be aligned along two distinct linear trends (N 29°E and N42°E) that converge at the point of the Kolumbo crater**.** Cones of the northerly trend are generally larger, but vary in size towards the northeast, whereas cones in the easterly trend are smaller and more uniform in size. In addition, the size and the height of the volcanic domes generally decrease toward the northeast, indicating that the volcanic activity diminishes as the distance from Kolumbo increases (**Nomikou et al. 2013**). The diameter of the approximately 500-m-deep Kolumbo's crater is 1700 m, with the shallowest part of its rim lying just 18 m below sea level (**Perissoratis 1995, Sigurdsson et al. 2006, Nomikou et al. 2013**).

Kolumbo's crater walls expose stratified pumiceous deposits at a depth of 270-250 m which continues to 150 m, above which the deposits are obscured by loose talus and bacterial overgrowths (**Carey et al. 2011, Kilias et al. 2013**). The entire crater floor of Kolumbo is covered by orange to brown smooth sediment with a few-cm-thickness **(Carey et al. 2010)** consisting of Fe-encrusted flocculent microbial mats and amorphous Fe-oxyhydroxide deposits (**Kilias et al. 2013**). Temperature in the Fe-rich sediment ranges between 16.2°C and 17°C. Small pockmark-like craters from the Fe microbial mat release clear, low-temperature fluids (≤70°C) and CO_2 gases (**Kilias et al. 2013**).

Kolumbo erupted in 1650 CE following one year of strong earthquake activity (**Fouque 1879**). Seismic profiles provide evidence that Kolumbo was shaped due to at least four eruptive cycles (**Fig. 14) (Hübscher et al. 2015)**. The lower part of the present Kolumbo cone is formed by layered or massive lava flows. The upper part of the cone is composed of tephra deposits produced during the 1650 eruptive phase. This interpretation has been verified by repetitive ROV dives in the Kolumbo crater and at different sites of the inner crater walls (**Nomikou et al. 2013**).

The eruption of 1650 was an explosive eruption of gas-rich magma. The eruption column of ash and pumice raised high above the volcano and created pyroclastic flows and pyroclastic surges that passed over the sea surface, spreading several kilometers distance over the ocean in all directions. At least fifty people and over a thousand livestock died from asphyxiation on Santorini at NE areas near the volcano (**Fouque 1879**). Some people went to the coast out of curiosity to see the eruption, but they were greatly affected by gas clouds and as a consequence some died. The Kolumbo pyroclastic surges passed over the sea reaching the north-east coast of Santorini, about 7 km away, as very dilute but still hot, lethal and gas-rich clouds of ash (**Nomikou et al. 2013**).The explosive eruption was followed by one year of strong earthquake activity (**Fouque 1879**). The resulting tsunami caused significant

destruction on the east coast of Santorini and adjacent islands (**Dominey–Howes et al. 2000, Nomikou et al. 2013**).

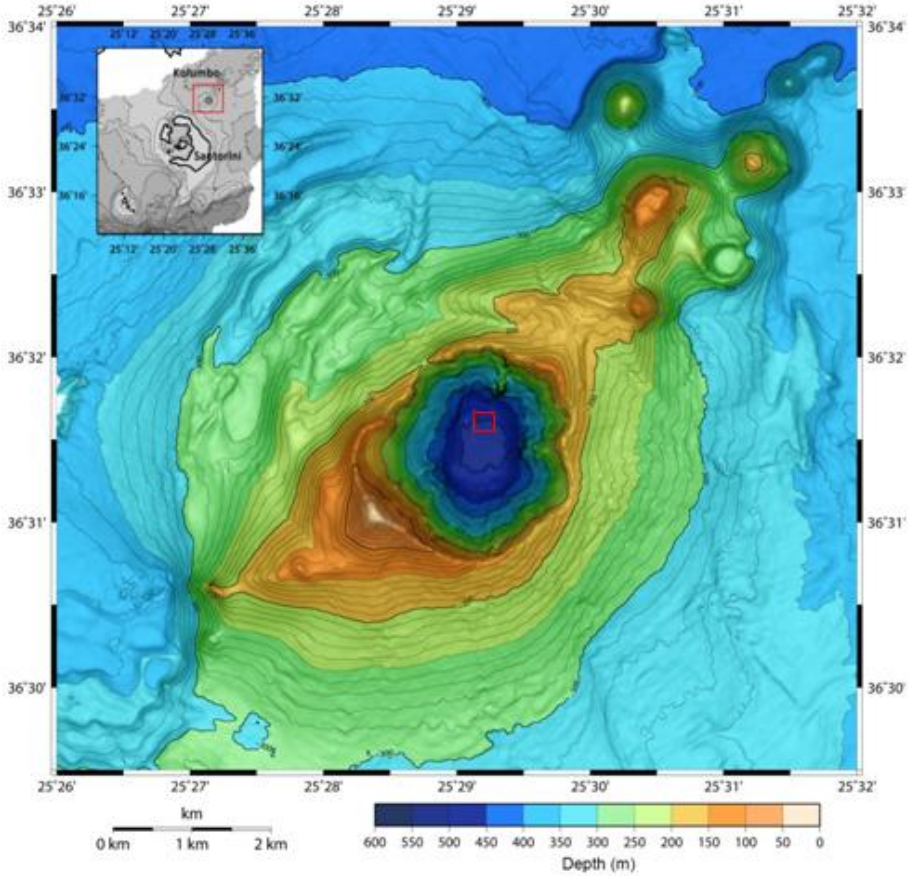

Figure 13: Swath bathymetry of Kolumbo volcano (modified after Nomikou et al. 2013). (The red square is the area of which a detailed bathymetric map of Kolumbo hydrothermal vent field is given in Figure 16).

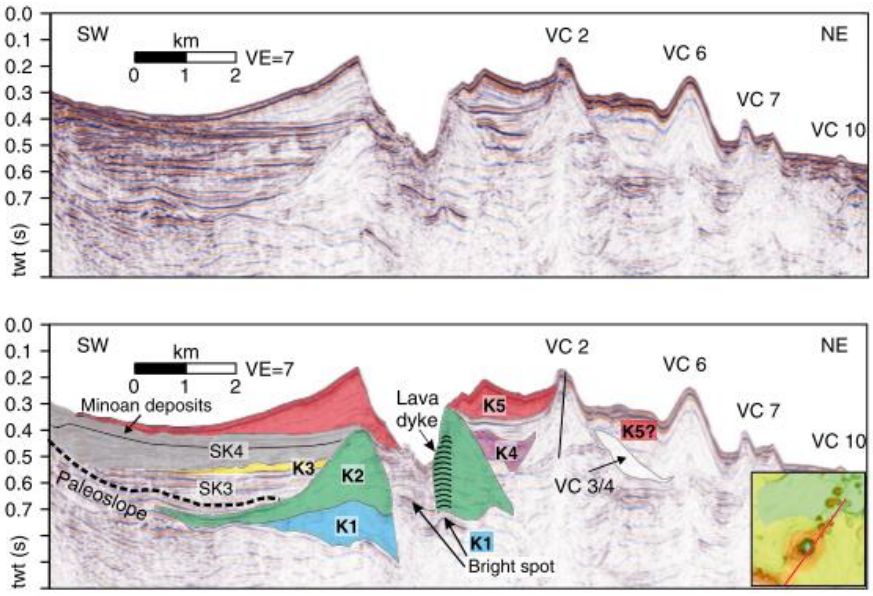

Figure 14: SW-NE striking multi-channel reflection seismic profile across Kolumbo. Upper part shows seismic data, lower part shows interpretation. Grey shaded area smark pyroclastic flows or mass-transport deposit. K1-K5: the five circular stratigraphic units labeled bottom-up. SK3 and SK4 refer to intercalated units. VC: Volcanic Cone. VC numbers according to Nomikou et al. (2013). (Hübscher et al. 2015).

4.2.2 Kolumbo hydrothermal field

In 2006, Remotely Operated Vehicle explorations in the northern part of Kolumbo's crater floor revealed an extensive ''diffuse-flow''-style hydrothermal vent field, Kolumbo Hydrothermal Field (KHF), between 492 and 504 m depth **(Fig. 13) (Sigurdsson et al. 2006)**. According to **Sigurdsson et al. (2006)** and **Kilias et al. (2013)**, the seafloor expressions of the KHF**,** consist of active and inactive sulfide-sulfate structures such as mounds, flanges, vertical spires and pinnacles that lie along a NE-SW trend, sub-parallel to the Christiana-Santorini-Kolumbo (CSK) tectonic zone. These vents **(Fig. 15)** are surrounded by sites of low-temperature (≤70˚C) diffuse venting from the Fe-mats. "Politeia Vent Complex" is a typical example of a spire-type vent extending over an area of 5×5 m, in the western part of the Kolumbo hydrothermal field. "Politeia Vent Complex" consists of short (≤3 m tall), slender, intermediate-temperature diffusely-venting, isolated and/or merged, sulfide-sulfate spires or "diffusers" **(Fig. 15a) (Kilias et. al 2013)**. These spires usually decrease gradually on their top and rise up from a hydrothermal mound, growing directly on the sediment and Fe-mat-covered seafloor. "Diffuser" spires release clear, almost free-of-particles fluids, from which sulfide minerals have precipitated prior to discharge (**Fig. 15b**) (**Hannington et al. 2005, Kilias et al. 2013**). Almost the same vents have been observed at shallow-water boiling vents on the Tonga arc, SW Pacific, the Juan de Fuca Ridge, and the Mid-Atlantic Ridge near Iceland (**Hannington et al. 2001, Kilias et al. 2013**). Grayish suspended filamentous microbial biofilms (streamers) cover the exterior of the "Politeia" spires (**Kilias et al. 2013**).

In the central part of the vent field smooth-sided sulfide-sulfate mounds are located: the "Champagne Vent Complex" (**Fig. 15b**) and the "Diffuser II Vent Complex" (**Fig. 15c**), which are covered by orange to brown Fe-rich microbial mats and consist of a basal mound without spire structures. Typically, bubble streams (mainly CO_2) are emitted from small holes and cracks on their sides and bases. Carbon dioxide gas dissolution causes accumulation of density-stratified water enriched in CO_2, and acidic seawater (pH≈5), for ~ 10–15m above the vents (**Carey et al. 2013**, **Kilias et al. 2013**). In 2010 the highest vent fluid temperature was measured, reaching 210˚C. At the northern crater slope, the largest hydrothermal chimney (height ~4 m) covered by Fe microbial mat ("Poet's Candle") was observed (**Fig. 15d**) (**Kilias et al. 2013**).

Additionally to the previous explorations, more Remotely Operated Vehicle explorations conducted in 2013, by collecting chimneys around the Champagne Vent

Complex area **(Figs. 15e, f, g, h)**. Most of these chimneys discharge gases and fluids, which are the typical features of Champagne Vent Complex.

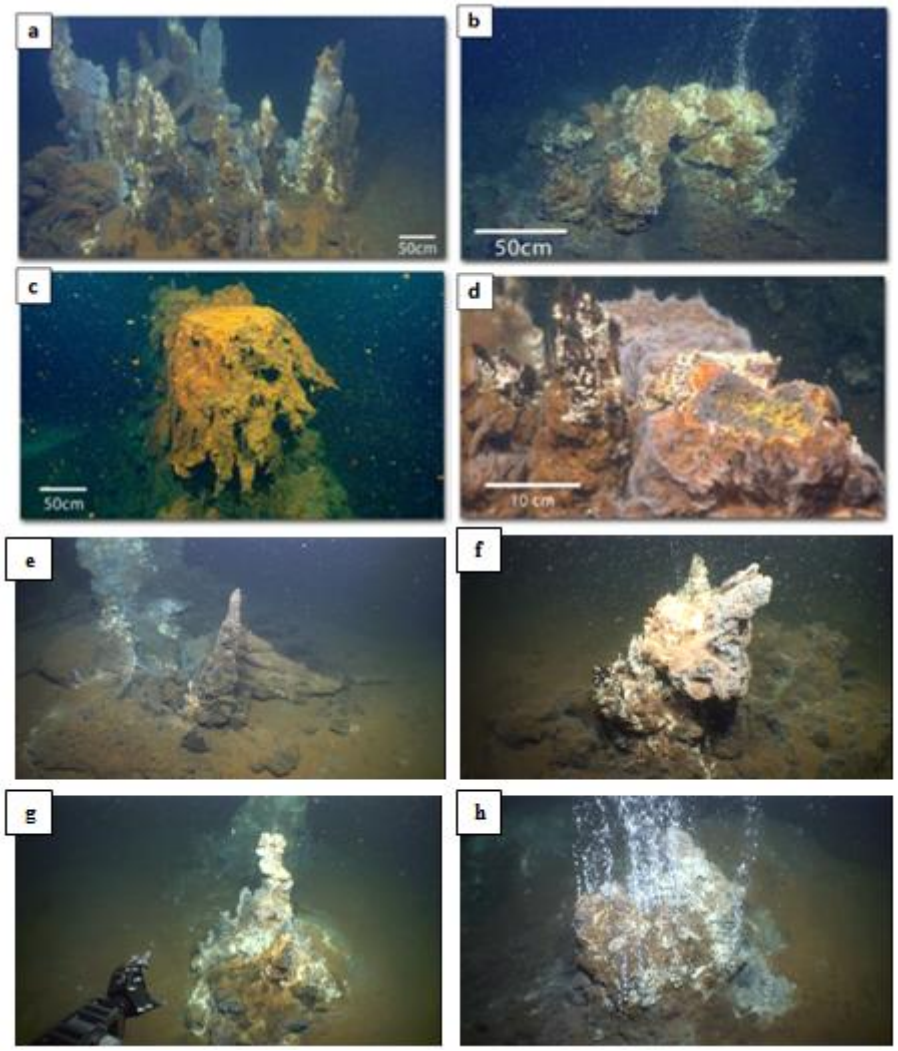

Figure 15: a. "Politeia Vent Complex": Field of multiple inactive and active sulfide/sulfate, spires up to 2 m high on top of a hydrothermal mound with spire fragments draped by Fe-bearing bacterial mats. Clear fluids vent from active spires (not visible). b. "Champagne Vent Complex": Active high-temperature (220°C) vent discharging both gases (>99 % CO_2) and fluids. c. "Diffuser II Vent Complex": Vent with bacterial covering and gas bubbling. d. "Poet's Candle": The largest observed (height ~ 4 m) inactive vent with bacterial covering (Kilias et al. 2013). e. Sulfide/sulfate spire on the top of a hydrothermal mound from the vent V16b. f. Vent with slight gas discharging from V08. g. Vent displaying gas bubbling from V59(2). h. Active vent discharging gases and fluids from the vent V65 (for vent location see Figure 16).

5. Materials and methods

The samples studied in this thesis were collected on the 3rd of September 2013 during the EU-funded oceanographic expedition "2-BIOTECH SAMPLING EVENT" of the "SeaBioTech" EU-FP7 project (Grant Number 311932) {http://spider.science.strath.ac.uk/seabiotech/index.php}. The expedition took place from 2 to 10 September 2013. The chief scientist of the expedition was Dr Paraskevi Polymenakou of

the Hellenic Centre Marine Research (HCMR). The survey was conducted with the Remotely Operated Vehicle (ROV) Max Rover onboard oceanographic vessel Aegaeo of the HCMR.

5.1 Sampling

Sampling campaign and methods are detailed in HCMR's "SeaBioTech Report 2013", and, vent and sample location and recovered samples are shown in **Figures 15 e-h, 16, 17, 18, 19, 20, 21**. The studied samples are characterized by four mineralogical zones according to the classification of **Kilias et al. (2013)**: (a) a thick porous "inner sulfide-sulfate core" (ISSC), (b) an earthy thin orange-yellow outer As-sulfide-dominated layer (OAsL), (c) an orange to brown Fe-(hydrated)-oxyhydroxide-dominated microbial surface Fe crust (SFeC) and (d) interior hydrothermal conduit networks are lined by unidentified Sb-Zn-S phases (IPCN).

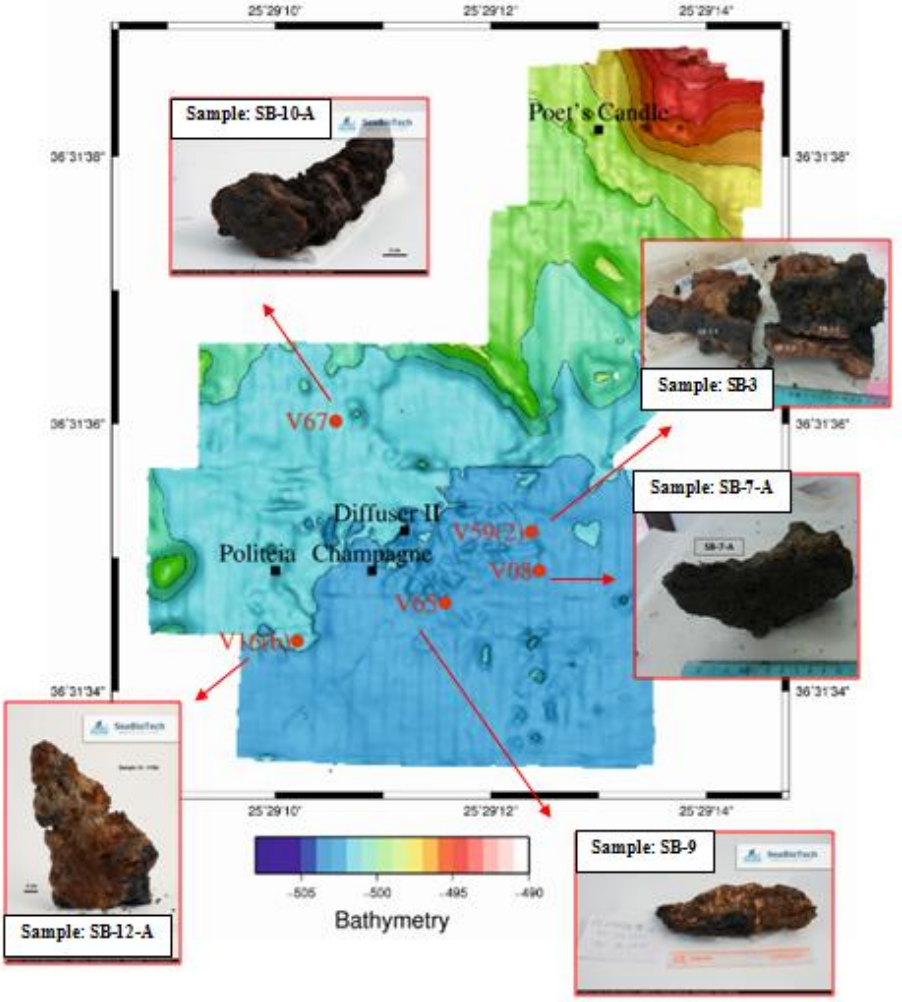

Figure 16: Detailed bathymetric map of Kolumbo hydrothermal vent field located in the northern part of the crater floor (red square in Figure 13) (modified after Kilias et al. 2013), with the locations of hydrothermal vents, Politeia, Champagne and Diffuser II, and the samples studied in this MSc thesis along with ex situ photographs immediately after recovery from the sea.

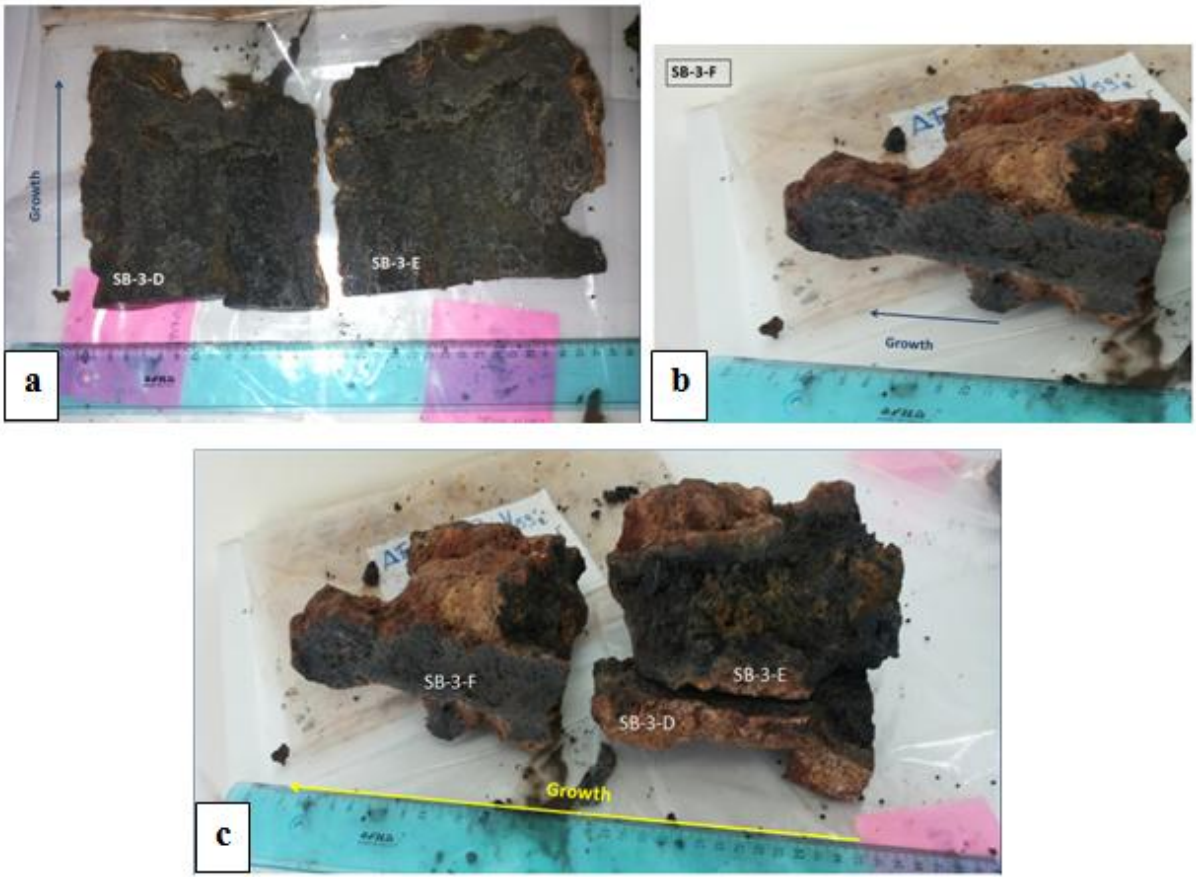

Figure 17: Ex-situ photographs of broken off and/or sectioned parts (SB-3-D, SB-3-E, SB-3-F) of sample SB-3 with marked bottom-up growth orientation. (a) Samples SB-3-D and SB-3-E represent the ISSC zone. (b) Sample SB-3-F is the top part of this hydrothermal chimney. (c) Individual samples assembled together to represent original positions in chimney sample SB-3. The brown exterior surface of the samples represents the OAsL zone.

Figure 18: Ex-situ photograph of sectioned chimney sample SB-7-A representing the ISSC zone.

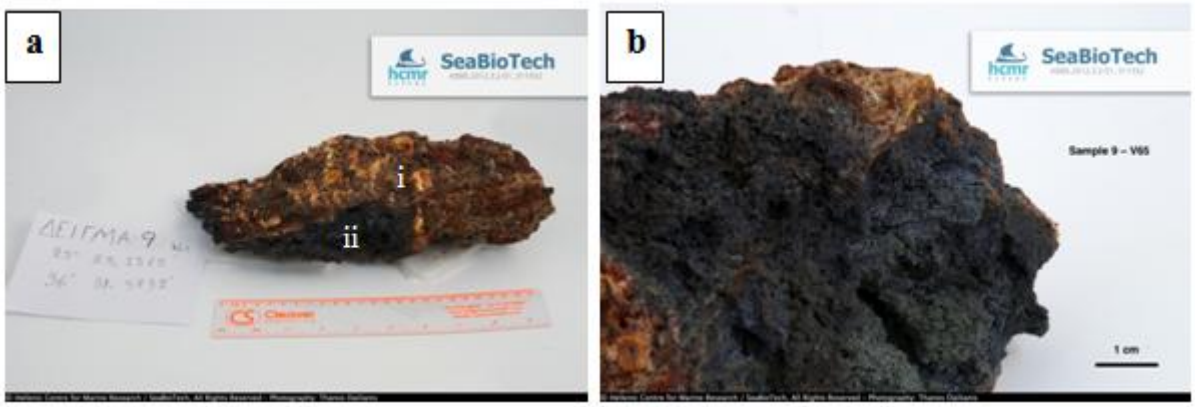

Figure 19: Ex-situ photographs of the hydrothermal spire sample No. SB-9 showing (a) the whole sample which is covered by the OAsL zone (i) while its interior represents the ISSC zone (ii); (b) its massive sulfide (ISSC)-dominated basal part of spire.

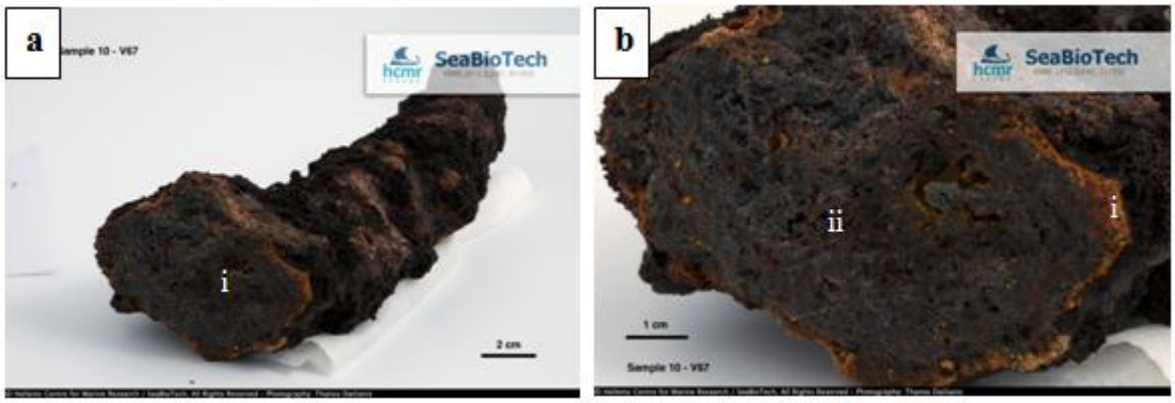

Figure 20: Ex-situ photographs of the hydrothermal chimney sample SB-10-A showing (a) the whole sample in which the zone ISSC (i) dominates and (b) its base with a thin orange rim of the OAsL zone (ii).

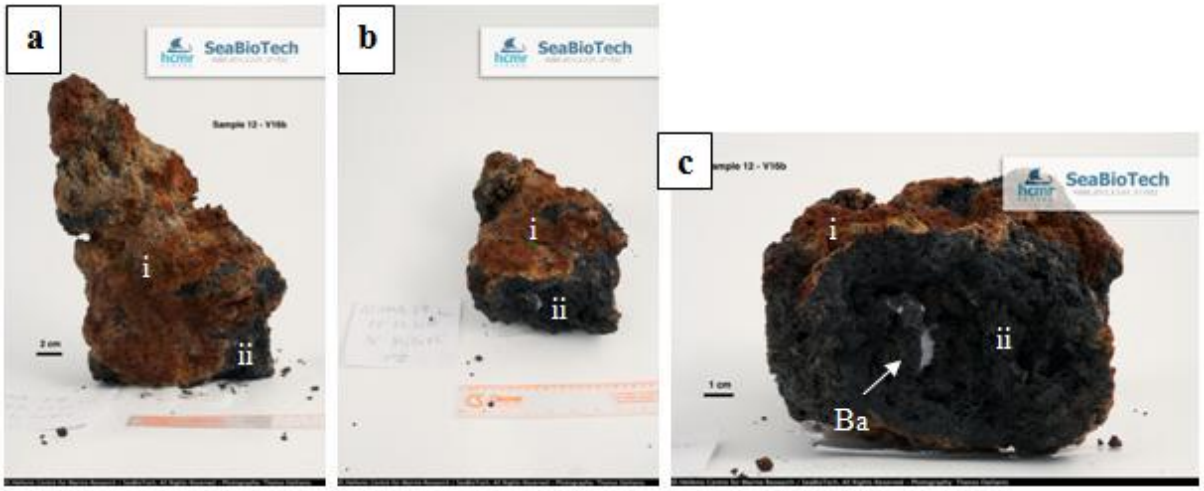

Figure 21: Ex-situ photographs of the hydrothermal chimney sample SB-12-A showing (a),(b) different aspects from the whole sample coated by the OAsL zone (i) while its interior consists of massive sulfide core (ISSC zone) (ii) and (c) its massive sulfide base (ISSC zone) (ii) with open-space filling barite crystals (Ba).

5.2 Sample preparation

Two (2) of the five (5) hydrothermal structures studied in this M.Sc. thesis (**Figs. 17–21**) were cut in several cross sections in order to obtain representative parts of the various zones, i.e., ISSC, OAsL etc. Specifically, the sample SB-3 (**Fig. 17**) was divided in six (6) subsamples (SB-3-A, SB-3-B, SB-3-C, SB-3-D, SB-3-E, SB-3-F) and the sample SB-9 (**Fig. 19**) in three (3) subsamples (SB-9-A, SB-9-B, SB-9-C). The remaining two samples (SB-7-A, SB-10-A and SB-12-A) were studied intact (**Table 2**). All the aforementioned samples encapsulate both the ISSC and the surrounding OAsL zone.

Ten (10) polished thin sections and seven (7) polished blocks were prepared from the aforementioned samples for mineralogical characterization under transmitted and reflected light (**Table 2**). Unfortunately, the samples were extremely brittle making impossible to obtain sections or blocks of the yellow-orange rims of the OAsL zone, so in this study only the ISSC zone was examined.

In an effort to examine the outer OAsL zone of the samples or to verify some ESEM results, ten (10) PXRD analyses were conducted in four (4) samples (**Table 2**). A very small amount of rock powder was obtained by scrapping the sectioned sample left from the thin section preparation in order to perform the PXRD analysis.

5.3 Analytical methods

The present M.Sc. thesis is based on mineralogical analysis using Optical Microscopy (OM) in reflected and transmitted light and Environmental Scanning Electron Microscopy (ESEM) and electron microprobe analyses (EMPA), for mineral identification, textural description and major, minor and trace element/metal analysis. Some analyses were performed using Powder X-Ray Diffraction (PXDRD) and Raman Spectroscopy (RS) for mineral identification.

Optical microscopy & Environmental scanning electron microscopy

All the prepared polished thin sections and blocks were made in the labs of Institute of Geology and Mineral Exploration (I.G.M.E.), Attiki, Greece. The optical microscope used is

housed in the Department of Geology and Geoenvironment at the National and Kapodistrian University of Athens (N.K.U.A.).

The environmental scanning electron microscopy was used to assist with mineral identification in cases when such identification was uncertain by petrographic techniques. Environmental scanning electron microscopy (ESEM) coupled with energy dispersive spectrometer (EDS), and a wavelength dispersive spectrometer (WDS) investigation of gold-coated polished surfaces was performed using an ESEM Field Emission Gun (FEI) QUANTA FEG 650 (Oxford Instruments, UK). For the EDS analyses an Oxford T-Max 80 detector was used, while for WDS analyses an Oxford Wave Instrument was used. Element mapping and peak analyses were performed using Aztec software, and WDS data processing was done using INCA Suite 4.11 software. The ESEM was housed in the Department of Geological Sciences at Stockholm University, Sweden. Calibration of the beam current was performed daily using a cobalt standard manufactured by Oxford. The standards for each element were included in the software, so the instrument was calibrated automatically to the standard during the EDS procedure. The Hg-standard for WDS was a sphalerite also manufactured by Oxford, but it was imported manually in the instrument. The detection limits for EDS is 0.1% and for WDS 0.01%.

Powder X-Ray Diffraction

A few supplementary PXRD analyses were conducted to verify the ESEM results by identifying the atomic and molecular crystal structure. The PXRD method performed by using a PANalytical X'pert PRO automated diffractometer, located at the Swedish Museum of Natural History in Stockholm. The estimated detection limit for phase identification is 1–3 wt %.

Raman spectroscopy

In order to verify and define some ESEM results, four (4) supplementary Raman spectroscopy analyses were conducted.

Raman spectra were recorded at the Department of Geological Sciences, Stockholm University, using a laser Raman confocal spectrometer (Horiba instrument LabRAM HR 800) and equipped with a multichannel air cooled CCD detector. An Ar-ion laser (λ = 514 nm) was used as the excitation source with an output power at the sample of 8 mW. The instrument was integrated with an Olympus microscope and the laser beam was focused to a spot of 1 μm

with a 100x objective. The spectral resolution is about 0.3 cm^{-1}. The instrument was calibrated using a neon lamp and the Raman line (520.7 cm^{-1}) of a silicon wafer. Instrument control and data acquisition was made with LabSpec 5 software.

Table 2: List of samples used for mineralogical study in this M.Sc. thesis.

Vent	Sample	Polished Thin Sections	Polished Blocks*	Number of PXRD analyses	Number of Raman analyses
V59(2)	SB-3-A	-	SB-3-A1	-	-
			SB-3-A2	-	-
	SB-3-B	-	SB-3-B	-	-
	SB-3-C	-	SB-3-C	-	-
	SB-3-D	SB-3-D1	-	-	2
		SB-3-D2	-	5	-
	SB-3-E	SB-3-E1	-	-	2
		SB-3-E2	-	-	-
	SB-3-F	SB-3-F	-	1	-
V08	SB-7-A	SB-7-A1	-	-	-
		SB-7-A2	-	2	-
		-	SB-7-3A	-	-
V65	SB-9-A	-	SB-9-A	-	-
	SB-9-B	-	SB-9-B	-	-
	SB-9-C	SB-9-C	-	-	-
V67	SB-10-A	SB-10-A	-	3	-
V16(b)	SB-12-A	SB-12-A	-	-	-

*The mineralogical study of polished blocks was made only by using the optical microscope, because during the ESEM procedure their gold-coated surface was charging, making their analysis by the electron microscope impossible.

6. Results

The mineral identification and textural description and interpretation were conducted on both polished thin sections and polished blocks first by Optical Microscopy and secondly confirmed by Environmental Scanning Electron Microscopy (ESEM).

In the case of Environmental Scanning Electron Microscopy (ESEM) analysis, only the polished thin sections could be examined by energy dispersive spectrometry (EDS) and wavelength dispersive spectrometry (WDS), because the gold-coated surface of the polished blocks was charging during the procedure, making their analysis impossible.

The studied hydrothermal spires are typically layered **(Figs. 17-21)**, comprising an inner sulfide sulfate zone consisting of PXRD-crystalline barite together with galena, sphalerite and pyrite/marcasite, and rare opal (‘ISSC’ of Kilias et al. 2013), an intermediate ‘‘outer As-sulfide layer’’ dominated by PXRD-amorphous disseminated As-rich sulfides (OAsL of Kilias et al. 2013) and an outer zone of gelatinous orange to brown Fe-rich microbial mat designated as ‘‘surface Fe-rich crust’’ (SFeC) **(Kilias et al. 2013)**. The studied sphalerite belongs only to the “inner sulfide-sulfate core” (ISSC).

6.1. Mineralogy and sphalerite textures of the ‘Inner Sulfide-Sulfate Core’ (ISSC)

Optical Microscopy in reflected and transmitted light, and Environmental Electron Scanning Microscopy (ESEM) aided by PXRD and Raman Spectroscopy analysis revealed three main sulfide phases within a barite matrix, and rare opal: pyrite/marcasite, sphalerite, galena; rare stibnite (Sb_2S_3), unidentified Sb-Pb-sulfosalts and a sphalerite-like phase containing Zn, S, Fe and Sb (**Table 3)**, were also detected.

Barite ($BaSO_4$) occurs as blades, acicular clusters, fibrous crystals and rarely as dendritic crystals and it usually forms the matrix of disseminated sulfides, sphalerite and mainly colloform pyrite/marcasite **(Fig. 22a, b, c)**. Moreover, barite blades are found with As-sulfide overgrowths along their edges **(Fig. 22d)**.

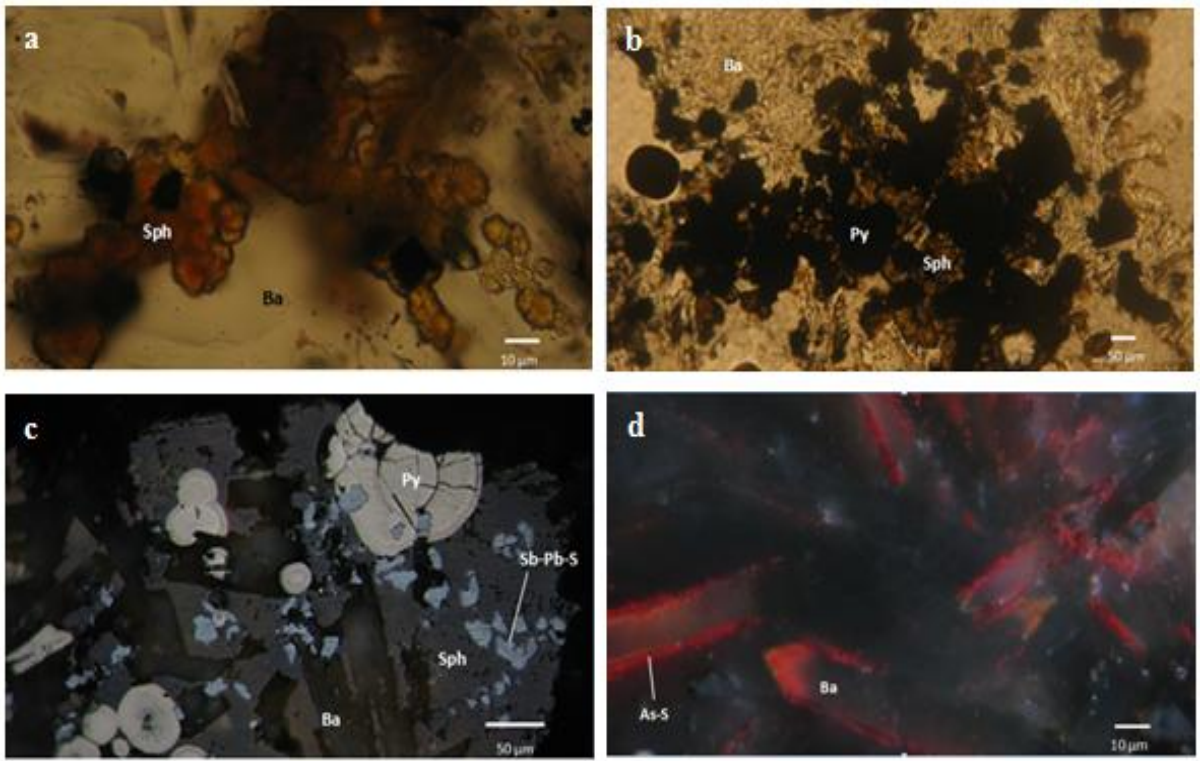

Figure 22: Photomicrographs of commonly seen textures in the inner sulfide-sulfate core (ISSC). Transmitted light microphotograph (TLP) of (a) barite (Ba) laths and rosettes forming the substrate for disseminated colloform zoned sphalerite (Sph) (oil lens and // Nichols). (b) pyrite/marcasite (Py) microglobules and colloform zoned sphalerite (Sph) overlaying barite (Ba) matrix (oil lens and // Nichols). (c) Reflected light microphotograph (RLP) of anhedral Sb-Pb-sulfosalt inclusions in concentrically laminated pyrite/marcasite (Py), mantled by barite laths (Ba) and anhedral sphalerite (Sph) with scattered Sb-Pb-sulfosalts inclusions (oil lens and // Nichols). (d) Reflected light microphotograph (RLP) of As-sulfides (As-S) overgrowing barite (Ba) blades along their edges (oil lens and crossed Nichols).

Pyrite/marcasite occurs in many textures such as compact, concentrically laminated spheroids **(Fig. 23a, b)** intricate closely-packed aggregates of rounded and bulbous laminated pyrite/marcasite displaying microstromatolitic structures **(Fig. 23c)**, as radial rim encircling concentrically banded, radial, spheroidal masses of pyrite/marcasite **(Fig. 23d)**. Additionally, pyrite/marcasite is found as anhedral porous, spongy rims around concentrically laminated pyrite/marcasite; the thickness of these rims is around 25-50 μm **(Fig. 23e)**.

Galena (PbS) occurs anhedral, up to 10μm across **(Fig. 24a, d)**, as rims encircling concentrically laminated spheroids of pyrite/marcasite **(Fig. 24b)** or as inclusions in sphalerite grains **(Fig. 24c)**.

Rare stibnite (Sb_2S_3) is found a) as fibers in open space **(Fig. 25a, b, c)** or b) in the form of anhedral or subhedral grains in open space **(Fig. 25c)**.

Anhedral Sb-Pb-sulfosalts **(Figs. 22c, 23a, b, 24)** are found as inclusions into colloform banded pyrite/marcasite, colloform sphalerite or as rims encircling concentrically laminated spheroids of pyrite/marcasite.

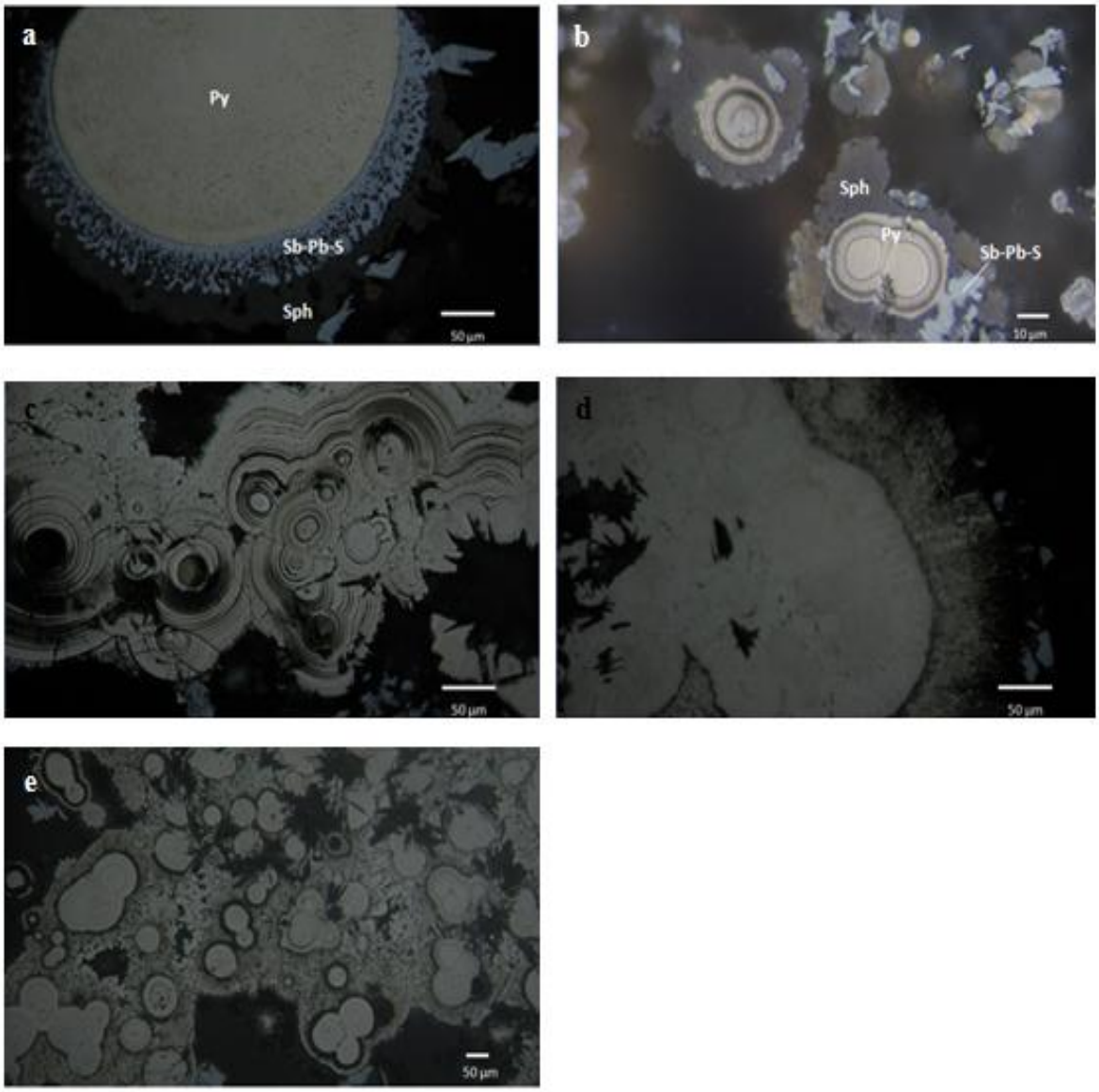

Figure 23: Photomicrographs of commonly seen textures in the inner sulfide-sulfate core (ISSC). Reflected light microphotograph (RLP) of (a) finely concentrically laminated spheroids of pyrite/marcasite (Py) mantled by anhedral to subhedral intergrowths of Sb-Pb-sulfosalts and sphalerite (Sph) (oil lens and // Nichols). (b) Concentrically laminated spheres of pyrite/marcasite (Py) surrounded by sphalerite (Sph) with inclusions of Sb-Pb-sulfosalts (oil lens and // Nichols). (c) Finely laminated pyrite-marcasite fabric with (micro)stromatolitic morphology (oil lens and // Nichols). (d) Radial rim of pyrite/marcasite encircling concentrically banded, radial, spheroidal masses of pyrite/marcasite (oil lens and // Nichols). (e) Anhedral porous, pyrite/marcasite spongy rims around concentrically laminated pyrite/marcasite (oil lens and // Nichols).

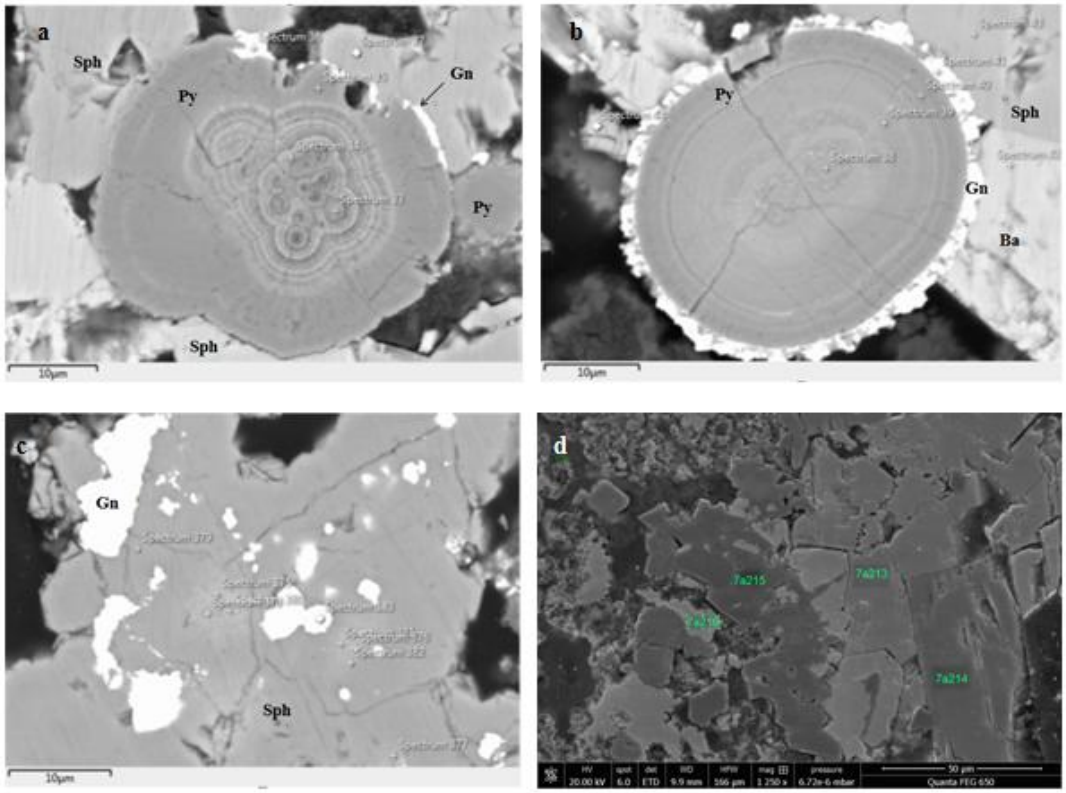

Figure 24: ESEM photographs of (a) anhedral galena (Gn) with anhedral sphalerite (Sph) and intricate closely packed, colloform banded pyrite/marcasite (Py) fabric. (b) Galena rim (Gn) encircling concentrically laminated spheroid of pyrite/marcasite (Py). (c) Anhedral inclusions of galena (Gn) into anhedral sphalerite (Sph). (d) ESEM backscatter image showing anhedral galena (points 7a213 and 7a216), with spherical pyrite (point 7a215) and barite blades (point 7a214).

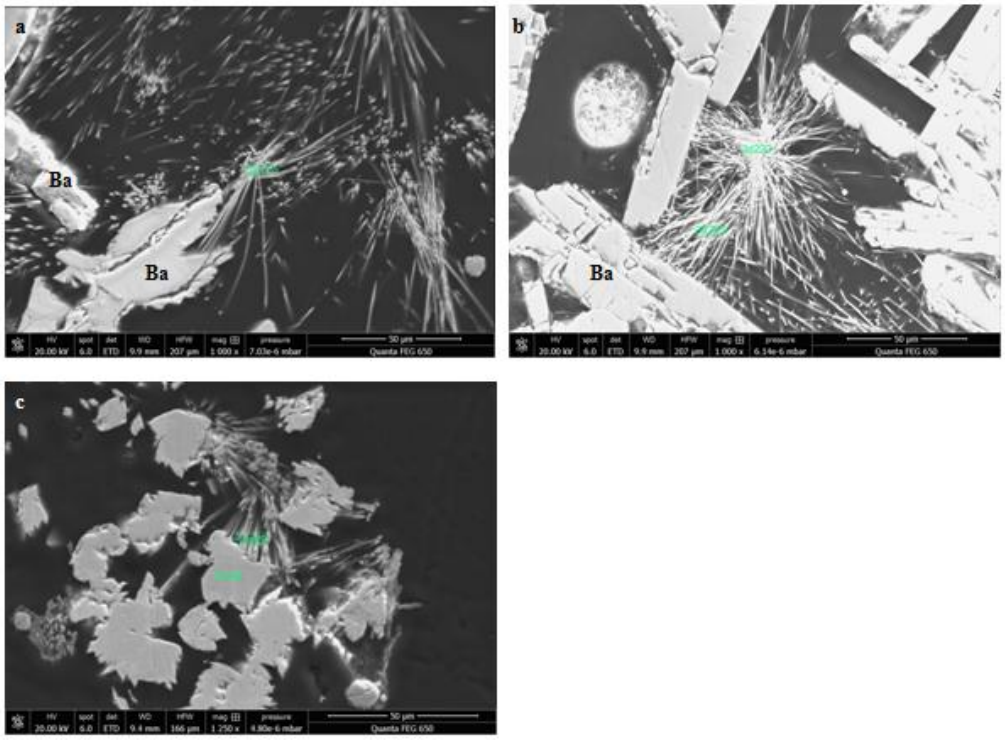

Figure 25: ESEM backscatter images of (a), (b) stibnite fibers (noted green points) with barite blades (Ba). (c) anhedral to subhedral and fibrous stibnite in open space.

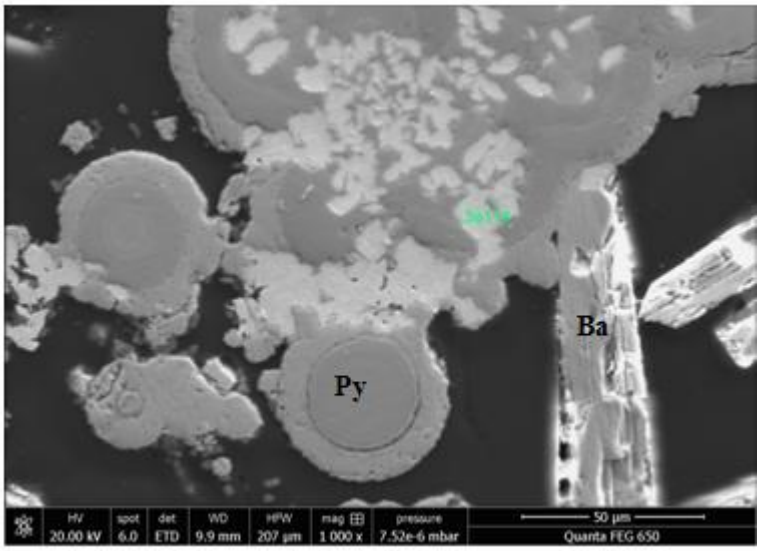

Figure 26: ESEM backscatter image showing anhedral Sb-Pb-sulfosalts inclusions (marked green) into laminated concentric spheres of pyrite/marcasite.

An unidentified non-stoichiometric Zn-sulfide phase was found in a texture of parallel bundles **(Fig. 27)**. This phase consists of zinc (Zn), sulfur (S), iron (Fe) and antimony (Sb) in average concentrations of 87.49, 10.29, 1.24 and 0.98 wt %, respectively (**Table 3).**

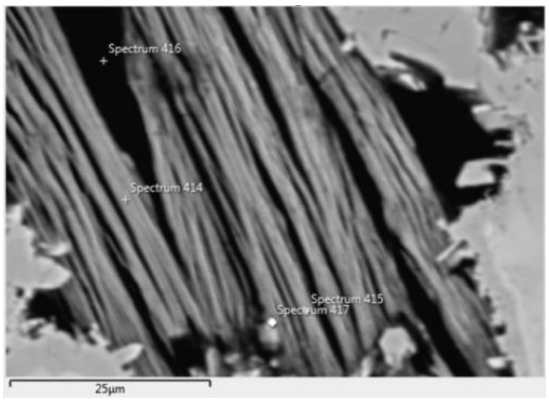

Figure 27: ESEM photograph of biomorphous bundles of unidentified non-stoichiometric Zn-sulfide phase.

Table 3: Single EPMA analyses showing the concentrations (wt %) of the elements contained in the non-stoichiometric Zn- sulfide phase. Spots of EPMA analyses are represented by crosses accompanied by "Spectrum +number X" designation (Fig. 27).

Spectrum	S (wt %)	Zn (wt %)	Fe (wt %)	Sb (wt %)
414	9.88	86.77	1.14	0.56
415	10.69	88.21	1.35	1.41

Sphalerite in the ISSC displays complex textures which can be classified into three (3) varieties designated as Type 1 to Type 3:

- Type 1: Microglobular and colloform zoned sphalerite
- Type 2: Zoned sphalerite with porous core and massive rim
- Type 3: Inclusion-rich and compositionally zoned massive sphalerite

6.1.1. Type 1: Microglobular and colloform zoned sphalerite

6.1.1.1 Mineralogical and textural description of sphalerite type 1

During the ESEM-EDS analysis of samples SB-9-C and SB-12-A, microglobular sphalerite was defined. The second form of this sphalerite type occurs as independent microglobules within massive sphalerite or in open space (**Fig. 28, 29**).

Raman analyses were conducted in the dark red and yellow zones of sphalerite type 1, as shown in **Figure 30**. Compared with Raman spectra of (a) pure sphalerite **(http://rruff.info)**, (b) Cd-rich sphalerite **(Kharbish 2007)** and (c) sphalerite containing Fe **(http://rruff.info)**, the spectra from the dark red areas of the microglobular and colloform zoned sphalerite match with the Cd-rich sphalerite, while the yellow areas match with the Fe-rich sphalerite.

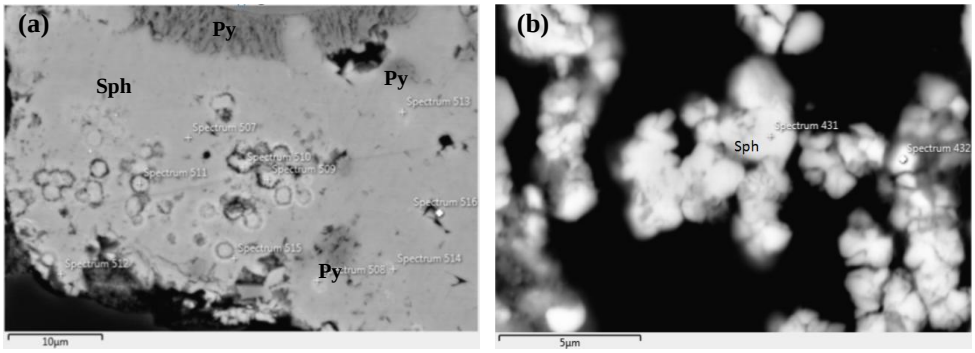

Figure 28: ESEM photograph of (a) massive sphalerite (Sph) with voids (dark) containing numerous circular to ovoid microglobules (~2 μm) (Type 1); microglobules' cores are separated from their rims by a thin gap (b) sphalerite (Sph) colloform microglobules (Type 1).

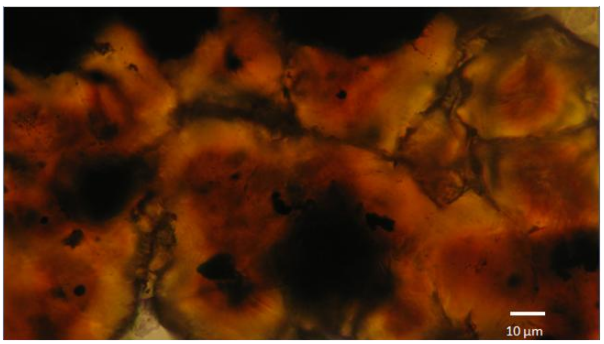

Figure 29: Transmitted light microphotograph (TLP) of colloform zoned sphalerite (Type 1) (oil lens and //Nichols).

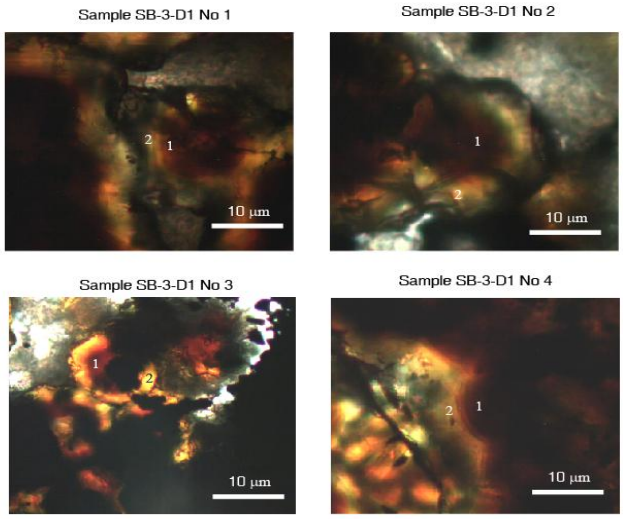
Sample SB-3-D1 No 1
Sample SB-3-D1 No 2
Sample SB-3-D1 No 3
Sample SB-3-D1 No 4
10 μm

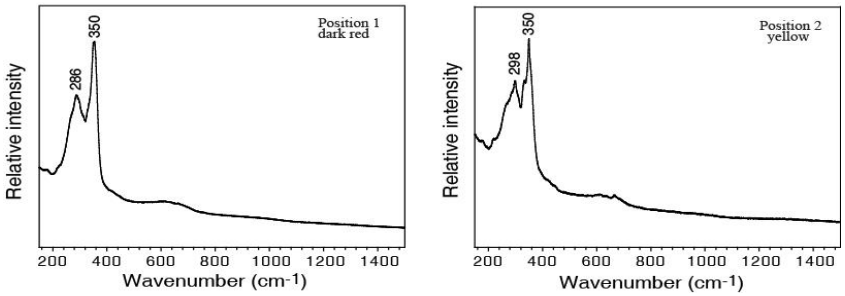
Position 1
dark red
Position 2
yellow
Relative intensity
286
298
350
200 400 600 800 1000 1200 1400
Wavenumber (cm-1)

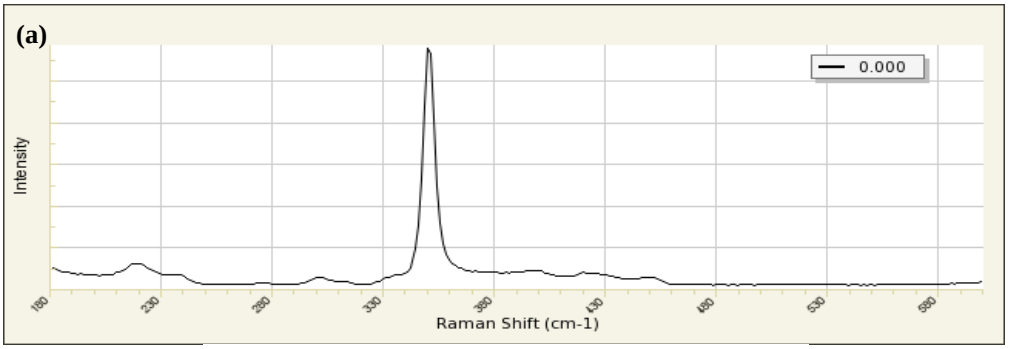
(a)
0.000
Intensity
Raman Shift (cm-1)

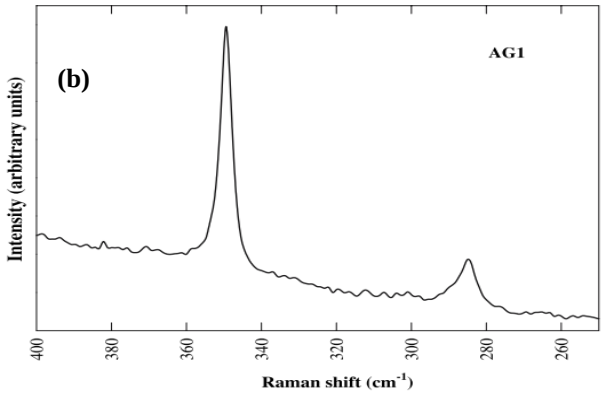
(b)
AG1
Intensity (arbitrary units)
400 380 360 340 320 300 280 260
Raman shift (cm-1)

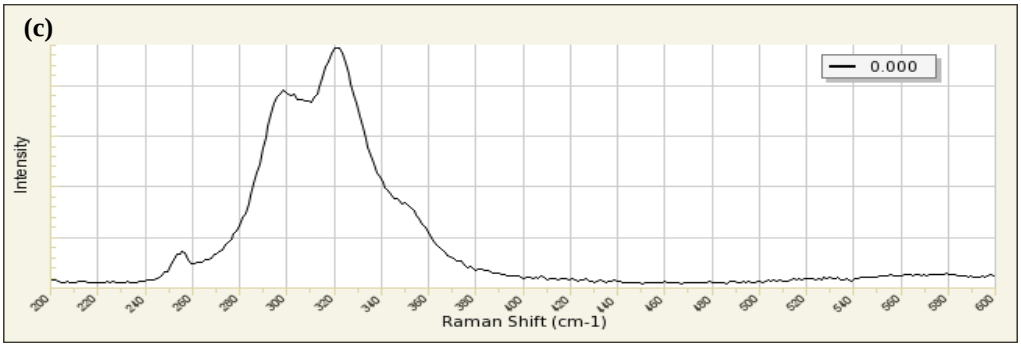

Figure 30: Raman analyses of the dark red (1) and yellow zones (2) of microglobular and colloform zoned sphalerite, compared with Raman spectra of (a) pure sphalerite (http://rruff.info), (b) Cd-rich sphalerite (Kharbish 2007) and (c) sphalerite containing Fe (http://rruff.info).

6.1.2.2. Quantitative EPMA analysis, compositional mapping, element distribution and correlation trends of sphalerite type 1

The absolute concentrations, normalized to 100%, for Fe and Sb in type 1 sphalerite are summarized as histograms in **Figures 31** and **32.** Whereas more trace elements (Cu, Cd, As and Ag) were also detected during electron microprobe (EPMA) analyses, their quantity was not enough to be displayed in histograms.

A total of 12 EPMA analyses were carried out on sphalerite type 1. Concentrations of eight elements (S, Zn, Fe, Cu, Cd, Sb, As and Ag) were determined using EDS mode. Electron probe microanalyses (EPMA-EDS) of samples SB-9-C and SB-12-A for major, minor and trace elements with number of analyses (n), means, standard deviations (1σ SD), maxima, minima and limits of detection (LOD) are listed in **Table 4**. Complete EPMA datasets can be found in the Appendix.

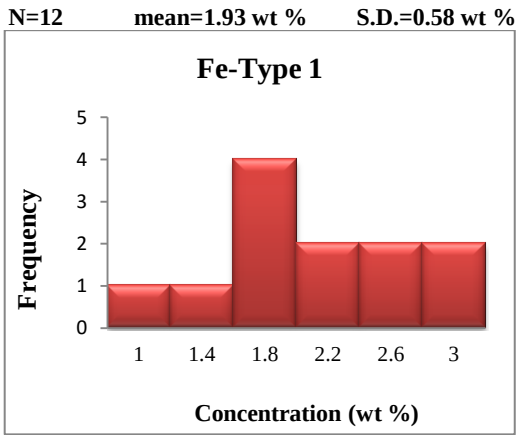

Figure 31: Histogram showing the variation in Fe in sphalerite type 1 from Kolumbo hydrothermal precipitates.

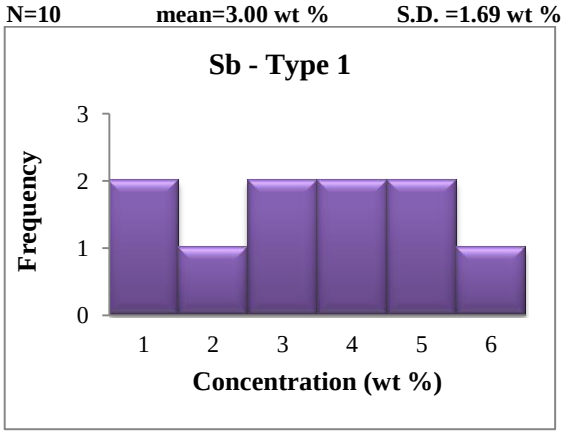

Figure 32: Histogram showing the variation in Sb in sphalerite type 1 from Kolumbo hydrothermal precipitates

Table 4: EPMA main results from the microglobular and colloform zoned sphalerite (type 1). Minimum, maximum, mean, corresponding standard deviation (1σ SD), and limit of detection (LOD) are presented.

Type 1	S (wt %)	Fe (wt %)	Zn (wt %)	Sb (wt %)	Cu (wt %)	Cd (wt %)	As (wt %)	Ag (wt %)
n^	12	12	12	10	4	3	3	3
Min.	32.42	0.99	56.86	0.706	0.850	0.973	0.218	1.103
Max.	35.45	2.94	64.40	5.757	1.024	1.025	0.779	1.647
Mean	34.05	1.92	60.49	3.004	0.949	0.999	0.433	1.429
1σ SD	1.04	0.58	2.77	1.692	0.076	0.026	0.303	0.287
LOD	0.1	0.1	0.1	0.1	0.1	0.1	0.1	0.1

^ **n**: number of measurements with higher contents than the limit of detection.

For sphalerite type 1 the Zn content ranges from 56.86 to 64.40 wt % and averages 60.49 wt % **(Table 4)**. The Fe content ranges from 0.99 to 2.94 wt % and averages 1.92 wt %. Sphalerite also shows significant variation in the content of Sb (0.71 to 5.76 wt %), Cu (up to 1.02 wt %), As (up to 0.78 wt %) and Cd (up to 1.02 wt %).

In order to examine potential chemical variations within the type 1 of sphalerite, trace element mapping was carried out by ESEM-EDS (**Fig. 33).** This procedure reveals a concentric rhythmic zoning from the sphalerite core towards their rim. The core seems to be enriched in Hg and Cd; a Sb-rich band succeeds and finally another concentric rhythmic zone of Hg and Cd followed by a Sb-Cu-rich zone ends up to the trace element-depleted rim.

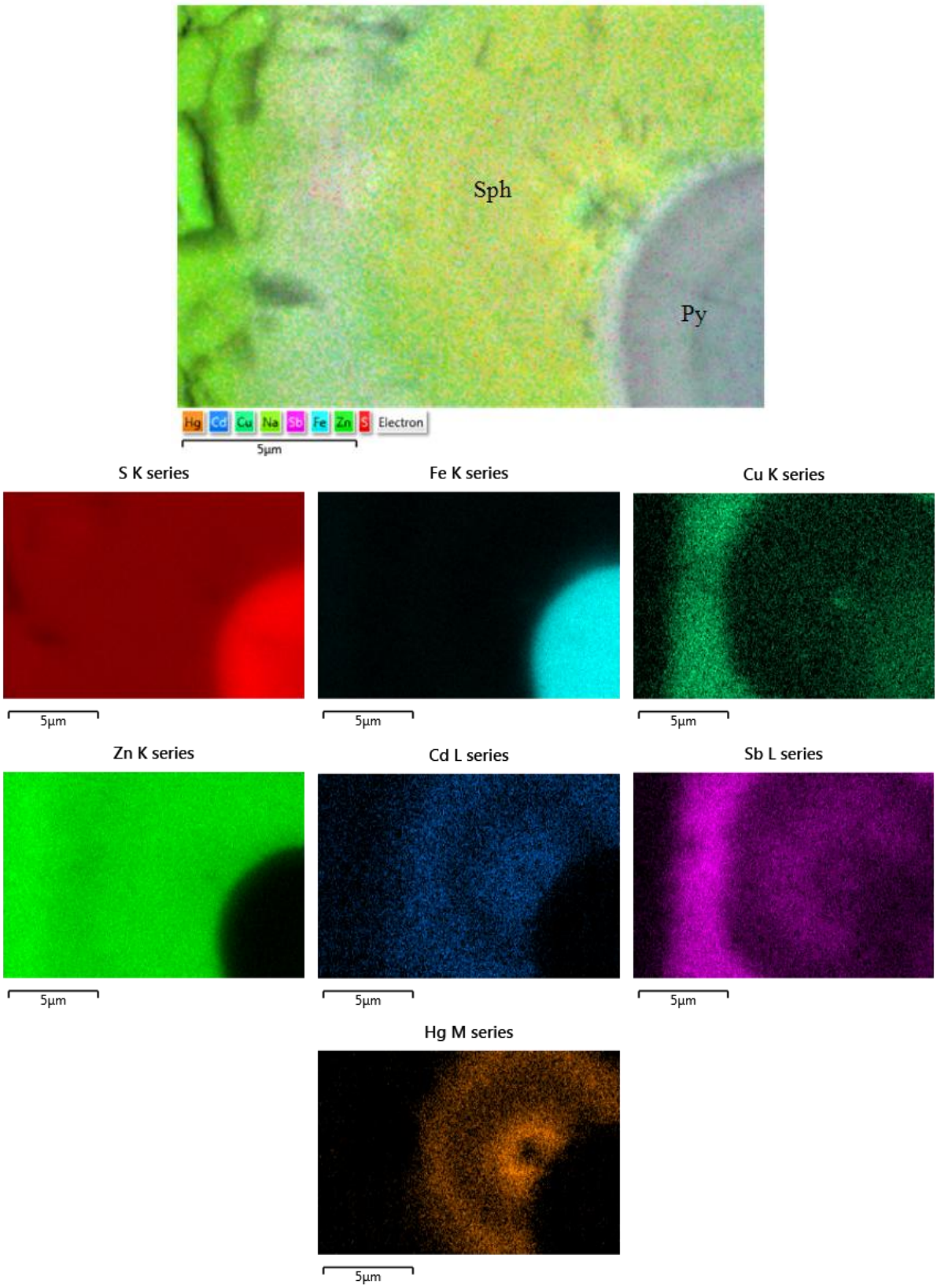

Figure 33: Energy dispersive spectroscopy map of colloform zoned sphalerite (Sph) of type 1 for Hg, Cd, Sb, Fe, S, Cu, Zn, proving a rhythmic zonation.

In **Figure 34** the correlation between Zn and the other detected trace elements (Fe, Sb, Cu, Cd, As and Ag) in sphalerite type 1 is illustrated. Whereas there is a good correlation

between Zn and Fe **(Fig. 34a)** and Zn and Sb **(Fig. 34b)**, it is not possible to come to any conclusion for the correlation of Zn with Cu, Cd, As and Ag **(Figs. 34 c, d, e, f)** because of the scarcity of analyses number for the aforementioned trace metals.

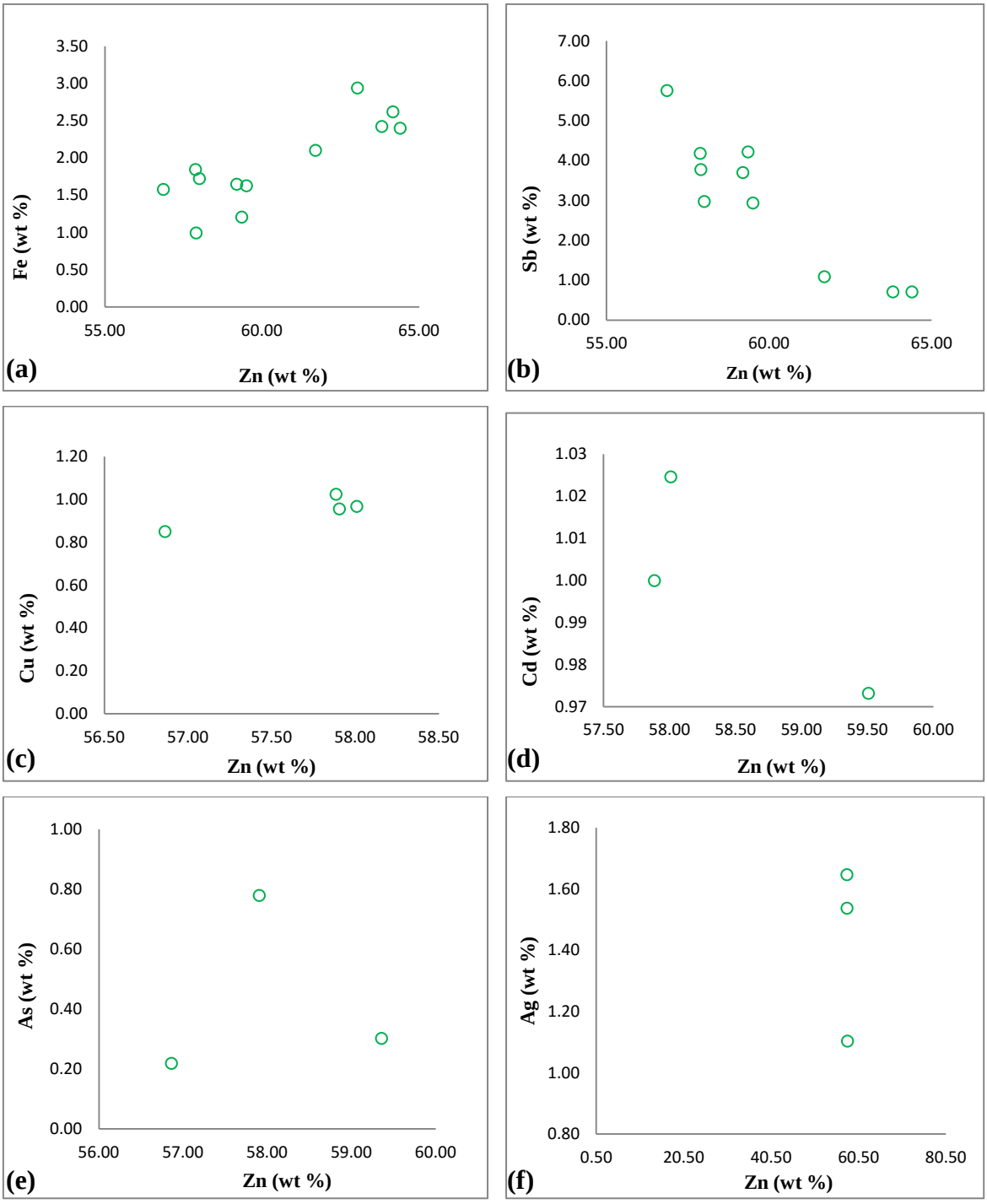

Figure 34: Binary correlation plots of (a) Zn vs. Fe, (b) Zn vs. Sb, (c) Zn vs. Cu, (d) Zn vs. Cd, (e) Zn vs. As, (f) Zn vs. Ag, in microglobular and colloform zoned sphalerite (Type 1).

6.1.2. Type 2: Zoned sphalerite with porous core and massive rim

6.1.2.1 Mineralogical and textural description of sphalerite type 2

Sphalerite of type 3 are characterized by texturally and/or chemically zoned anhedral sphalerite having porous core and massive rim of variable thickness, associated with barite, pyrite/marcasite, galena and opal **(Figs. 35, 36, 37, 38, 39)**. Commonly, porous core is devoid of optically detectable galena, whereas anhedral galena inclusions of various sizes and shapes occur either randomly distributed within the massive rims **(Fig. 35, 36)** or they outline the interface between porous and massive zones of sphalerite 2 (**Figs. 37, 38)**.

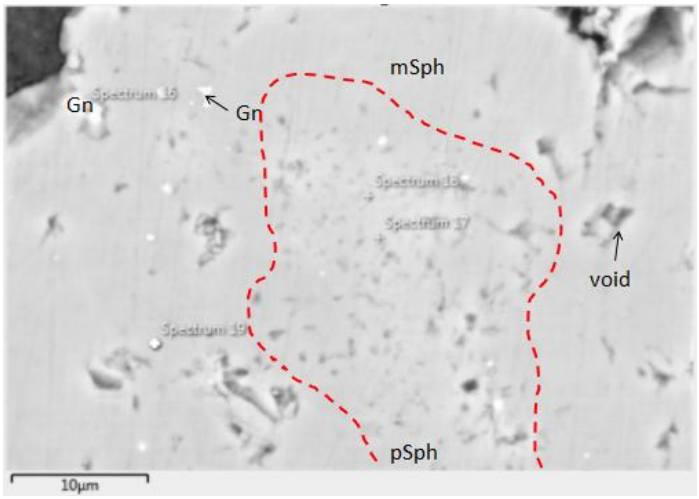

Figure 35: ESEM photograph of type 2 sphalerite with porous core (pSph) and massive rim (mSph) with voids (dark). The latter contains randomly distributed galena (Gn) inclusions.

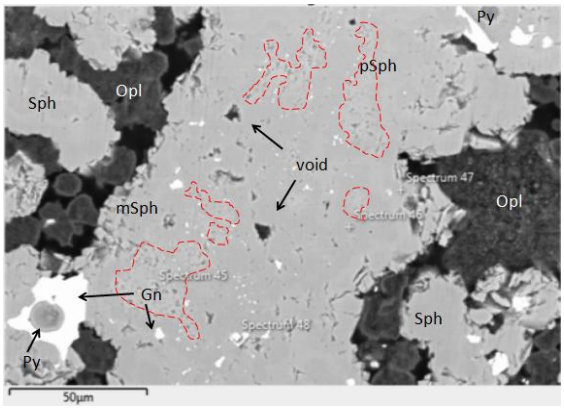

Figure 36: ESEM photograph showing the association between sphalerite type 2 and pyrite (Py), galena (Gn) and opal (Opl).

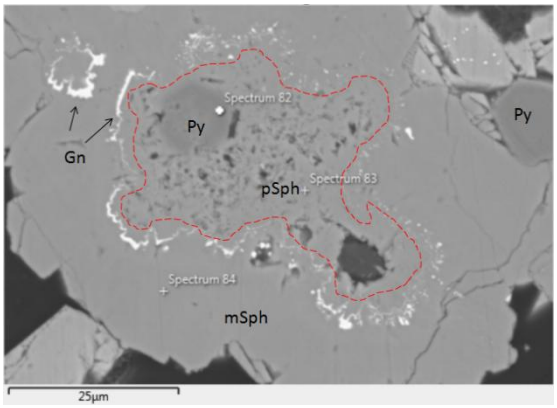

Figure 37: BSE-ESEM photograph of type 2 sphalerite exhibiting textural and chemical zoning, consisting of sphalerite with porous core (pSph) which contains pyrite (Py) microglobules and is surrounded by massive sphalerite (mSph). Galena (Gn) inclusions appear into massive sphalerite. These inclusions mainly separate porous from massive sphalerite.

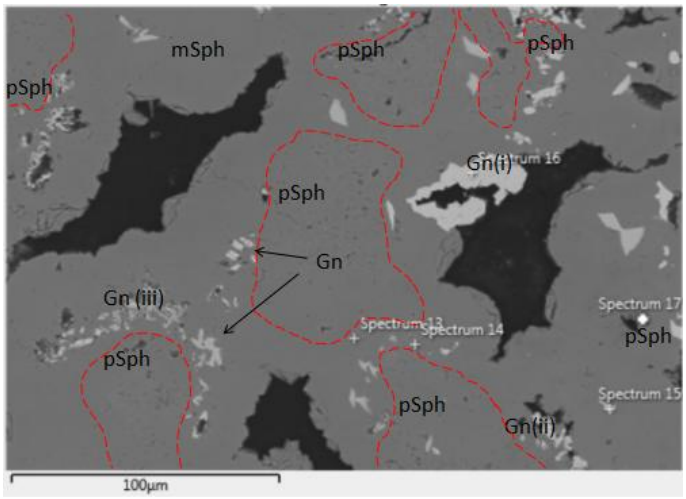

Figure 38: ESEM photograph of closely packed anhedral type 2 sphalerite consisting of porous cores (pSph) and massive rims (mSph) with voids (dark). Sphalerites contain inclusions of anhedral (i), skeletal assemblages (ii), and filaments and or needles (iii) of galena (Gn).

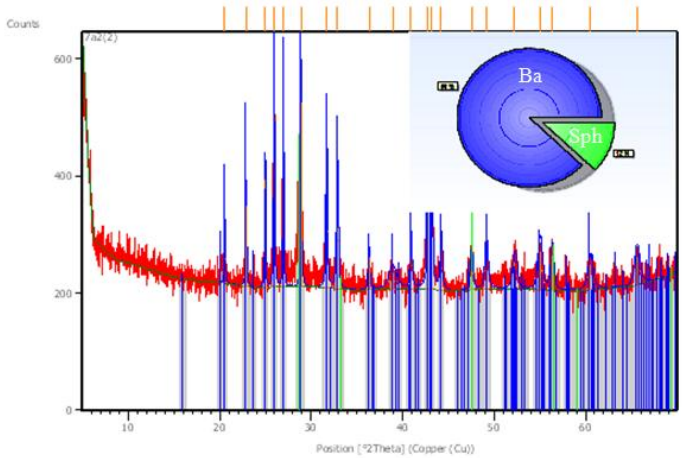

Figure 39: XRD spectra showing the association of barite and sphalerite. The pie chart shows how well the spectra for each mineral match the XRD-diagram.

6.1.2.2. Quantitative EPMA analysis, compositional mapping, element distribution and correlation trends of sphalerite type 2

The absolute concentrations, normalized to 100%, for Fe and Sb in type 2 sphalerite are summarized as histograms in **Figures 40** and **41.** Whereas more trace elements (Cu, Cd, As and Ag) were also detected during electron microprobe (EPMA) analyses, their quantity was not enough to be displayed in histograms.

A total of 28 EPMA analyses were carried out on sphalerite type 2. Concentrations of eight elements (S, Zn, Fe, Cu, Cd, Sb, As and Ag) were determined using EDS mode. Electron probe microanalyses (EPMA-EDS) of samples SB-3-D1, SB-3-E2 and SB-9-C for major, minor and trace elements with number of analyses (n), means, standard deviations (1σ SD), maxima, minima and limits of detection (LOD) are listed in **Table 5**. Complete EPMA datasets can be found in the Appendix.

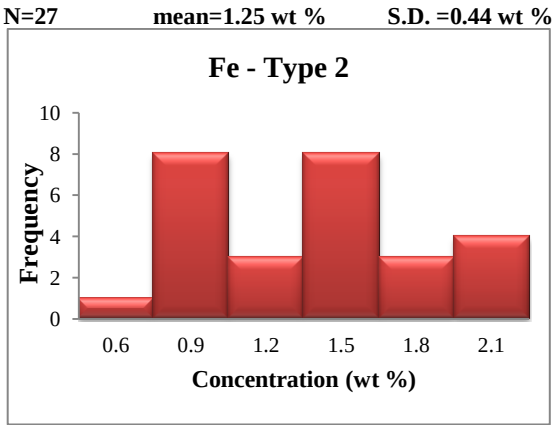

Figure 40: Histogram showing the variation of Fe in sphalerite type 2 from Kolumbo hydrothermal precipitates.

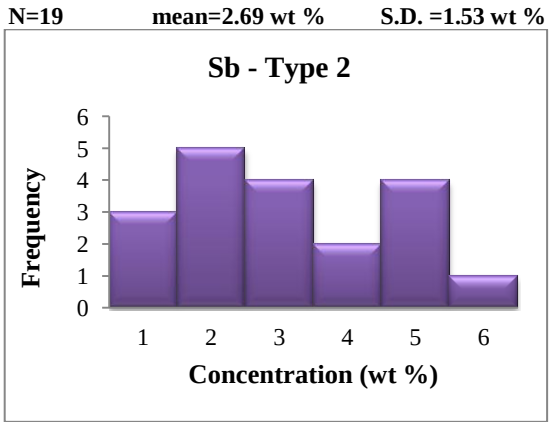

Figure 41: Histogram showing the variation of Sb in sphalerite type 2 from Kolumbo hydrothermal precipitates.

Table 5: EPMA main results for zoned sphalerite with porous core and massive rim (Type 2). Minimum, maximum, mean, corresponding standard deviation (1σ SD), and limit of detection (LOD) are presented.

Type 2		S (wt %)	Fe (wt %)	Zn (wt %)	Sb (wt %)	Cu (wt %)	Cd (wt %)	As (wt %)	Ag (wt %)
Porous core	n^	12	12	12	12	2	1	3	1
	Min.	33.80	0.54	56.63	0.98	0.58	*	0.52	**
	Max.	39.40	1.49	63.52	5.94	1.22	*	1.07	**
	Mean	34.56	1.01	60.56	3.40	0.90	*	0.76	**
	1σ SD	1.55	0.33	1.95	1.45	0.45	*	0.28	**
	LOD	0.1	0.1	0.1	0.1	0.1	0.1	0.1	0.1
Massive rim	n	16	16	16	7	3	3	-	-
	Min.	33.77	0.69	57.89	0.90	0.59	0.49	-	-
	Max.	39.85	2.02	65.37	2.79	1.67	0.81	-	-
	Mean	35.06	1.41	62.56	1.47	1.10	0.68	-	-
	1σ SD	1.82	0.45	1.95	0.65	0.54	0.17	-	-
	LOD	0.1	0.1	0.1	0.1	0.1	0.1	0.1	0.1

^ n: number of measurements with higher contents than the limit of detection.
***** One single analysis of 1.30 wt % Cd.
****** One single analysis of 1.19 wt % Ag.
- Concentrations below the detection limit.

The EPMA analyses for Kolumbo type 2 sphalerites are grouped in (i) 12 analyses from the porous core and (ii) 16 from the massive rim **(Table 5)**. Sphalerite core is composed of 56.63 to 63.52 wt % Zn (60.56±1.95 wt %) and 33.80 to 39.40 wt % S (34.56±1.55 wt %). Fe and Sb are ubiquitous components of all analyzed sphalerite 2 cores, with contents varying between 0.54 and 1.49 wt % (mean 1.01±0.33 wt %), and 0.98 to 5.94 wt % (mean 3.40±1.45 wt %), respectively; in sphalerite 2 cores Cu (up to 1.22 wt %) and As (up to 1.07 wt %) were also detected but only in a few number of analyses. Cd in 1.30 wt % and Ag in 1.19 wt % were also found just in one analysis. Sphalerite rim is composed of 57.89 to 65.37 wt % Zn (62.56±1.95 wt %) and 33.77 to 39.85 wt % (35.86±1.82 wt %) S. Fe is detected in all analyzed sphalerite 2 rims, with contents varying between 0.69 and 2.02 wt % (mean 1.41±0.45 wt %). Sb concentrations range between 0.90 and 2.79 wt % (mean 1.47±0.65 wt %) in sphalerite 2 rims whereas Cu (up to 1.67 wt %) and Cd (up to 0.81 wt %) were also detected but only in a few number of analyses. As and Ag were below the detection limit of the instrument.

In order to examine potential chemical variations between porous and massive type 2 sphalerite, systematic trace element concentration profiles were carried out by ESEM-EDS, as shown in **Figure 42**. Systematic trace metal variations between porous core and massive rim

can be observed: depletion of Sb, Ag and Cu, and enrichment of Fe and Cd towards the outer massive rim.

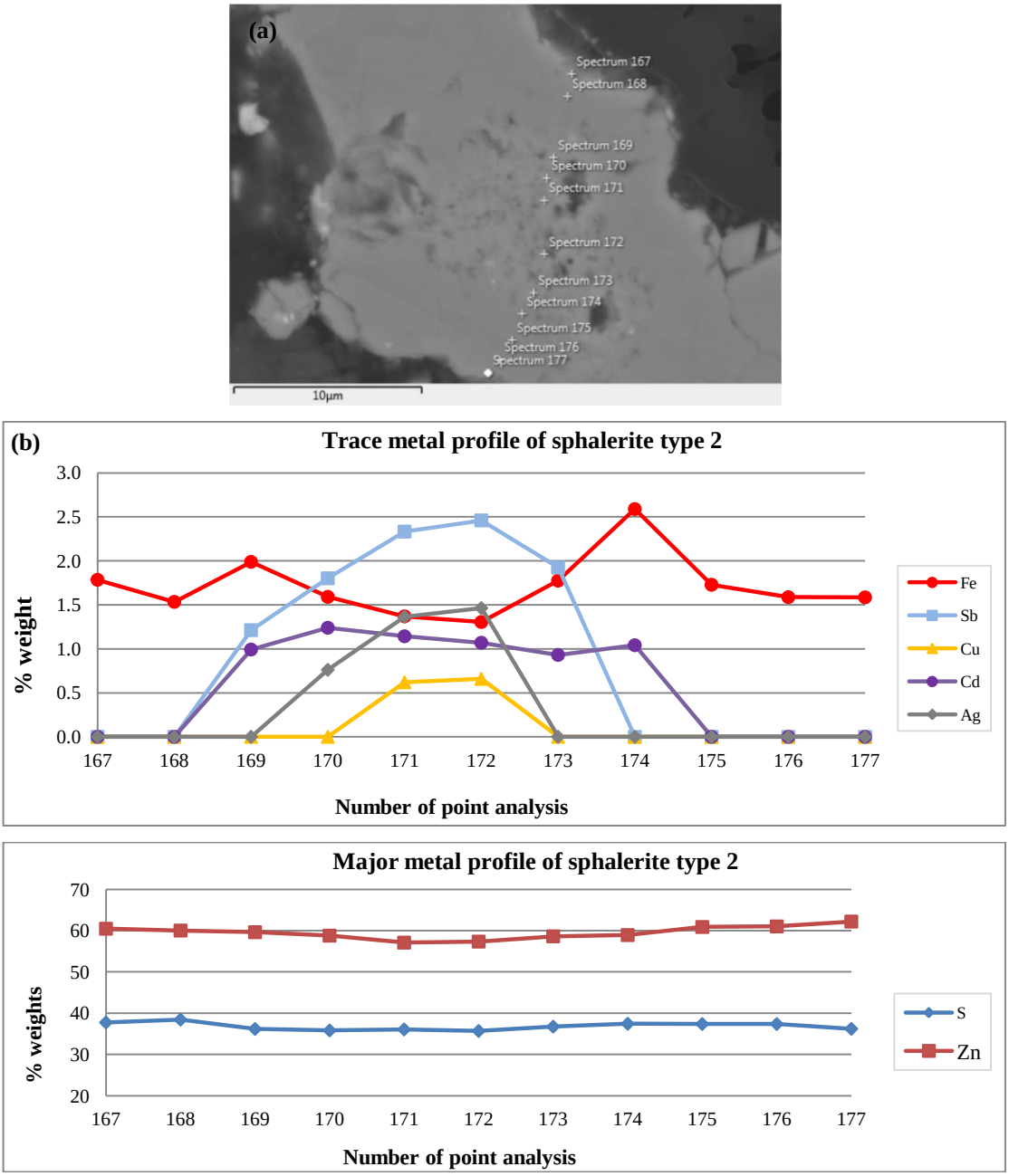

Figure 42: Geochemical profile across a zoned type 2 sphalerite crystal with porous core and massive rim. (a) Spots of EPMA analyses are represented by crosses accompanied by "Spectrum +number X" designation, including "Spectrum 170, 171, and 172" for the porous core, and all the rest "Spectrum number X" designations for the massive rim. (b) Enrichment of Ag, Sb, Cu towards the outer massive parts of the sphalerite crystal.

In **Figures 43, 44, 45, 46** and **47** the correlation between Zn and the other detected trace elements (Fe, Sb, Cu, Cd and As) in both porous and massive sphalerite of type 2 is illustrated. It is not possible to come to any conclusion for the correlation of Zn with Cu, Cd, and As **(Figs. 45, 46, 47)** because of the limited number of analyses for the aforementioned trace metals.

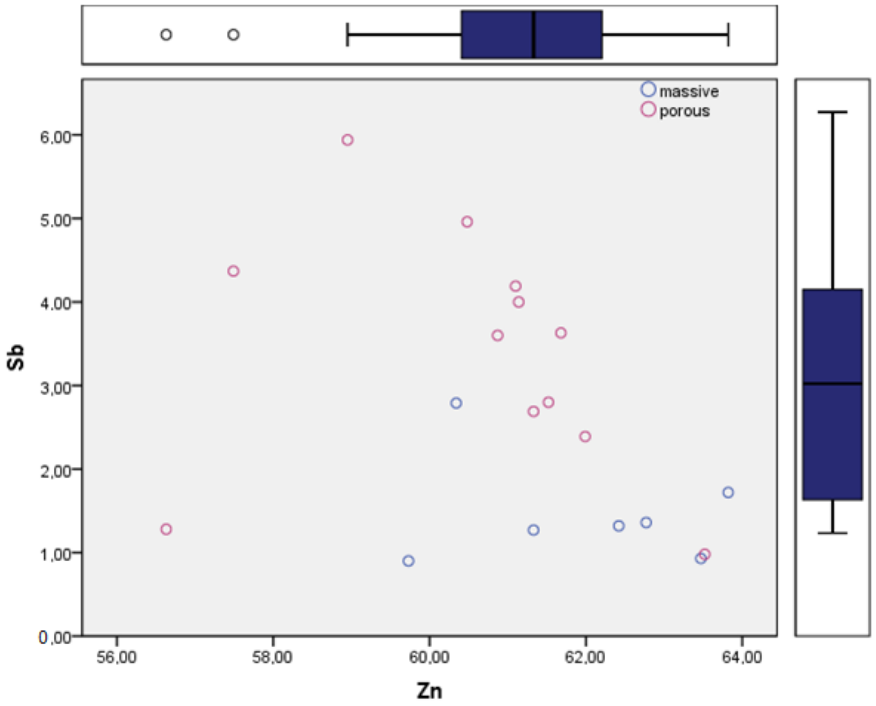

Figure 43: Binary correlation plot of Zn vs. Sb in zoned sphalerite with porous core and massive rim (Type 2).

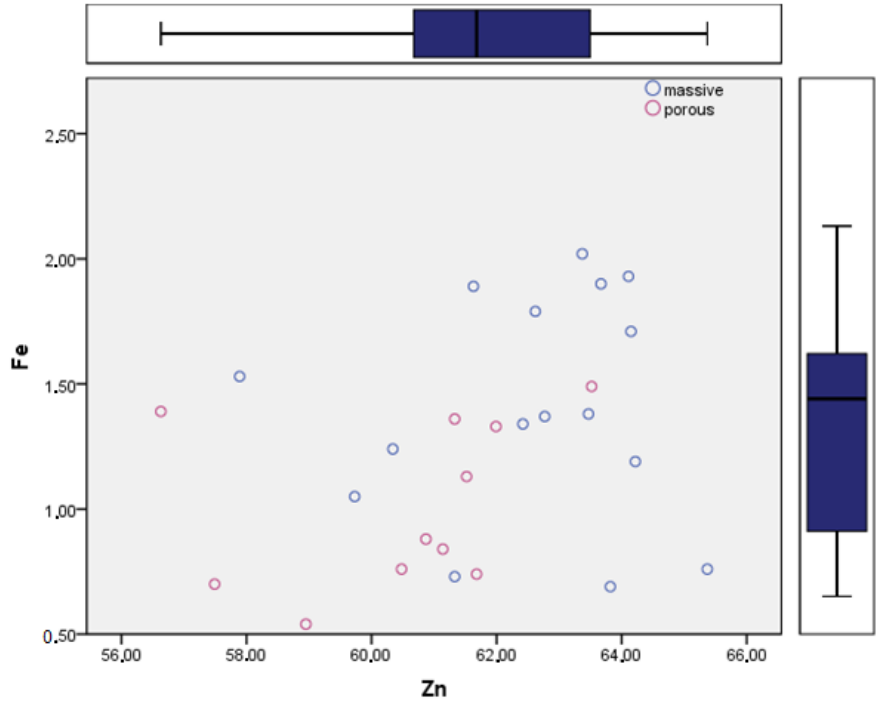

Figure 44: Binary correlation plot of Zn vs. Fe in zoned sphalerite with porous core and massive rim (Type 2).

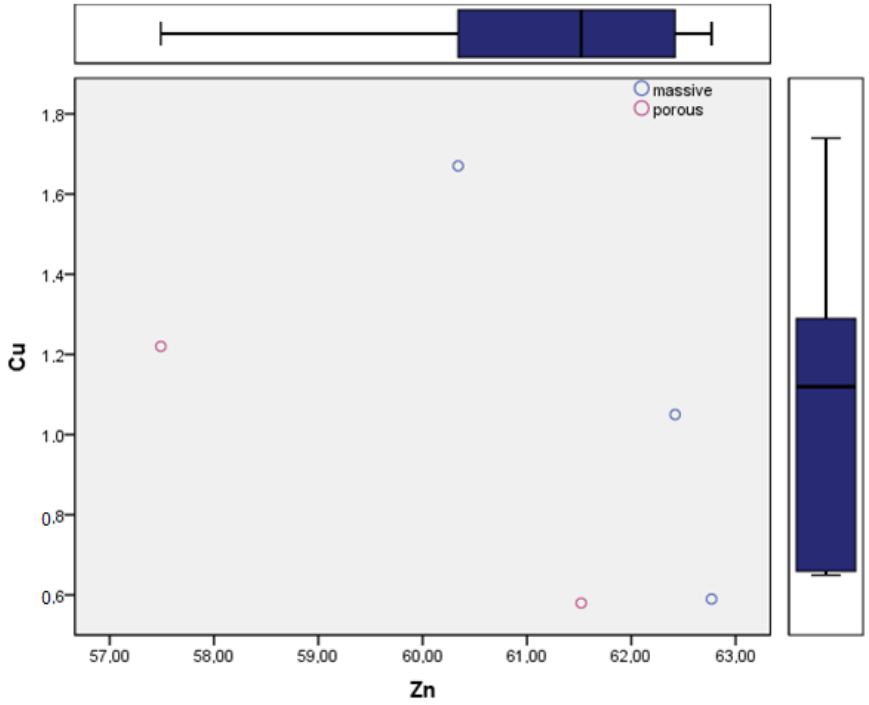

Figure 45: Binary correlation plot of Zn vs. Cu in zoned sphalerite with porous core and massive rim (Type 2).

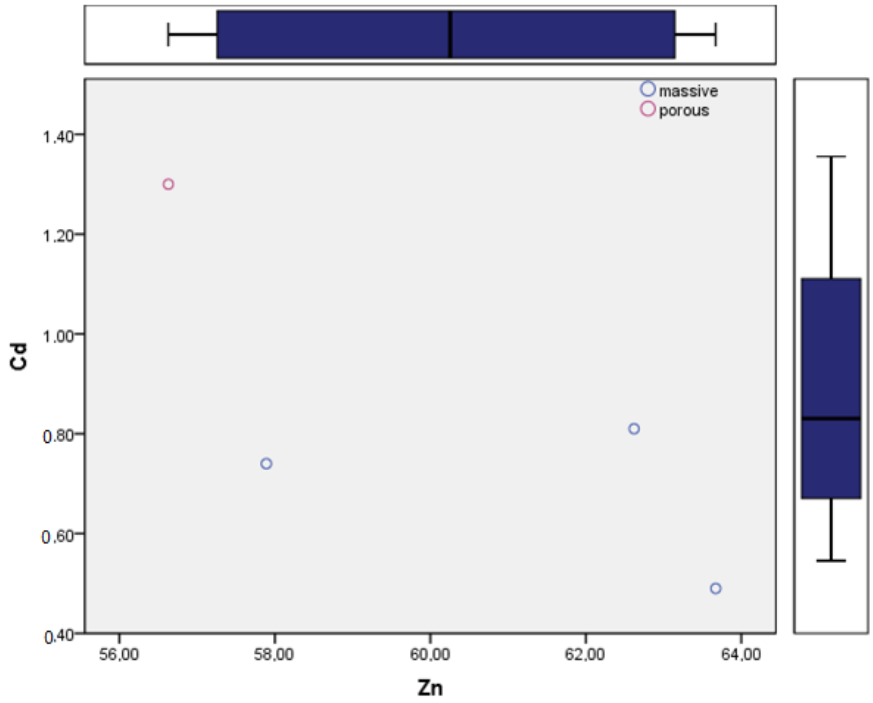

Figure 46: Binary correlation plot of Zn vs. Cd in zoned sphalerite with porous core and massive rim (Type 2).

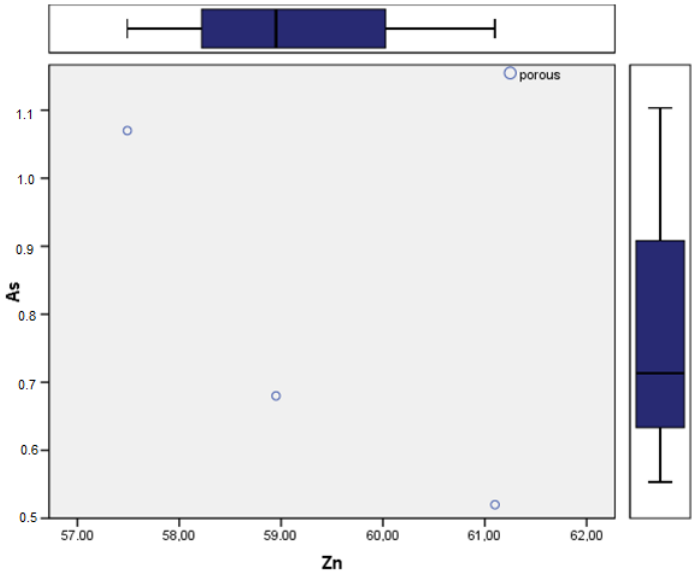

Figure 47: Binary correlation plot of Zn vs. As in zoned sphalerite with porous core and massive rim (Type 2).

6.1.3. Type 3: Inclusion-rich and compositionally zoned massive sphalerite

Reflected light microscopy and backscattered electron imaging revealed that the most commonly encountered sphalerite texture is massive sphalerite, comprising the third type of Kolumbo sphalerite **(Figs. 48, 49, 50, 51)**. Sphalerite type 3 is found either rich in randomly **(Fig. 48)** or linear **(Fig. 49)** distributed inclusions, inclusion-free **(Fig. 50)** or compositionally zoned **(Fig. 51)**. The latter displays a chemical zoning expressed by trace metal poor cores and trace metal-rich rims, as well as growth and sector zones < 1 μm thick enriched with Sb, Cu and Ag **(Table 6)**. Among the various inclusions found in sphalerite type 3, inclusions of Hg-Cd sulfosalts **(Fig. 52)** were also analyzed **(Table 7)**.

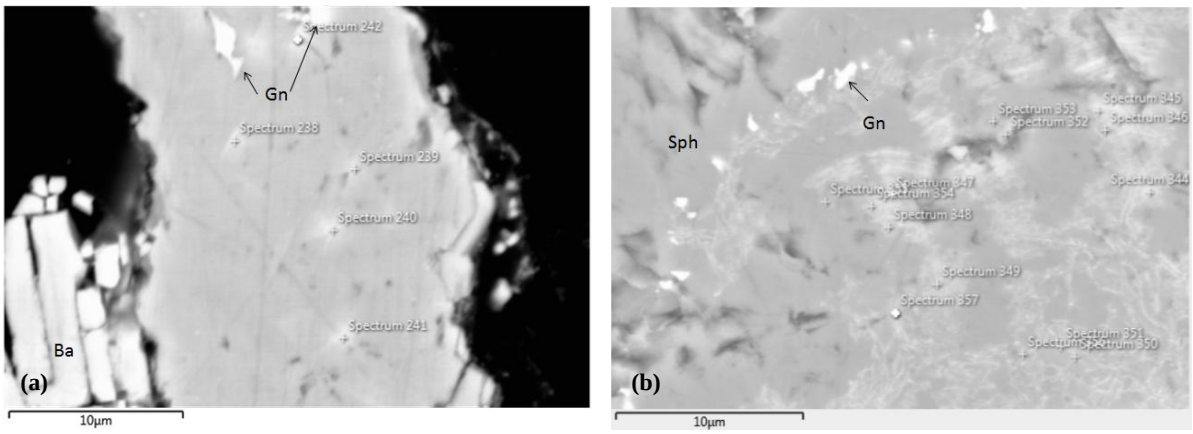

Figure 48: ESEM photograph of (a) inclusion-rich, massive sphalerite (type 3) with randomly dispersed inclusions, in association with barite (Ba). (b) galena (Gn) inclusions and symplectites of Pb–Sb-Hg bearing phases in inclusion-rich, massive sphalerite of Type 3.

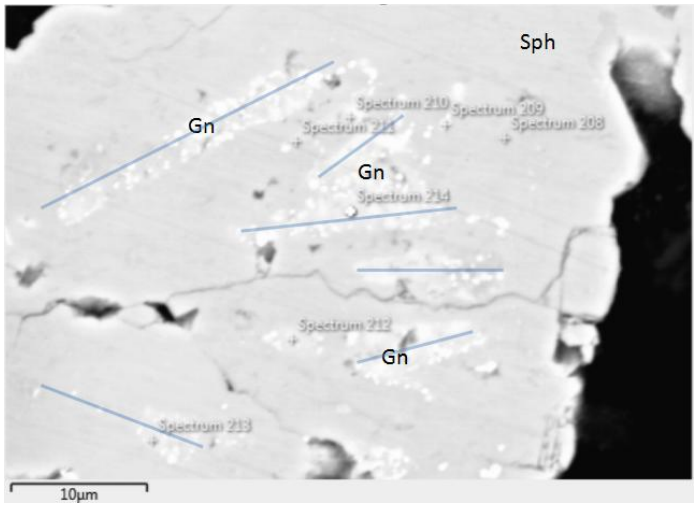

Figure 49: ESEM-BSE photograph of inclusion-rich, massive sphalerite (type 3) containing ubiquitous galena (Gn) inclusions arranged mainly in thick linear patterns.

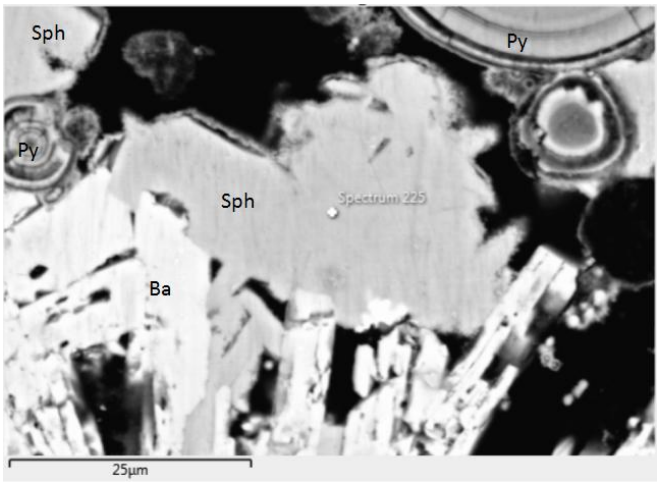

Figure 50: ESEM photograph showing the association between massive sphalerite of type 3 and colloform pyrite (Py), and barite (Ba) blades.

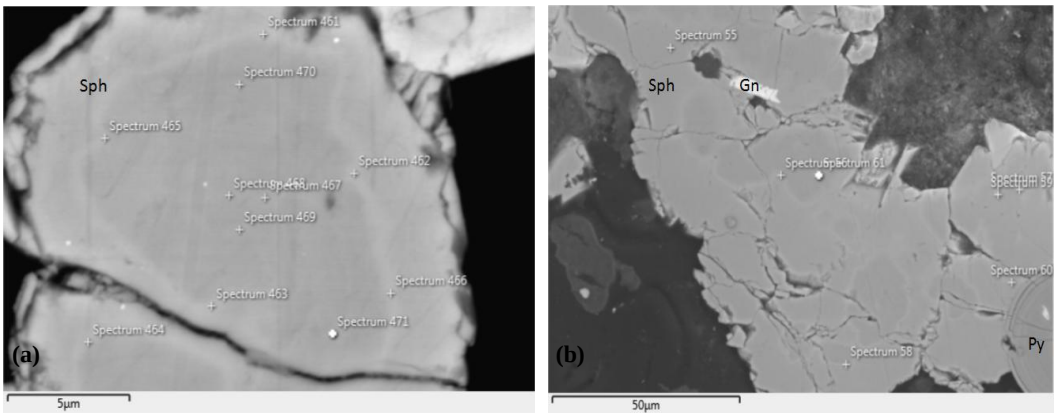

Figure 51: BSE-ESEM image of (a) type 3 massive, zoned sphalerite (Sph) grain with core separated from rim by a thin sectorial zone (type 3). (b) Type 3 massive, zoned sphalerite (Sph) grain with core separated from rim by a thin sectorial zone (type 3), galena (Gn) inclusions and pyrite (Py).

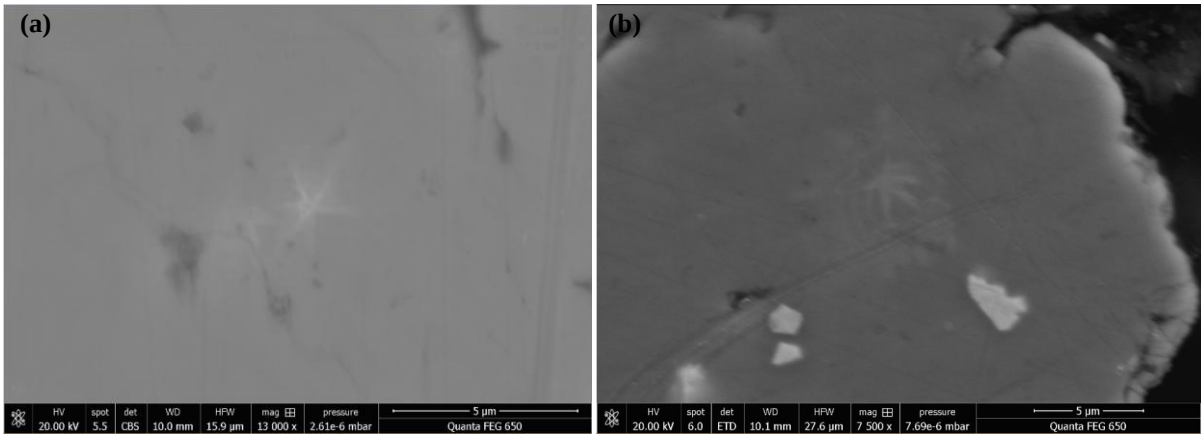

Figure 52: ESEM photograph of Hg-Cd sulfosalt inclusions in inclusion-rich, massive sphalerite (type 3) (a) in the form of "star-like" inclusions (b) in the form of "star-like" inclusion encircled in Hg-Cd-rich rim.

6.2. Quantitative EPMA analysis, compositional mapping and element distribution and correlation trends of sphalerite type 3

The absolute concentrations, normalized to 100%, for Fe, Sb and Cd in massive and compositionally zoned massive sphalerite of type 3 are summarized as histograms in **Figures 53, 54, 55, 56, 57,** and **58.** Whereas more trace elements (Cu, As, Ag, Hg and Pb) in massive sphalerite of type 3 and Cu and Ag in compositionally zoned massive sphalerite were also detected during electron microprobe (EPMA) analyses, their quantity was not enough to be displayed in histograms.

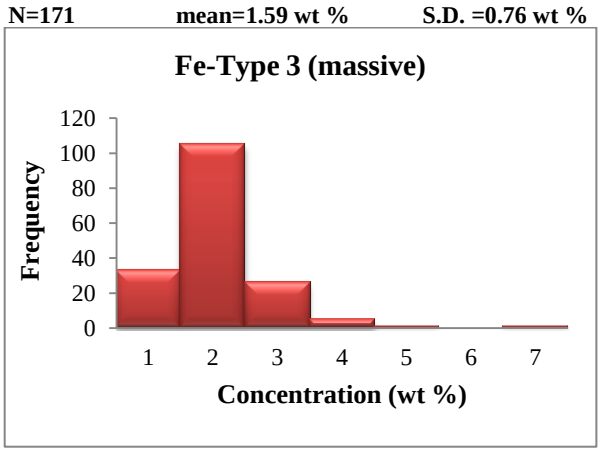

Figure 53: Histogram showing the variation in Fe in massive sphalerite of type 3 from Kolumbo hydrothermal precipitates.

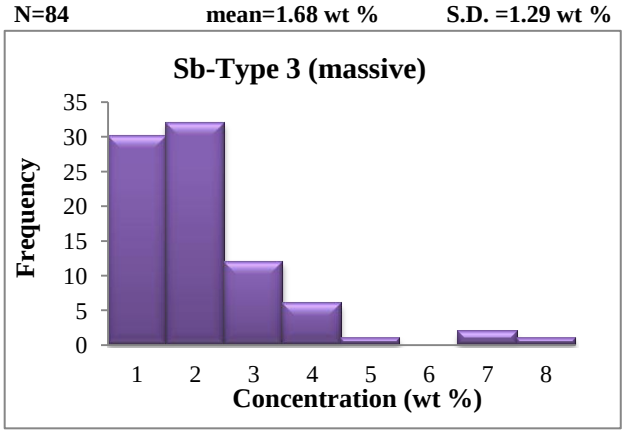

Figure 54: Histogram showing the variation in Sb in massive sphalerite of type 3 from Kolumbo hydrothermal precipitates.

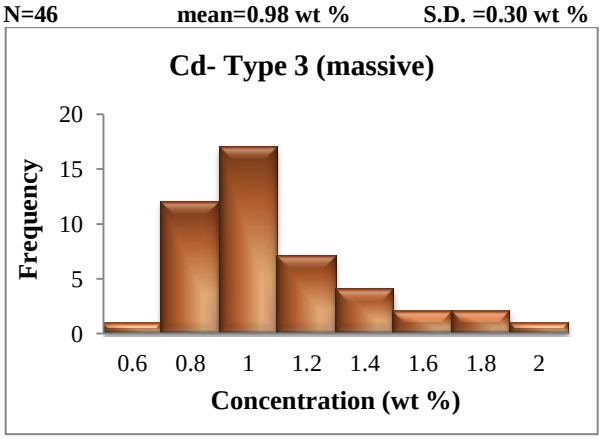

Figure 55: Histogram showing the variation in Cd in massive sphalerite of type 3 from Kolumbo hydrothermal precipitates.

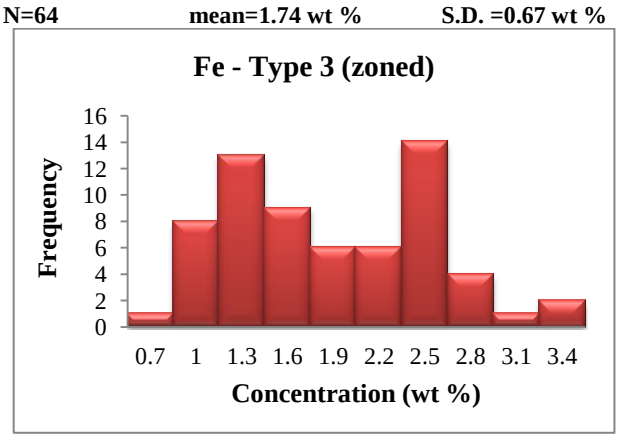

Figure 56: Histogram showing the variation in Fe in compositionally zoned, massive sphalerite of type 3 from Kolumbo hydrothermal precipitates.

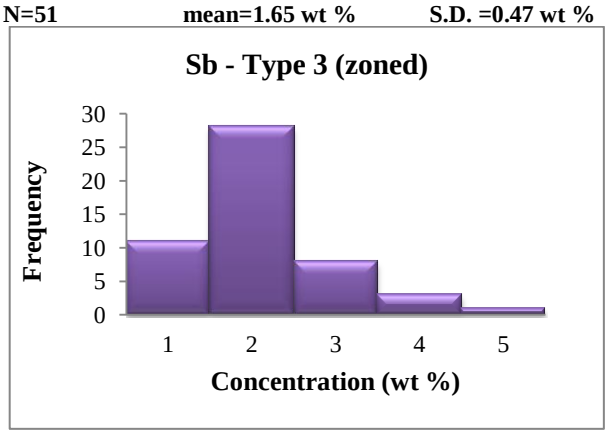

Figure 57: Histogram showing the variation in Sb in compositionally zoned, massive sphalerite of type 3 from Kolumbo hydrothermal precipitates.

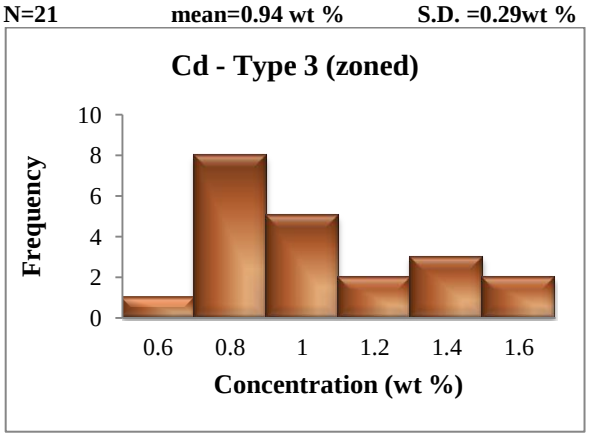

Figure 58: Histogram showing the variation in Cd in compositionally zoned, massive sphalerite of type 3 from Kolumbo hydrothermal precipitates.

A total of 235 EPMA analyses were carried out on sphalerite type 3. EPMA analyses conducted massive sphalerite of type 3 in which concentrations of ten elements (S, Zn, Fe, Cu, Cd, Sb, As, Ag, Hg and Pb) were determined using EDS mode. Electron probe microanalyses (EPMA-EDS) of samples SB-3-D, SB-3-E1,SB-7-A, SB-9-C, SB-10-A and SB-12-A for major, minor and trace elements with number of analyses (n), means, standard deviations (1σ SD), maxima, minima and limits of detection (LOD) are listed in **Table 6**. Additionally, for the compositionally zoned, massive sphalerite of type 3, concentrations of seven elements (S, Zn, Fe, Sb, Cu, Cd and Ag) were determined using EDS mode. Electron probe microanalyses (EPMA-EDS) of samples SB-3-D2, SB-3-E2, SB-10-A and SB-12-A A for major, minor and trace elements with number of analyses (n), means, standard deviations

(1σ SD), maxima, minima and limits of detection (LOD) are listed in **Table 6**. Complete EPMA datasets of sphalerite type3 can be found in the Appendix.

The EPMA analyses for Kolumbo type 3 sphalerites are grouped in (i) 171 analyses from the massive sphalerite of type 3 and (ii) 64 from the compositionally zoned, massive sphalerite of type 3 **(Table 6)**. Massive sphalerite is composed of 50.53 to 70.18 wt % Zn (61.55±2.87 wt %) and 28.22 to 45.87 wt % S (35.55±2.54 wt %). Fe is ubiquitous in massive sphalerite 3, with contents varying between 0.37 and 6.08 wt % (mean 1.59±0.76 wt %); Cd concentrations range between 0.56 and 1.86 wt %. Additionally, Cu (up to 2.55 wt %), As (up to 0.78 wt % and Ag (up to 1.15 wt %), were also detected but only in a few number of analyses. Hg (2.77 and 3.10 wt %) and Pb (5.43 and 6.79 wt %) were also found just in two analysis. Compositionally zoned, massive sphalerite of type 3 is composed of 37.86 to 63.66 wt % Zn (60.47±4.10 wt %) and 33.97 to 56.04 wt % (35.84±3.80 wt %) S. Fe is detected in all compositionally zoned, massive sphalerite of type 3 analyzed, with contents varying between 0.66 to 3.35 wt % (mean 1.74±0.67 wt %). Sb concentrations range between 0.47 and 4.20 wt % (mean 1.65±0.85 wt %) and Cd from 0.59 to 1.54 wt % (mean 0.94±0.29 wt %), whereas Cu (up to 2.39 wt %) and Ag (up to 1.48 wt %) were also detected but only in a few number of analyses. Concentrations of As were below the detection limit of the instrument.

Table 6: EMPA main results from the massive sphalerite and the compositionally zoned massive sphalerite (type 3). Minimum, maximum, mean, corresponding standard deviation (1σ SD), and limit of detection (LOD) are presented.

Type 3		S (wt %)	Fe (wt %)	Zn (wt %)	Sb (wt %)	Cu (wt %)	Cd (wt %)	As (wt %)	Ag (wt %)	Hg (wt %)	Pb (wt %)
Massive	n^	171	171	171	84	8	46	7	6	2	2
	Min.	28.22	0.37	50.53	0.55	0.70	0.56	0.16	0.54	2.77	5.43
	Max.	45.88	6.08	70.18	7.03	2.55	1.86	0.78	1.15	3.1	6.79
	Mean	35.55	1.59	61.55	1.68	1.15	0.98	0.35	0.78	2.94	6.11
	1σ SD	2.54	0.76	2.87	1.29	0.64	0.30	0.26	0.21	0.23	0.97
Compositionally Zoned	n^	64	64	64	51	9	21	-	7	-	-
	Min.	33.97	0.66	37.86	0.47	0.63	0.59	-	0.63	-	-
	Max.	56.04	3.35	63.66	4.21	2.39	1.54	-	1.48	-	-
	Mean	35.84	1.74	60.47	1.65	1.41	0.94	-	1.03	-	-
	1σ SD	3.80	0.67	4.10	0.85	0.68	0.29	-	0.29	-	-
LOD		0.1	0.1	0.1	0.1	0.1	0.1	0.1	0.1	0.1	0.1

^ n: number of measurements with higher contents than the limit of detection.
- Concentrations below the detection limit.

Massive sphalerite is the type which contains large amount of inclusions, among other galena, Sb-Pb- and Hg-Cd- sulfosalts **(Figs. 48, 49, 52)**. For that reason, 125 EMPA-WDS

analyses were conducted in order to measure Hg concentrations in the Hg-Cd sulfosalt inclusions of massive sphalerites in samples SB-3-E and SB-7-A. Electron microprobe (EMPA - WDS) analyses of samples SB-3-E, SB-7-A and the mean of both samples analyses for Hg with number of analyses (n) means, standard deviations (1σ SD), maxima, minima and limits of detection (LOD) are listed in **Table 7**.

For massive sphalerite of type 3, Hg content in Hg-Cd sulfosalts varies from 3.81 to 47.17 wt % (mean 18.28±13.50 wt %) in sample SB-3-E1, from 4.99 to 24.96 wt % (mean 13.45±4.84 wt %) in sample SB-3-E2 and from 1.19 to 9.17 wt % (mean 5.76±1.55 wt %) in sample SB-7-A **(Table 7)**.

Table 7: EMPA-WDS main results of Hg from the Hg-Cd sulfosalt inclusions of massive sphalerite (type 3) in samples SB-3-E, SB-7-A and the mean of both samples analyses. Minimum, maximum, mean, corresponding standard deviation (1σ SD), and limit of detection (LOD) are presented.

	SB-3-E1 (wt %)	SB-3-E2 (wt %)	SB-7-A (wt %)	Total
n	52	27	46	125
Min.	3.81	4.99	1.19	1.19
Max.	47.17	24.96	9.17	47.17
Mean	18.28	13.45	5.755	12.63
1σ SD	13.50	4.84	1.55	10.57
LOD	0.01	0.01	0.01	0.01

In order to examine potential chemical variations across massive sphalerite grains of type 3, systematic trace element concentration profiles were carried out by ESEM-EDS, as shown in **Figure 59**. Random trace metal distribution is observed, thus, systematic trace metal variations cannot be observed.

Respectively, in order to examine the possibility of chemical variation between the core, sector and rim of zoned massive sphalerite of type 3, **Table 8** was created, showing the single EPMA analyses of a such crystal, and systematic trace element concentration profiles were carried out by ESEM-EDS, as shown in **Figure 60**. Sphalerite core is separated from rim by a thin sectorial zone. The core contains Cd, Fe and Sb (analyses 1-4), the sector contains Ag, Cd, Fe, Sb and Cu (analyses 5-8) and the rim contains Sb and Fe (analyses 9-11).

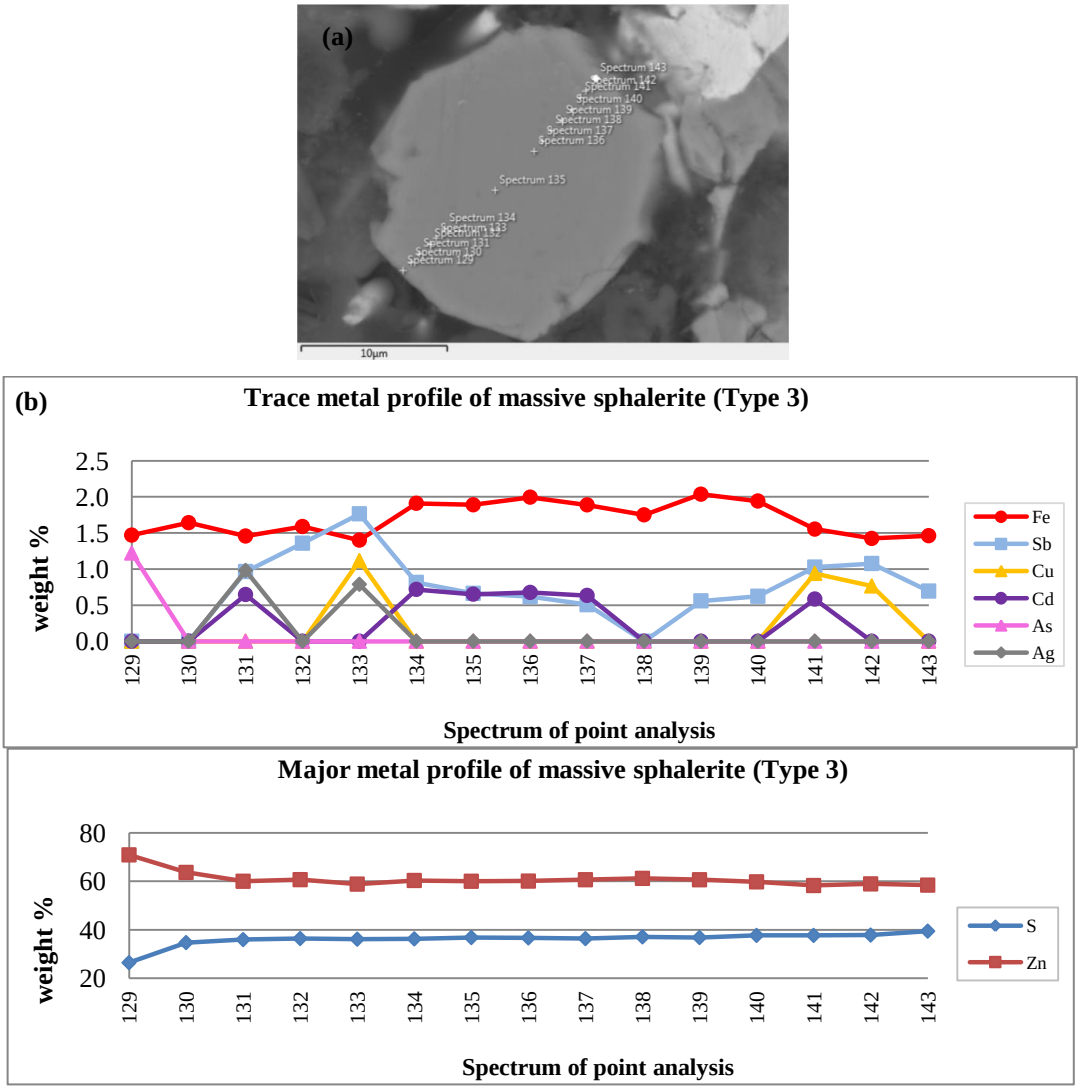

Figure 59: Geochemical profile across a massive type 3 sphalerite crystal. (a) Spots of EPMA analyses are represented by crosses accompanied by "Spectrum +number X" designation. (b) Random trace metal distribution is observed.

Table 8: Single EPMA analyses showing the element concentrations (wt %) of the core, sector and rim of zoned, massive type 3 sphalerite. The points of analysis are shown in Figure 60a.

	Point of analysis	S (wt %)	Fe (wt %)	Zn (wt %)	Sb (wt %)	Cu (wt %)	Cd (wt %)	Ag (wt %)	Total (wt %)
core	1	35.25	2.30	62.45	0.00	0.00	0.00	0.00	100.00
	2	35.40	2.78	61.18	0.00	0.00	0.64	0.00	100.00
	3	35.07	1.81	61.75	0.77	0.00	0.61	0.00	100.00
	4	35.16	2.18	61.95	0.00	0.00	0.71	0.00	100.00
sector	5	34.65	1.18	61.28	1.51	0.00	0.75	0.63	100.00
	6	36.13	1.15	60.66	2.06	0.00	0.00	0.00	100.00
	7	34.30	2.26	60.92	1.26	0.00	1.26	0.00	100.00
	8	34.58	1.51	60.60	2.32	0.99	0.00	0.00	100.00
rim	9	34.08	2.36	63.56	0.00	0.00	0.00	0.00	100.00
	10	34.27	1.87	62.87	1.00	0.00	0.00	0.00	100.00
	11	35.03	1.29	62.54	1.14	0.00	0.00	0.00	100.00

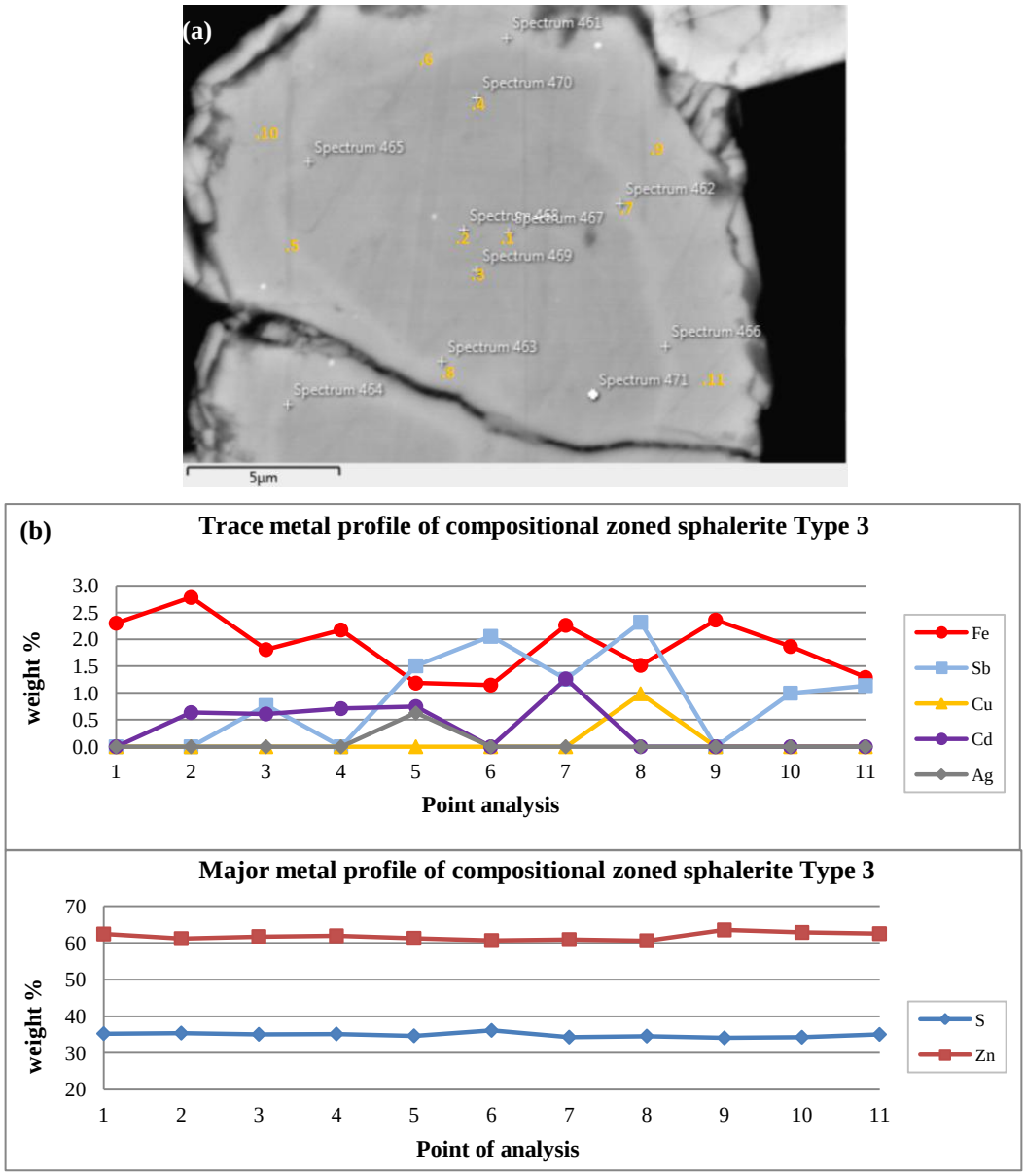

Figure 60: Geochemical profile across a zoned, massive type 3 sphalerite crystal. Analyses 1-4 refer to the core, 5-8 to the sector and 9-11 are from the rim of zoned, massive sphalerite crystal. (a) Spots of EPMA analyses are represented by the orange numbers. (b) The core contains Cd, Fe and Sb (analyses 1-4), the sector contains Ag, Cd, Fe, Sb and Cu (analyses 5-8) and the rim contains Sb and Fe (analyses 9-11).

In order to examine potential chemical variations within the inclusion-rich massive sphalerite of type 3, trace element mapping was carried out by ESEM-EDS (**Figs. 61, 62, 63).** The anhedral inclusions in **Figure 61** seem to contain Pb and Fe, while the symplectites are consisted of Sb, Pb and Hg. EDS elemental maps of Hg-Cd sulfosalt inclusions are shown in **Figure 62** and **63.** In **Figure 63** the Hg-Cd sulfosalt inclusions are found into a Sb-rich sphalerite area.

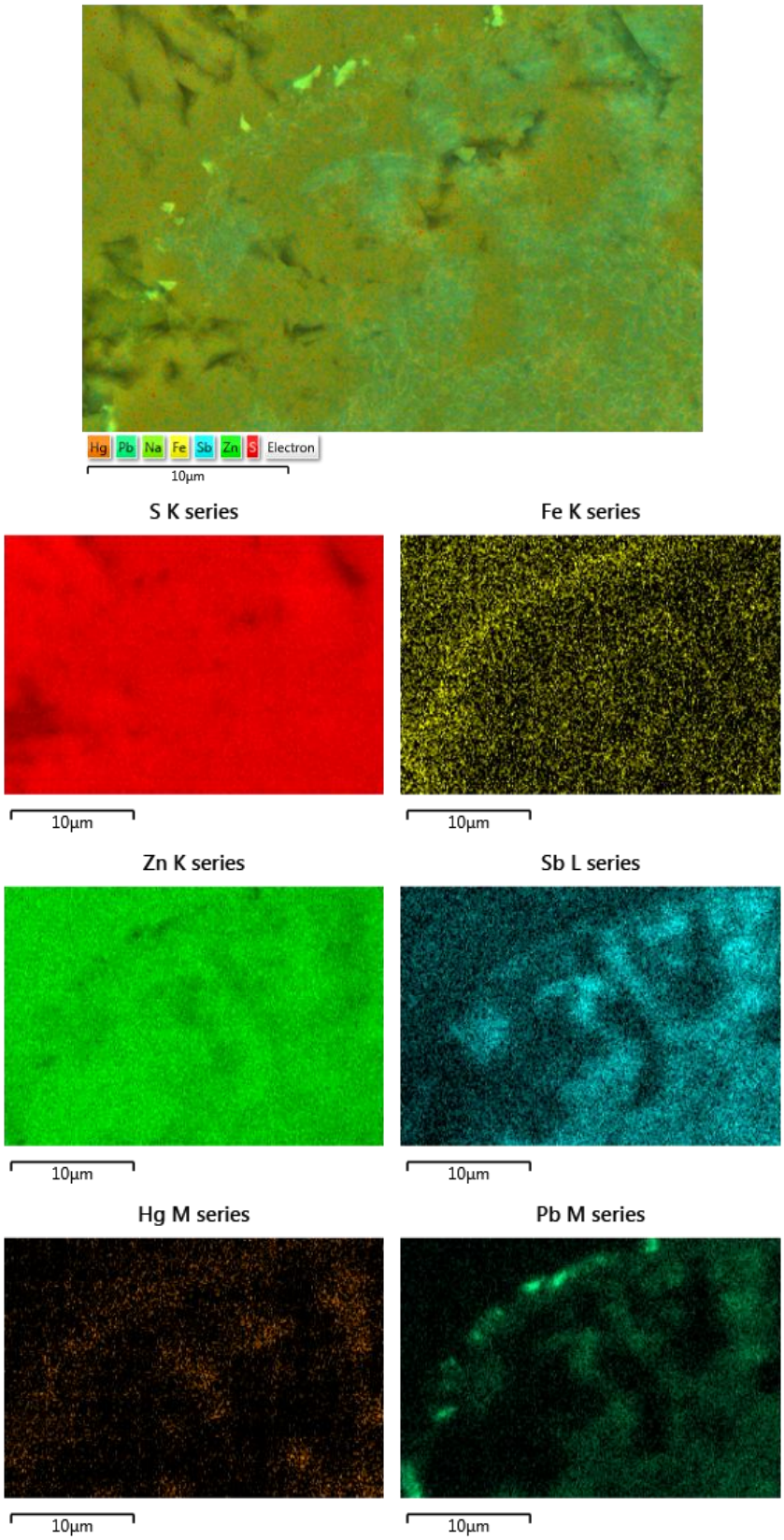

Figure 61: EDS elemental map of the inclusion-rich massive sphalerite of Figure 48b for S, Fe, Zn, Sb, Hg and Pb. The anhedral inclusions contain Fe and Pb, while the symplectites consist of Sb and Pb.

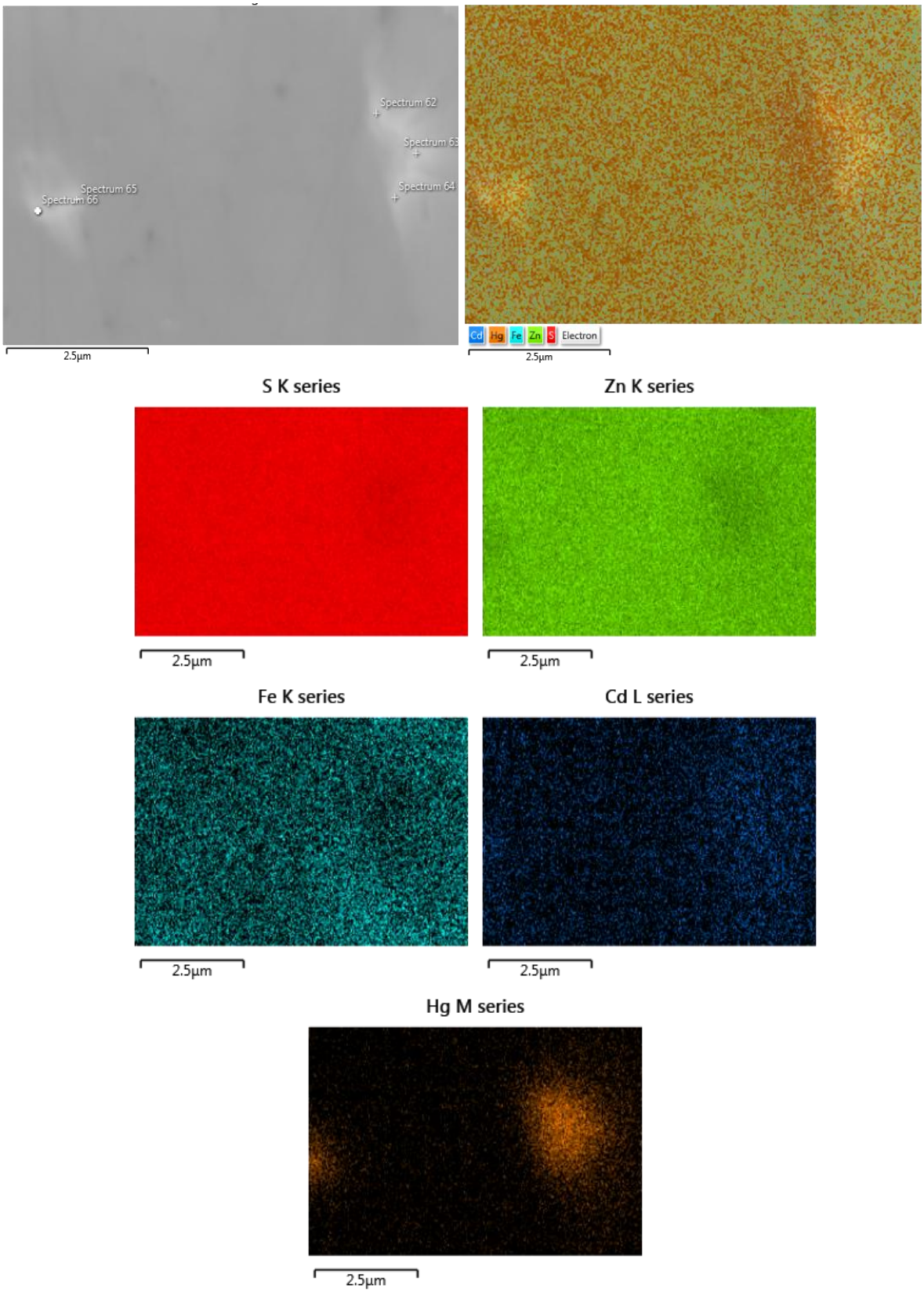

Figure 62: EDS elemental map of a Hg-Cd inclusion in massive type 3 sphalerite for S, Zn, Hg, Fe and Cd.

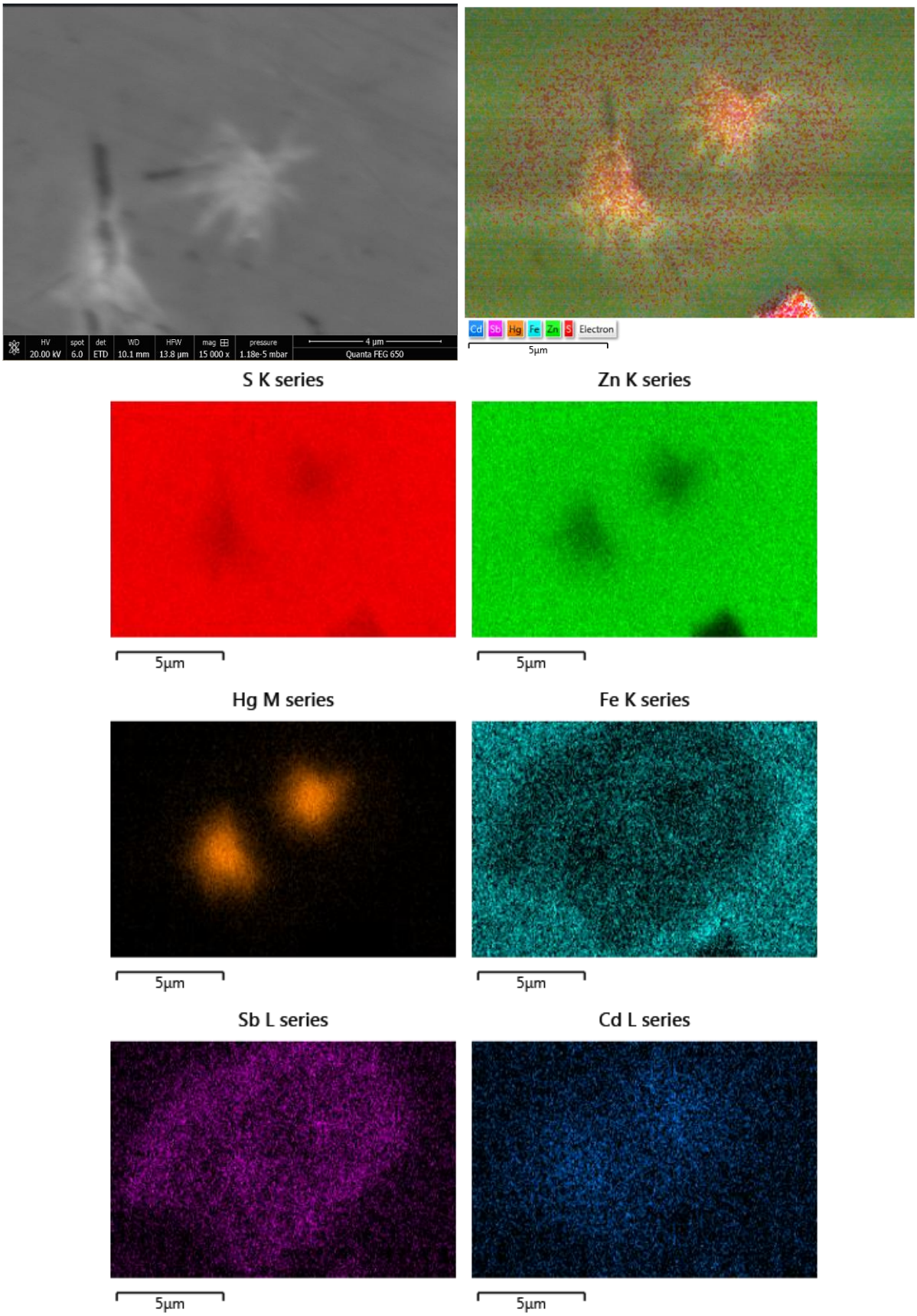

Figure 63: EDS elemental map for S, Zn, Hg, Fe, Sb and Cd depicting of a Hg-Cd inclusion into a Sb-rich area of massive type 3 sphalerite

In **Figures 64, 65 66,** the correlation between Zn and the other detected trace elements (Fe, Sb and Cd) in massive sphalerite of type 3 is illustrated. It is not possible to come to any conclusion for the correlation of Zn with As, Ag and Cu **(Fig. 67)** because of the limited number of analyses for the aforementioned trace metals. Respectively, the correlation between Zn and the other trace elements (Fe, Sb and Cd) in zoned, massive sphalerite of type 3 is depicted in **Figures 68, 69, 70,** while for the correlation between Zn with Cu and Ag it is not possible to come to any conclusion because of the scarcity in the number of analyses for them **(Figs. 71, 72).**

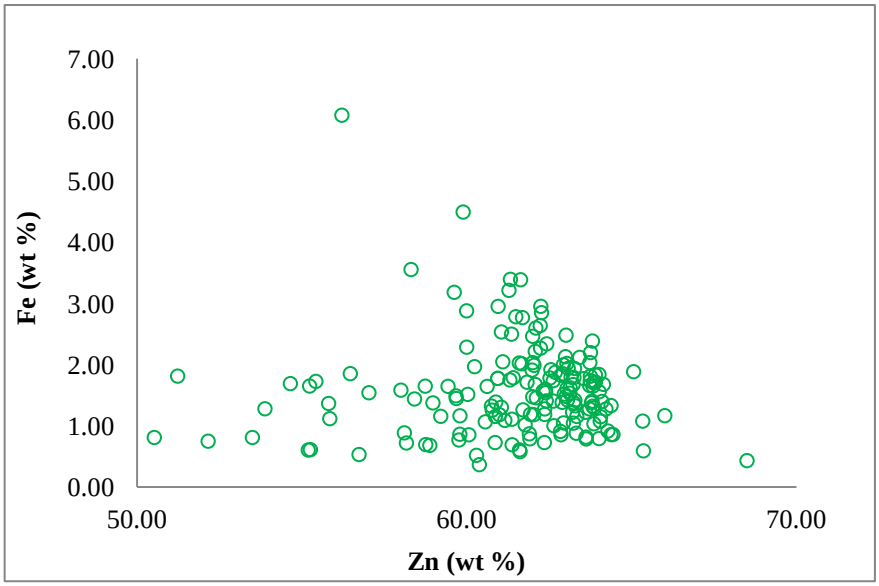

Figure 64: Binary correlation plot of Zn vs. Fe in massive sphalerite (Type 3).

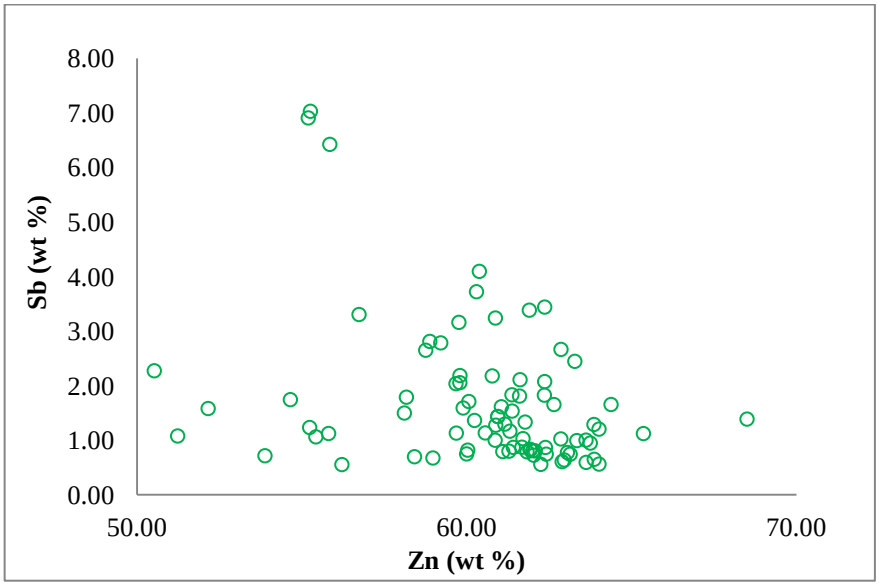

Figure 65: Binary correlation plot of Zn vs. Sb in massive sphalerite (Type 3).

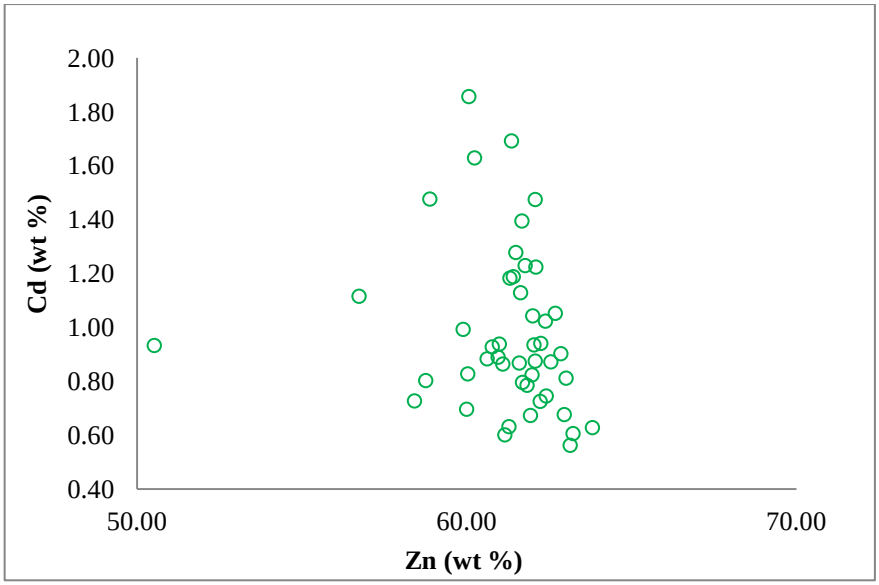

Figure 66: Binary correlation plot of Zn vs. Cd in massive sphalerite (Type 3).

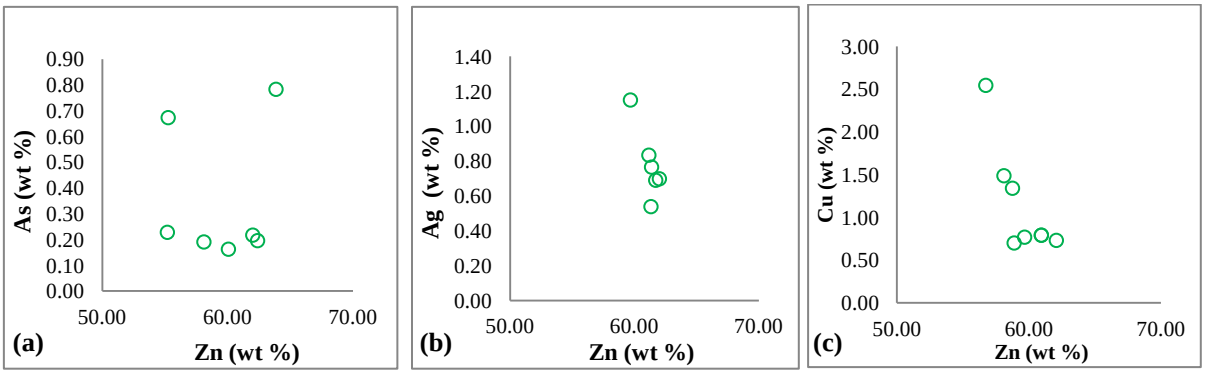

Figure 67: Binary correlation plot of (a) Zn vs. As, (b) Zn vs. Ag and (c) Zn vs. Cu in massive sphalerite (Type 3).

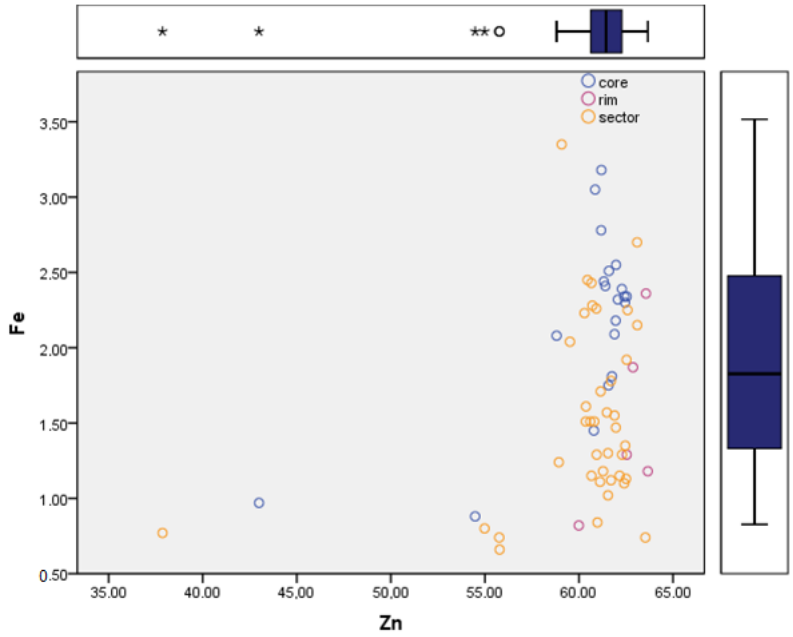

Figure 68: Binary correlation plot of Zn vs. Fe in zoned, massive sphalerite (Type 3).

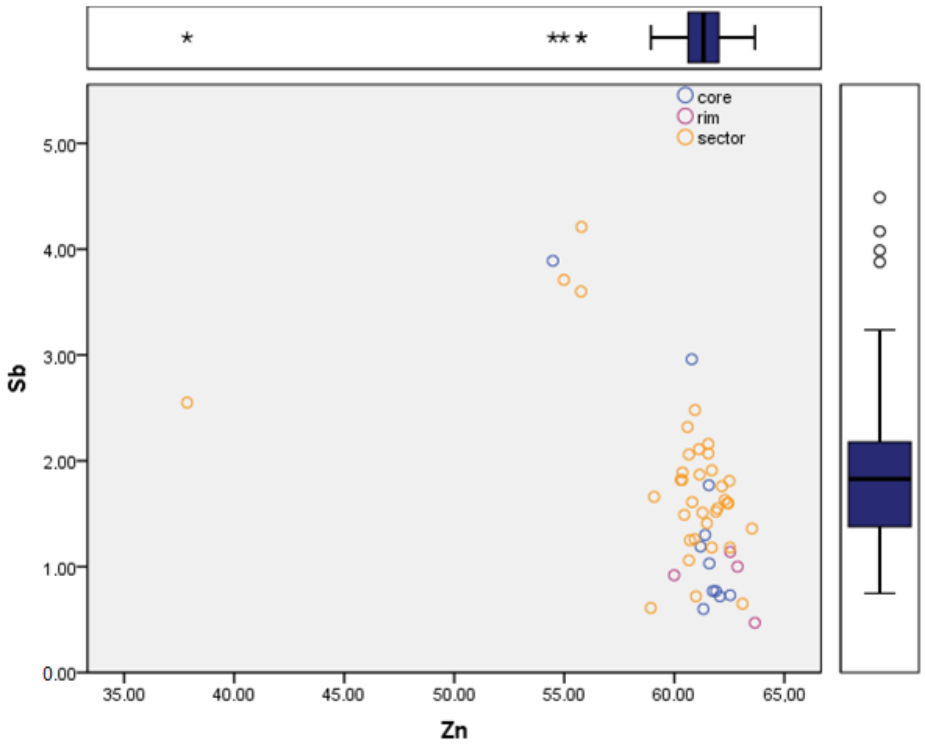

Figure 69: Binary correlation plot of Zn vs. Sb in zoned, massive sphalerite (Type 3).

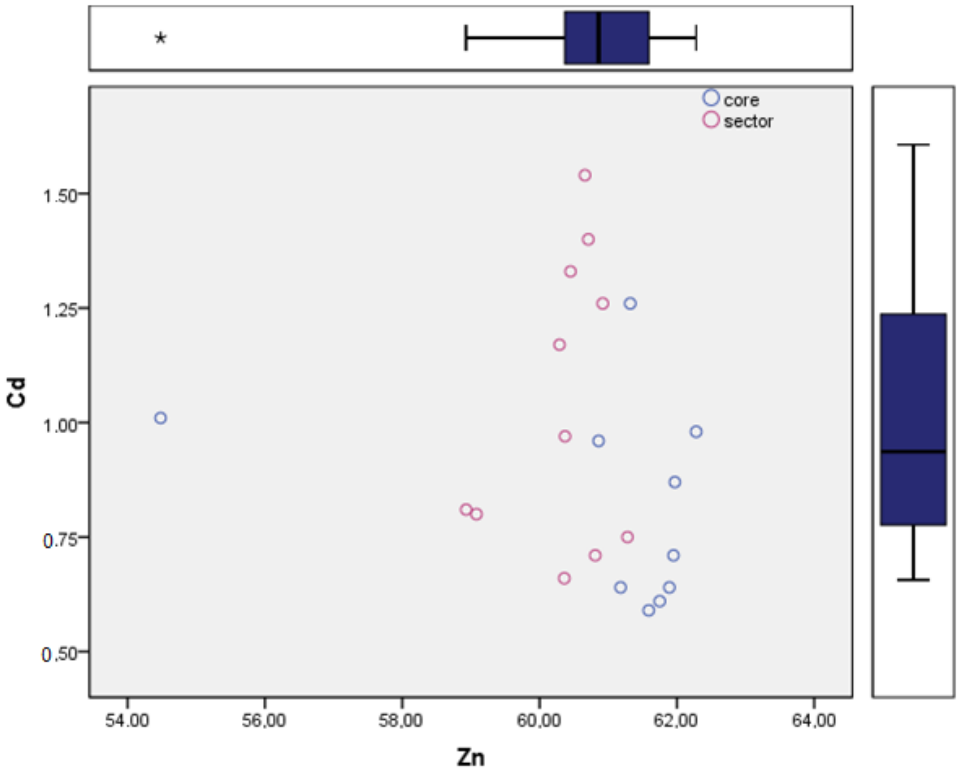

Figure 70: Binary correlation plot of Zn vs. Cd in zoned, massive sphalerite (Type 3).

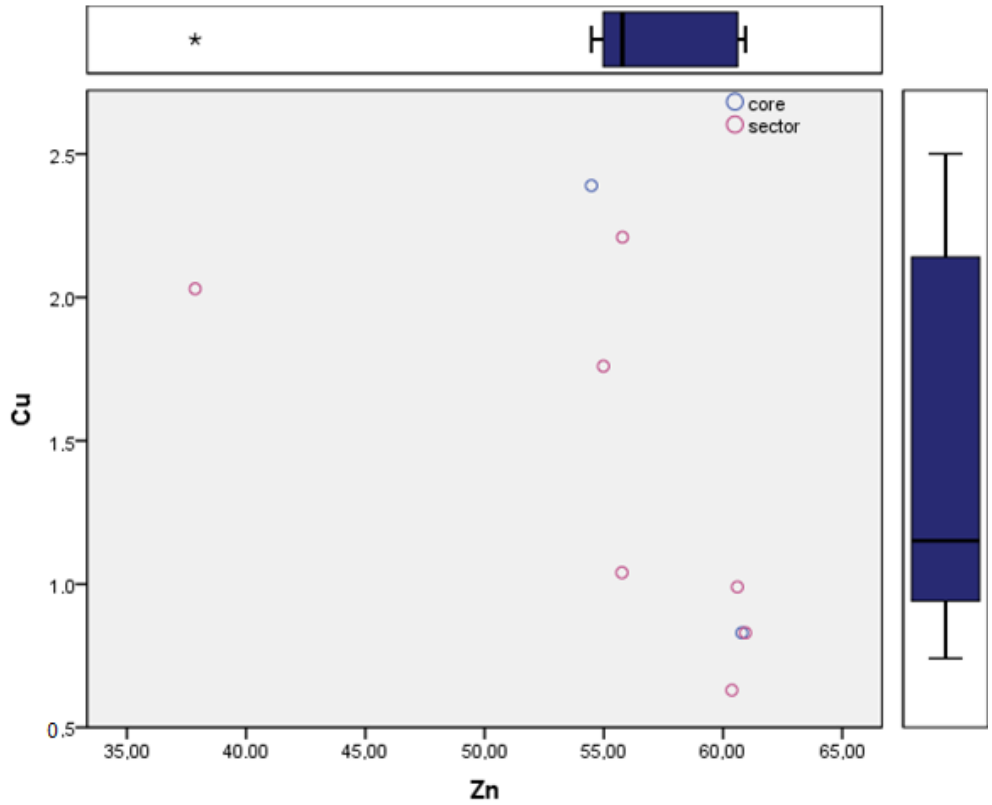

Figure 71: Binary correlation plot of Zn vs. Cu in zoned, massive sphalerite (Type 3).

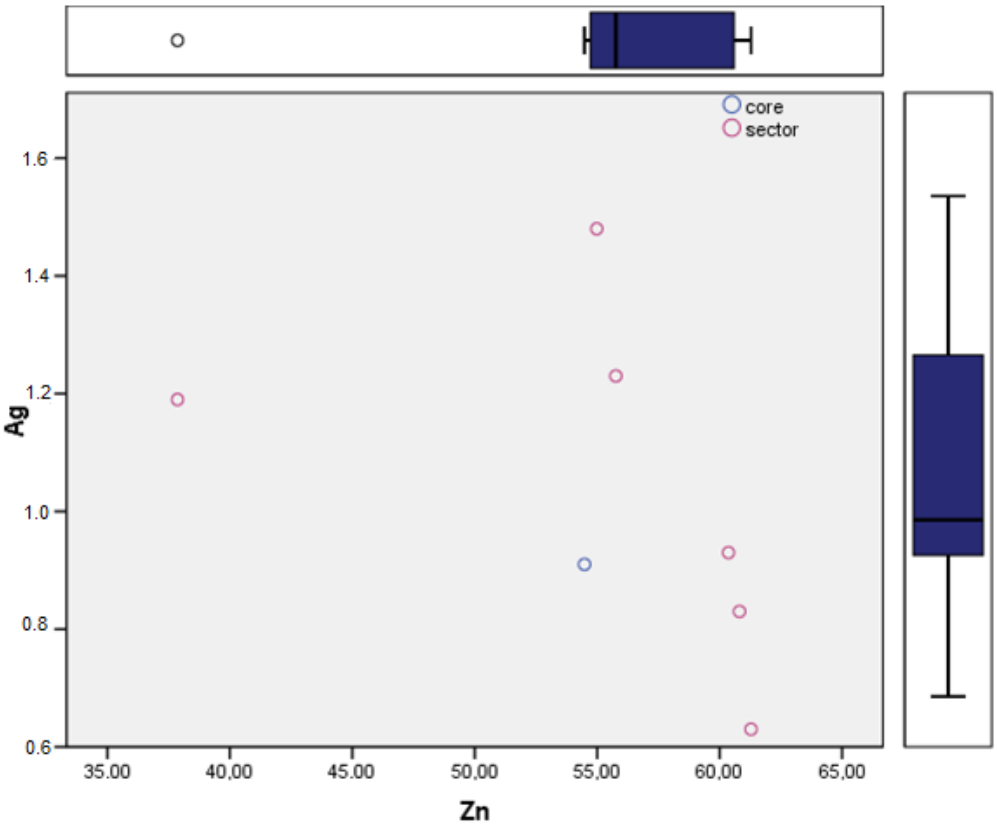

Figure 72: Binary correlation plot of Zn vs. Ag in zoned, massive sphalerite (Type 3).

7. Discussion

7.1 Structural and chemical variation of sphalerite crystals and control of trace element distribution

Recent work by **Wohlgemuth-Ueberwasser et al. (2015)** has shown that the factors that control the distribution of trace metals (i.e. As, Sb, Au) in seafloor chimney sulfide minerals may be: (1) the nature of the rocks hosting the hydrothermal vent system, (2) the physicochemical conditions of sulfide precipitation (i.e. fluid chemistry, oxidation state, and fluid temperature) within seafloor chimneys, (3) the amounts of co-precipitated sulfides and whether they constitute equilibrium/disequilibrium assemblages, and (4) the extent of modification of trace metal distribution in chimney sulfides due to dissolution–reprecipitation processes within the hydrothermal vent precipitates during later stage hydrothermal activity.

The results of this thesis have shown that bulk trace metal concentrations of Hg and Ag are controlled by the modal abundance of sphalerite and its modifications during the course of dissolution–reprecipitation processes during chimney growth and evolving hydrothermal activity. For seafloor hydrothermal vent precipitates, mineral texture is accepted as a measure of these modifications, i.e. variability of mineral textures is associated with initial crystallization as well as subsequent recrystallization, which also influence the mobility and redistribution of trace metals among the various minerals present and textural variants of the same phase (**Wohlgemuth-Ueberwasser et al. 2015**). Colloform textures are known to indicate primary seafloor precipitation textures formed directly from hydrothermal fluids via rapid crystallization due to mixing of hot hydrothermal fluids with ambient seawater, most likely during the early stages of chimney growth (**Xu & Scott 2005, Berkenbosch et al. 2012, Keith et al. 2016**); more compact but still porous textures represent an intermediate stage of the modification of primary precipitates (i.e. colloform textures), and the final stage of replacement and recrystallization is represented by well-defined, massive textures consisting of interlocking, subhedral to euhedral minerals (**Keith et al. 2016, Wohlgemuth-Ueberwasser et al. 2015, Hannington et al. 1998, Maslennikov et al. 2009**).

On the above basis, the three sphalerite textural varieties that have been distinguished in the Kolumbo samples are interpreted to be associated with initial crystallization as well as subsequent transformation/recrystallization. Specifically, the most immature primary textures are colloform zoned sphalerite (Type 1) which highly likely formed directly from hydrothermal fluids **(Fig. 73a, b).** Zoned sphalerite with porous core and massive rim (Type

2; **Fig. 73c, d**) represent the intermediate stage of the modification of primary colloform precipitates (Type 1) to fully massive texture (Type 3; **Fig. 73e, f**), as porosity is reduced during replacement and recrystallization processes **(Hannington et al. 1995);** the textural relationship of subhedral massive sphalerite embracing earlier formed colloform sphalerite shows that these two sphalerite generations can be locally observed **(Fig. 28a)**. The final stage of replacement and recrystallization is represented by samples with well-defined anhedral to subhedral sphalerite textures characterized by random anhedral mineral inclusions and/or chemical zoning (Type 3).

The trace metal mobility, and consequent chemical progression, during the sphalerite textural evolution is demonstrated by: **(1)** The change from systematic trace metal variation in microglobular sphalerite (type 1) where Hg, Cd, and Sb are distributed in concentric sectorial growth zones **(Fig. 33)**, to random, and/or systematic, redistribution of these metals in sphalerite types 2 and 3 chiefly in mineral inclusions, or different sectors, respectively (see **Figs. 42, 59, 60, 61, 62, 63, 74**; see also below); it should be noted that type 1 sphalerite contains also trace Ag, Cu, and As concentrations which were detected in these growth zones during spot analysis **(Appendix Table 1)**. The above change in trace metal distribution, combined with the associated textural modification, suggests that trace metals were expelled from sphalerite 1 during dissolution–reprecipitation processes, and were fractionated in sphalerite 2 and 3 mostly as independent micro-, and possibly nano-particulate, phases (see below). Moreover, subhedral and anhedral sphalerites of type 2 and 3 are chemically indistinguishable in most trace elements, which support our conclusion that these different textures are due to dissolution processes (**c.f. Keith et al. 2016**) **(Fig. 74a-d)**; **(2)** Systematic trace element variations between different sectoral zones of sphalerite 2. For Sb, Ag and Cu the highest concentrations were observed in the porous innermost cores of the sphalerite crystals **(Fig. 42, Table 5)**. This can be explained by variable fluid conditions during sphalerite growth from porous to massive and/or fractionation of the studied trace metals due to physicochemical changes in the parental fluids during sphalerite 2 precipitation (**Keith et al. 2016; Wohlgemuth-Ueberwasser et al. 2015)**. More specifically, these variations in trace element chemistry probably reflect a decreasing solubility of Sb, Ag and Cu, and increasing solubility of Fe and Cd, during sphalerite growth due to changes in the physicochemical parameters of the discharging fluids **(c.f. Maslennikov et al. 2009, Revan et al. 2014, Wohlgemuth-Ueberwasser et al. 2015, Keith et al. 2016)**; **(3)** the fractionation and concentration of Hg, Cd, Pb and Sb into discrete Hg-Cd sulfosalts and Sb-Pb symplectites within type 3 sphalerite (see EDS elemental maps in **Figures 61, 62, 63**); and, **(4)** Variations

in trace metal chemistry between the central and outer parts of zoned type 3 sphalerite **(Fig. 60)**; depletion of Cd towards the outer parts of sphalerite crystals, which are separated from the central part by a thin sectorial zone rich in trace Ag, Cd, Fe, Sb, and Cu (see geochemical profile of **Figure 60)**.

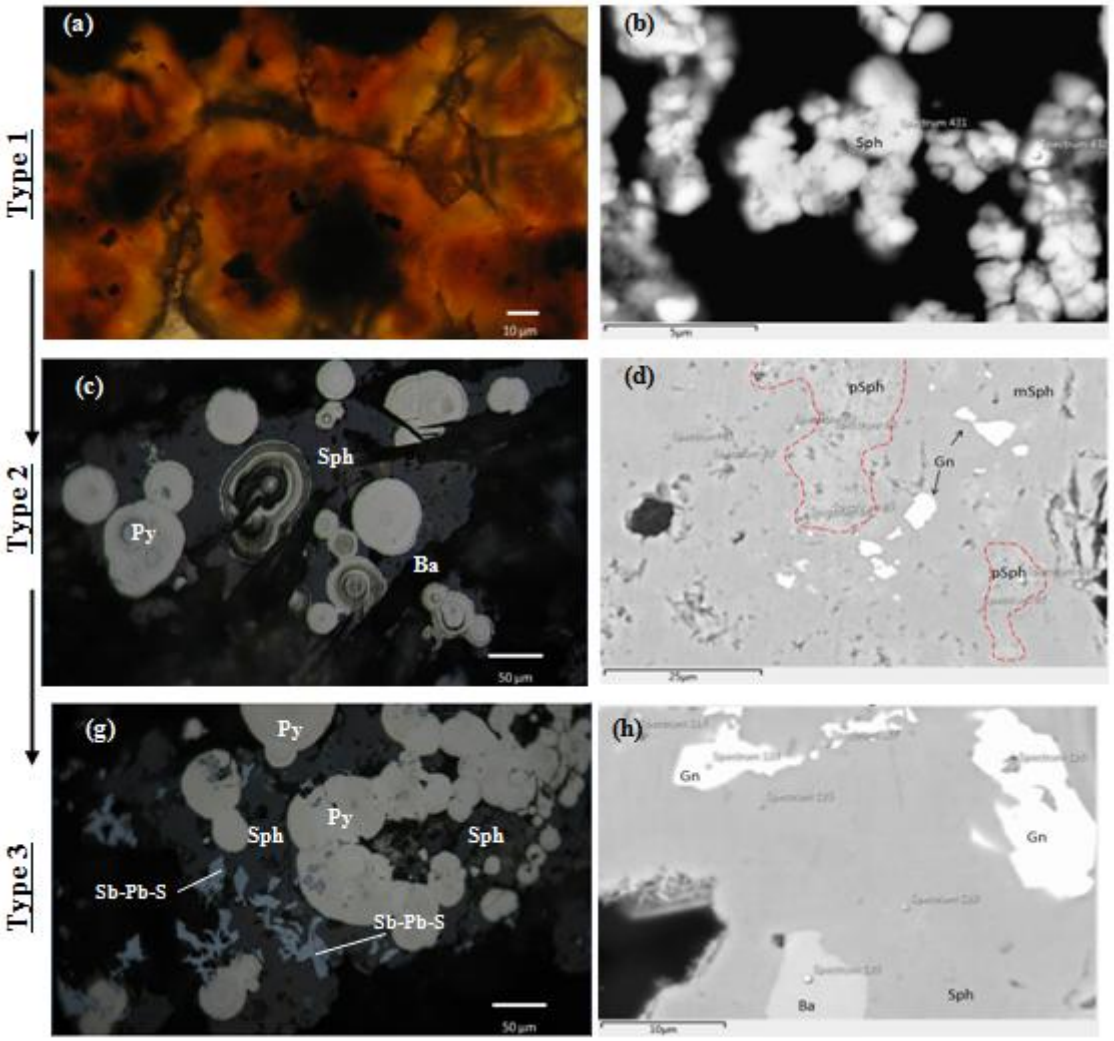

Figure 73: The three sphalerite textural varieties arranged in order of maturity. a) Transmitted light microphotograph (TLP) of colloform zoned sphalerite (Type 1) (oil lens and //Nichols). b) ESEM photograph of sphalerite (Sph) colloform microglobules (Type 1). c) Reflected light microphotograph (RLP) of zoned sphalerite with porous core and massive rim (Sph) (Type 2), having inclusions of colloform pyrite/marcasite (Py) and being in association with blades of barite (Ba) (oil lens and // Nichols). d) ESEM photograph of sphalerite with porous core (pSph) and massive rim (mSph) (Type 2) with voids (dark) and galena (Gn) inclusions. g) Reflected light microphotograph (RLP) of inclusion-rich and compositionally zoned massive sphalerite (Sph) (Type 3) with inclusions of closely-packed pyrite globules (Py) and anhedral Sb-Pb-sulfosalts (oil lens and // Nichols). h) ESEM photograph of compositionally zoned massive sphalerite (Sph) (Type 3) containing galena inclusions (Gn) and barite (Ba) blades.

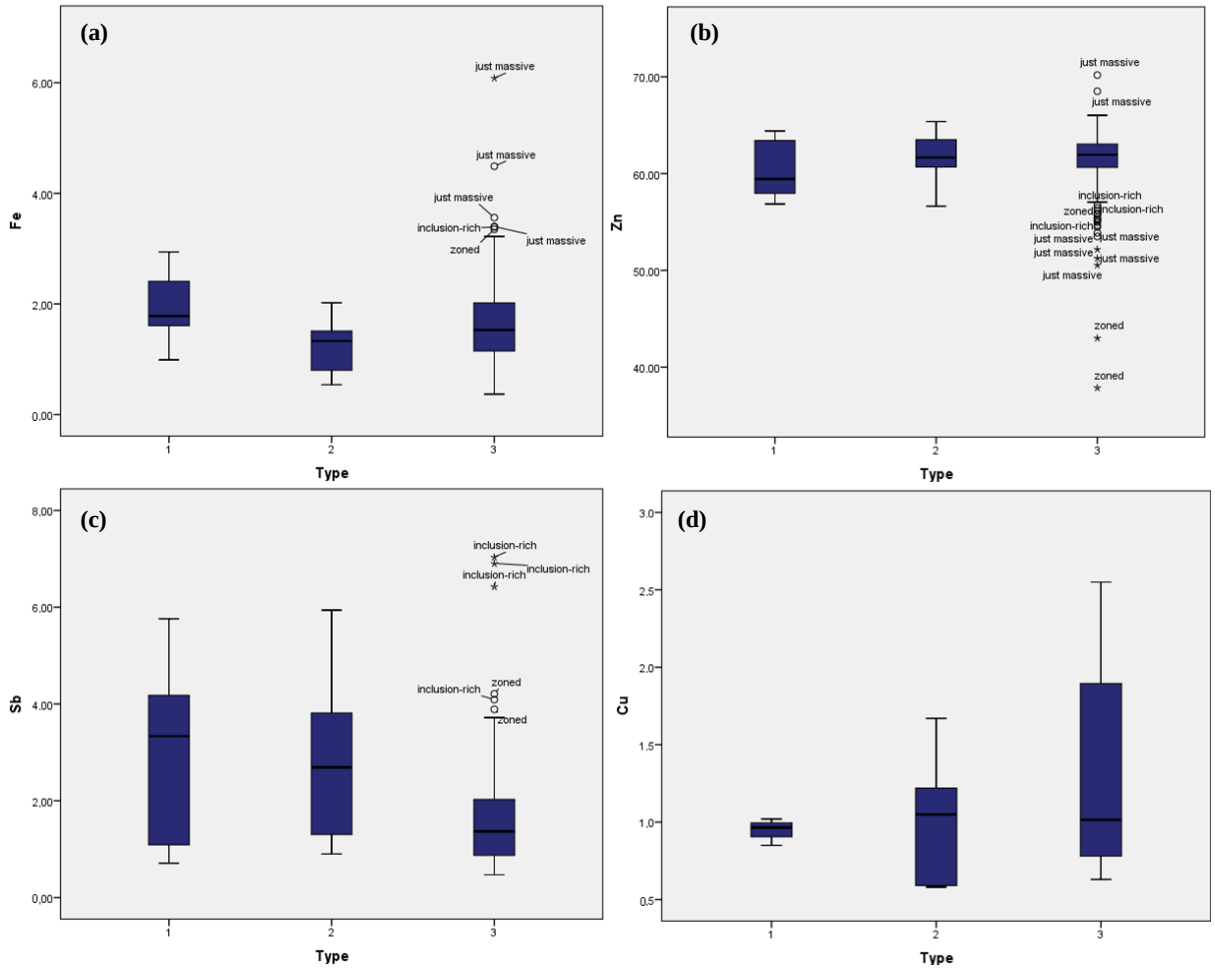

Figure 74. Box-whisker plot showing the concentration of (a)Fe, (b) Zn, (c) Sb, (d) Cu in each sphalerite type. Boxes represent the 25th and 75th data percentiles, whiskers represent the 10th and 90th percentiles, and symbols represent outliers (outside the 10th and 90th percentiles). The horizontal line in each box represents the median.

7.2. Trace elements in sphalerite: element substitution versus micro-, and/or nano-inclusions

The spatial distribution of trace metals within sulfide host phases may result from the presence of nano- or micro inclusions of phases hosting specific trace metals (**Deditius et al. 2011**), and/or, stoichiometric or non-stoichiometric substitution of trace metals into the host sphalerite (**see Wohlgemuth-Ueberwasser et al. 2015, and references therein; Maslennikov et al. 2009**).

Figure 75 shows a dendrogram that is based on statistical correlation of all the EDS data **(Appendix, Tables 1-6)** obtained from Kolumbo sphalerites; the dendrogram was constructed in order to investigate the clustering of elements into groups according to similarity levels. The elements are clustered into two main groups, group 1 and group 2 (similarity level >54%). Group 1 is subdivided into 2 subgroups: subgroup 1 includes Fe and Zn with similarity level 62 % and subgroup 2 includes Cd and Hg with similarity level 74 %. The second group includes Sb, Pb, Cu, Ag and As with similarity level ≥60%. These relationships suggest distinctive processes of element incorporation in the various sphalerite phases:

(1) The association of Zn with Fe coupled by variable and erratic relationships in binary plots **(Figs. 34a, 44, 64, 68)** may imply an influence from the established substitution mechanism $(Zn^{2+})\leftrightarrow(Fe^{2+})$ **(e.g. Cook et al. 2009)**, as well as complex relationships between other trace metals (e.g. Sb, Cd, Cu, and Ag) and Zn) (see **Figs. 69, 70, 71, 72**).

(2) The association of Hg with Cd is difficult to interpret with the available analytical resolution. However, this association combined with elemental EDS mapping which reveals a strong and systematic co-variation of Hg and Cd along different growth zones of type 1 sphalerite **(Fig. 33)**, and in micron-scale particulate inclusions within type 3 sphalerite that are visible in BSE images (Fig. 63, 67), may be interpreted as follows: (i) Direct substitutions of divalent cations as $Zn^{2+}\leftrightarrow(Hg^{2+}, Cd^{2+})$ **(c.f. Grammatikopoulos et al. 2006, Cook et al. 2009)** along certain growth zones that are intercalating more Zn enriched zones, in primary colloform type 1 sphalerite **(Fig. 33)**; these variations in trace element chemistry probably reflect variable solubility of Hg and Cd, during primary type 1 sphalerite growth due to changes in the physicochemical parameters of the discharging parental fluid phase **(cf. Maslennikov et al. 2009, Revan et al. 2014, Wohlgemuth-Ueberwasser et al. 2015, Keith et al. 2016)**. Homogeneous distribution of sulfosalt nanoparticles of Hg and Cd in type 1

sphalerite is less possible; and (ii) incorporation of sulfosalt micro-particles of Hg and Cd in sphalerite 3 following dissolution-reprecipitation mechanisms. Concerning Hg-Cd sulfosalts, these are very rare in nature (**Vasil'ev, 2011)**; all the varieties are complex isomorphous mixtures of the ZnS–HgS solid solution series in the natural system Zn–Hg–Cd–S. We speculate that if the Hg-Cd correlation and covariation shown in **Figures 33, 62, 63, 75** is originated by Hg-Cd sulfosalts, they may be part of this natural series (**Vasil'ev 2011)**.

(3) The Cu-Ag-As-Sb-Pb association **(Fig. 74)** may be interpreted as an expression of the incorporation of these elements in crystalline type 2 and 3 sphalerite as micro-, and/or nano-inclusions of galena–tetrahedrite–tennantite (galena–'fahlore') associations [PbS─$(Cu,Ag)_{10}(Fe,Zn)_2(As,Sb)_4S_{13}$] **(Cook et al. 2009, Maslennikov et al. 2009, Pfaff et al. 2011)**; galena inclusions visible in BSE images are widespread **(Fig. 73 d, h).** Such galena–'fahlore'associations are not evident in BSE elemental maps of type 1 sphalerite **(Fig. 33)**. This explanation is verified by the spiky fluctuating concentration patterns of Cu, Sb, As and Ag, coupled by the strong covariation of these elements, displayed in geochemical profile across a subhedral type 3 sphalerite crystal **(Fig. 59) (Wohlgemuth-Ueberwasser et al. 2015, Keith et al. 2016)**. The above interpretations are in agreement with the work of **Cook et al. (2009)** who found elevated As and Sb concentrations in sphalerite from different ore deposits, and **Pfaff et al. (2011)** who found positively correlated As+Sb+Cu+Ag in sphalerite, which they attributed to micro-inclusions of tetrahedrite–tennantite. Moreover, these interpretations conform to **Taylor & Radtke (1969)** and **Kelley et al. (2004)** who presume that certain trace element contents like Ag, Cu, Pb, and Sb are present as submicroscopic inclusions of galena, chalcopyrite and/or tetrahedrite in sphalerite. Alternatively, the statistically significant Pb-As-Sb association of **Figure 75**, combined with a strong co-variation of Pb and Sb in micron-scale particulate inclusions in sphalerite 3 **(Fig. 61)**, may be interpreted as a mark of inclusions of the jordanite–geocronite ($Pb_{14}(As,Sb)_6S_{23}$) solid solution series **(Pfaff et al. 2011)**.

With special reference to Ag that this thesis puts emphasis on, recent work has shown that Ag exhibits a dual character, either as microscopic Ag-bearing mineral inclusions (i.e. tetrahedrite-tennantite) in sphalerite as well as substituted in the lattice (as Ag^+) **(Cook et al. 2009, Ciobanu et al. 2011, Murakami & Ishihara 2013)**. Consequently, the strong co-variation between Ag and Sb along geochemical profiles in sphalerite 2 and **3 (Figs. 42, 59, 60)** can also be explained by coupled substitution in the sphalerite lattice: $2Zn^{2+} \leftrightarrow Ag^+ + Sb^{3+}$, alongside nano-scale inclusions of Ag–Sb-bearing tetrahedrite-tennantite. This is supported by **Cook et al. (2009)** who remarked that a general coupled substitution mechanism would

result in monovalent cation enrichment (i.e. Ag^{+}) in sphalerite, with respective tri- and tetravalent cation enrichments (e.g., Sb^{3+}, Ga^{3+}, In^{3+}, As^{3+}, and Ge^{4+}).

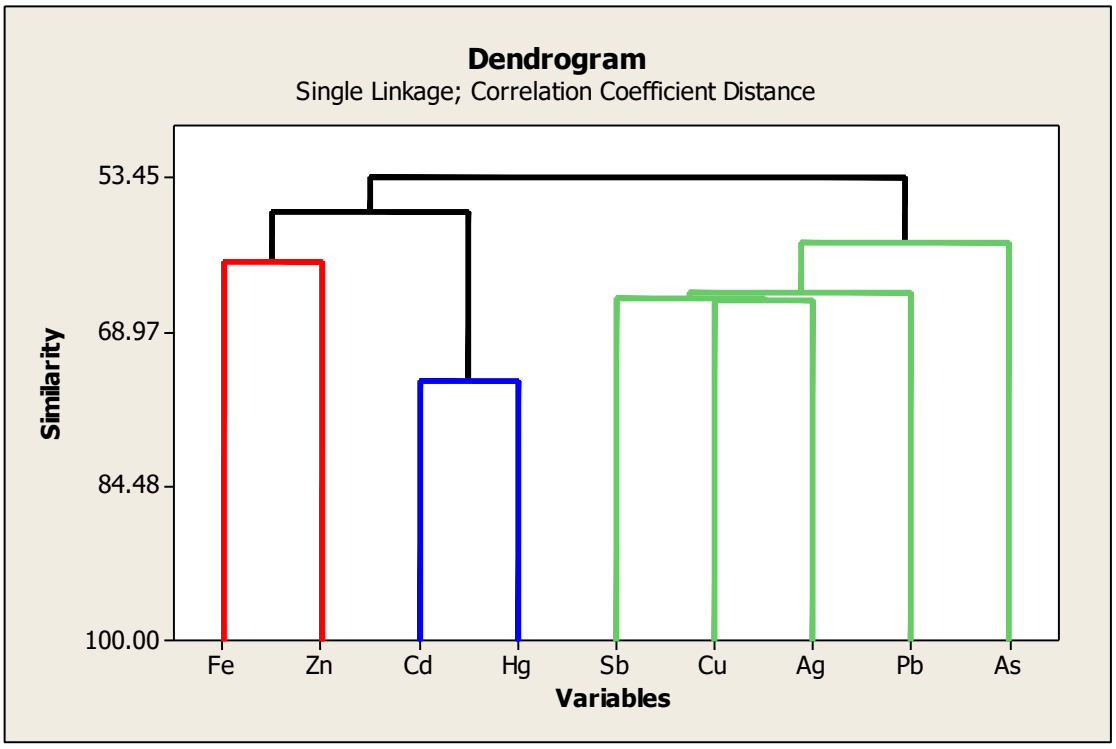

Figure 75: Dendrogram based on statistical correlation of the elements contained in Kolumbo sphalerite samples clustered into two main groups with similarity level >54%. The first group is subdivided into 2 subgroups: subgroup 1 includes Fe and Zn (similarity 62 %) and subgroup 2 includes Cd and Hg (similarity level 74 %). The second group includes Sb, Pb, Cu, Ag and As with similarity level 60%.

7.3 Genetic considerations

The composition and character of massive sulfides forming in the submarine environment is controlled by a complex array of factors and processes **(Herzig et al. 1993, Tivey 1995, Saunders & Brueseke 2012, Monecke et al. 2014, Wohlgemuth-Ueberwasser et al. 2015, Maslennikov et al. 2009, Keith et al. 2016)**:

(1) The character of the host rocks to the hydrothermal vent system and the geological setting;

(2) Water depth of sulfide formation, and subseafloor boiling, a process influencing the composition and metal transport capacity of hydrothermal fluids;

(3) Fluid–seawater mixing within the chimney wall and during fluid discharge that causes significant variations in metal solubility due to changes in temperature, pH, redox conditions, salinity and ligand availability within the parental fluid phase that may enhance metal and trace element solubilities in the fluid phase;

(4) Input of magmatic volatiles (CO_2); magmatic volatiles may provide an important metal source for submarine hydrothermal systems and elements such as Au, As, Sb, Hg, Ag, Tl, Ag can be transported by such a volatile phase;

(5) The nature and physicochemical conditions of sulfide precipitation within seafloor hydrothermal edifices (i.e. chimneys etc);

(6) The proportions of coexisting minerals which control of trace element incorporation; and

(7) The extent of modification of trace metal distribution in chimney sulfides due to dissolution–reprecipitation processes within the vent edifices during later stage hydrothermal activity.

7.3.1. Mechanisms of sphalerite precipitation

Unless otherwise noted the following synthesis stems from **Boyce et al. (2015)**. Mechanisms of deposition of sphalerite depend largely on the nature of the complexation: chloride complexation ($ZnCl^+$, $ZnCl_2^0$, $ZnCl_3^-$, and $ZnCl_4^{2-}$; 400ºC to 25 ºC) and bisulfide complexation ($Zn(HS)_2^0$, $Zn(HS)_3^-$, $Zn(HS)_4^{2-}$, and $Zn(OH)(HS)^0$; 25 and 350°C depending on fluid composition and temperature). The species $ZnCl^+$ and $ZnCl_2^0$ are considered to be the most important at elevated temperatures, whereas for temperatures and pH relevant to hydrothermal systems, the two most important bisulfide species are $Zn(HS)_2^0$ and $Zn(HS)_3^-$; the prevalence boundary for these two species increases from a pH of 4.6 at 100°C to 8.1 at 350°C.

Precipitation mechanisms can be expressed in terms of the following two generalized reactions:

$$ZnCl_n^x + H_2S^- = ZnS + 2H^+ + nCl^- \quad (1)$$

$$Zn(HS)_n^x + (-x)H^+ = ZnS + (n-1)H_2S \quad (2)$$

where x = 2-n.

The precipitation of sphalerite could result from a variety of mechanisms depending on the Zn speciation. The latter is largely governed by four things: (1) Cl^- and (2) ΣS concentrations in the fluid, (3) fluid pH, and (4) fluid temperature.

(1) For chloride complexes (higher mCl^- and lower mΣS and pH), sphalerite precipitation could result from an increase in pH (Reaction 1, **Fig. 76**), and/or an increase in the concentration of reduced sulphur (HS^-), potentially due to fluid mixing or dissolution of sulfur from rocks, could also lead to sphalerite precipitation (see below) **(Fig. 76)**. In many hydrothermal systems, pH values are less than neutral, favoring Reaction 1.

(2) For bisulfide complexes, oxidation of reduced sulfur to sulfate would drive Reaction 2 to the right and result in sphalerite precipitation. Moreover, decrease in pH would lead to sphalerite precipitation at low pH.

(3) Cooling may also cause sphalerite precipitation **(Fig. 76)**. Based on **Figure 76** at a pH of 4, the solubility of sphalerite decreases from ~650 ppm to ~10 ppm over the temperature interval 300 to 150°C in a fluid with a salinity of 12 wt % and mΣS = 0.05 (i.e., 98.5 % of the Zn in solution would be precipitated).

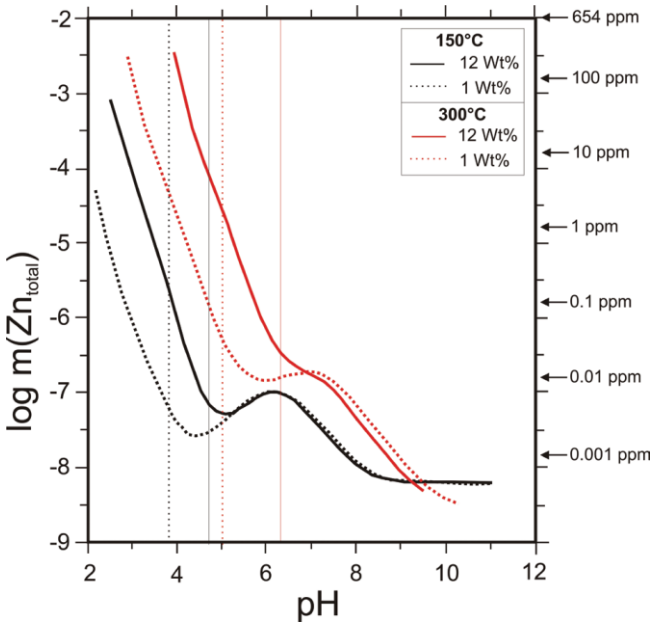

Figure 76. The solubility of sphalerite as a function of pH for 1 and 12 wt % NaCl fluids at 150 and 300°C and mΣS = 0.05. The thin vertical lines represent the boundary between the predominance of chloride species (to the left of the lines) and bisulphide species. It is clear from this figure that sphalerite solubility is significantly higher at low pH, where chloride species predominate. If Zn is transported under such conditions, it can be seen that its solubility will significantly decrease if the fluid undergoes a decrease in temperature or increase in pH, potentially resulting in precipitation of sphalerite. After Tagirov & Seward (2010).

7.3.2 Effects of phase separation and metal complexation on sphalerite composition

As it has already been stated, water depth is one of the main controls on the metal content of sulfide precipitates in modern seafloor hydrothermal systems in arc-related settings **(Monecke et al. 2014)**. Kolumbo hosts one of the shallowest hydrothermal systems in subduction-related settings that are hosted by active arc volcanoes **(c.f. Monecke et al. 2014)** where modern seafloor Hg- and Ag-bearing sphalerite formation occurs at ~500 mbsl along with other sulfides. Consequently, phase separation of CO_2-rich hydrothermal fluids occurs in the Kolumbo subseafloor (see **Kilias et al. 2013)** because the ambient hydrostatic pressure is insufficient to prevent boiling of the mineralizing fluids, during their ascent to the seafloor

and during seafloor venting. Thus, subseafloor boiling of the hydrothermal fluids is a key process for sphalerite deposition and trace metal enrichment, because it may control the maximum fluid temperature, influence fluid chemistry (pH) and metal-transport capacity (e.g., **Monecke et al. 2014, *and references therein*)**.

(1) Because decompression of boiling fluids during fluid ascent to the seafloor is accompanied by significant cooling, boiling will affect sphalerite solubility and hence deposition. Despite the fact that high Zn (and Pb) grades are found at a wide range of water depths, it is generally assumed that in the case of shallow marine vent sites these high grades are explained in part by deposition at lower temperatures (e.g., 150°−250°C: **Large 1992, Hannington et al. 1995**).

(2) In addition to temperature, the aqueous solubility of Zn and other base and precious metals is influenced by the concentrations of complexing ligands (chloride complexes or bisulfide complexes) and fluid acidity, both of which change during boiling as dissolved gases partition into the vapor phase, thus causing sphalerite deposition **(Fig. 76) (Drummond & Ohmoto 1985, Bischoff & Rosenbauer 1987, Foustoukos & Seyfried 2007)**.

(3) We believe that the enrichment of primary colloform type 1 sphalerite in Hg (and by inference Ag, Sb) is also due to subseafloor boiling that contributes to a relative enrichment of the epithermal suite of elements (ESE) (Hg, Ag, Au, As, Sb, Tl, Ag, and Sb) in lower temperature sulfides forming in shallow marine vents **(cf. Hannington et al. 1999)**. Such a process is supported by recent work that suggests ESE enrichment to result from their similar volatile behaviour in subduction systems **(Saunders & Brueseke 2012)**; previous studies revealed that subduction zonemagmas are volatile rich and oxidized compared to mid-ocean ridge magmas **(Huston et al. 2011, de Ronde et al. 2007)** and degassing of such magmas releases significant amounts of metals **(Williams-Jones & Heinrich 2005, Simon & Ripley 2011, Scher et al. 2013)**. In addition, the results of **Wohlgemuth-Ueberwasser et al. (2015)** and **Monecke et al. (2014)** also indicate that the composition of hydrothermal sulfides is affected by sub-seafloor phase separation.

(4) The involvement of fluid-seawater mixing on sphalerite precipitation is supported by colloform textures that indicate disequilibrium conditions that are interpreted to be the result of rapid crystallization due to mixing between hydrothermal fluid and ambient seawater **(Xu & Scott 2005, Berkenbosch et al. 2012, Keith et al. 2016)**.

In agreement with previous studies we conclude that fluid temperature variations, phase separating processes and possibly variable amounts of fluid-seawater mixing represent important variables controlling the distribution of Hg and Ag (and by inference Au, As, Sb,

Tl, Ag, and Sb) in Kolumbo's sphalerite and associated sulfides deposits **(Maslennikov et al. 2009, Revan et al. 2014, Wohlgemuth-Ueberwasser et al. 2015, Keith et al. 2016)** and the observed variations in the crystallization sequence and texture of sphalerite can be attributed to fluid–seawater mixing within the chimney wall and during fluid discharge that causes significant variations in metal solubility due to changes in temperature, pH and redox conditions within the parental fluid phase **(Herzig et al., 1993, Tivey 1995)**. Systematic trace element variations along growth zones within sphalerite crystals **(Fig. 33)** probably resemble such variations in a geochemical way **(Wohlgemuth-Ueberwasser et al. 2015)**.

7.4 Environmental considerations

Enrichments of polymetallic hydrothermal chimneys in Hg and Ag (As, Sb, Pb, Cd, Cu, Zn, Fe), among the biggest ever reported from the world' oceans, have been discovered in the hydrothermal vent field located on the floor of the density-stratified acidic (pH~ 5) crater of the Kolumbo shallow-submarine arc-volcano, near Santorini **(Kilias et al. 2013)**. These results indicate that volcanic CO_2-rich fluids venting onto Kolumbo's of shallow (<2 km water depth) crater seabed cause local seawater acidification, and contain high concentrations of bioessential trace metals (i.e. Fe, Cu, Zn) and trace metal and metalloid emergent global pollutants such as Hg, Ag as well as As, Sb, and Tl. The observed metal enrichment have significant implications for toxic metal (i.e. Tl, Sb, As, Hg, Ag) transport and biogeochemical cycling in seafloor hydrothermal systems, and underscores the importance of Kolumbo's submarine volcanic and geothermal activity as a potential source of toxic metals to: (1) microbial metabolism, (2) marine phytoplankton cell growth and marine food webs, and, (3) in areas exploited by fishing such that Kolumbo ~12 miles NE of Santorini. It is not known how common the type of polymetallic Hg-Ag-rich deposit studied here may be in the submarine volcanoes of the Kolumbo line, along the CSK tectonic line **(Nomikou et al. 2012)**. Given the significant role that the Christianna-Santorini-Kolumbo (CSK) tectonic line plays for the region's morphology, volcanism, hydrothermal activity, and seismicity, the hazardous release of potentially toxic metals into the water column may be tied to the earthquake cycle in that highly touristic Santorini island.

Formation of methylmercury (CH_3Hg^{2+}) and dimethylmercury [$(CH_3)_2Hg^0$]would be favored by high concentrations of dissolved C, which is a likely scenario for Kolumbo given the high organic matter content of the chimneys **(Kilias et al. 2013)**, as in aquatic

environments microbes are the main agents controlling methylmercury production (**Gilmour et al. 1992**, **Compeau & Bartha 1985**, **King et al. 1999)**. If this would happen, living organisms would accumulate methylmercury which is biomagnified through the food chain (**Monteiro et al. 1996**).

8. Conclusions

1. Mercurian (Hg) and argentiferous (Ag) sphalerite was detected for the first time in the Hellenic Volcanic Arc, in shallow seafloor (~500 mbsl) hydrothermal vent edifices (i.e. chimneys, mounds etc.) of the active hydrothermal vent system of Kolumbo shallow-submarine arc-volcano. Rare stibnite and an unidentified non-stoichiometric Zn-sulfide phase were also detected, for the first time.
2. The bulk trace metal enrichment of Hg and Ag in the chimneys is controlled by the modal abundance of sphalerite and its modifications that accompany the course of dissolution–reprecipitation processes during evolving hydrothermal activity and chimney growth.
3. Kolumbo sphalerite occurs in three textural varieties, interpreted as a result of increasing maturity following dissolution–reprecipitation processes within the vent edifices during hydrothermal evolution of the chimney mineralogy. They are designated as Types 1 to 3, and represent different generations which in order of increasing maturity are: i) Type1: microglobular and zoned colloform sphalerite, ii) Type 2: sphalerite with porous core and massive rim and iii) Type 3: inclusion-rich and compositionally zoned massive sphalerite.
4. Mercury (Hg) correlates closely with Cd in sphalerite and the distribution of Hg in sphalerite is probably controlled by: (i) Direct substitutions of divalent cations as $Zn^{2+} \leftrightarrow (Hg^{2+}, Cd^{2+})$ along systematic growth zones in primary colloform type 1 sphalerite, possibly due to variable solubility of Hg during sphalerite growth due to changes in the physicochemical parameters of the discharging fluid phase; and, (ii) inclusions of sulfosalt micro-particles of Hg and Cd in sphalerite 3 following dissolution-reprecipitation mechanisms; these particles which are visible in BSE images, probably represent solid inclusions of the ZnS–HgS solid solution series incorporated in sphalerite.
5. Silver (Ag) correlates with Cu-As-Sb-Pb. Its distribution is controlled by micro-, and/or nano-inclusions of galena–tetrahedrite–tennantite (galena–'fahlore') associations [$PbS{-}(Cu,Ag)_{10}(Fe,Zn)_2(As,Sb)_4S_{13}$]. Moreover, the strong co-variation between Ag and Sb along geochemical profiles in sphalerite 2 and 3 can also be explained by coupled

substitution in the sphalerite lattice: $2Zn^{2+} \leftrightarrow Ag^{+} + Sb^{3+}$, alongside nano-scale inclusions of Ag–Sb-bearing tetrahedrite-tennantite.

6. We conclude that fluid temperature variations, boiling subseafloor and during venting processes and possibly variable amounts of fluid-seawater mixing represent important variables controlling the distribution of Hg and Ag in the submarine hydrothermal systems and associated sulfide deposits.

References

Amos H.M., Jacob D.J., Streets D.G., Sunderland E.M., 2013. Legacy impacts of all-time anthropogenic emissions on the global Hg scale. Global Biogeochemical Cycles. 27:1–12

Angelier J., 1979. Neotectonique de l' arc Egeen. These de doctorat d' Etat, Soc. Geol. Nord., No 3, 418p

Archibald S. M., Migdisov A. A., Williams-Jones A. E., 2001. The stability of Au–chloride complexes in water vapor at elevated temperatures and pressures. Geochim. Cosmochim. Acta 65(23):4413–4423

Archibald S. M., Migdisov A. A., Williams-Jones A. E., 2002. An experimental study of the stability of copper chloride complexes in water vapor at elevated temperatures and pressures. Geochim. Cosmochim. Acta 66(9):1611–1619

Armellini F. J. & Tester J. W., 1993. Solubility of sodium chloride and sulfate in sub- and supercritical water vapor from 450–550 ˚C and 100–250 bar. Fluid Phase Equilib. 84:123–142

Audetat A., Günther D., Heinrich C. A., 1998 Formation of a magmatic-hydrothermal ore deposit: insights with LA-ICP-MS analysis of fluid inclusions. Science 279(5359):2091–2094

Audetat A., Günther D., Heinrich C. A., 2000a. Magmatic- hydrothermal evolution in a fractionating granite: a micro-chemical study of the Sn–W–F-mineralized Mole granite (Australia). Geochim. Cosmochim. Acta 64(19):3373–3393.

Audetat A., Günther D., Heinrich C., 2000b. Causes for large-scale metal zonation around mineralized plutons: fluid inclusion LA-ICP-MS evidence from the Mole Granite, Australia. Econ. Geol. 8(December):1563–1581.

Axelrad D.A., Bellinger D.C., Ryan L.M., Woodruff T.J., 2007. Dose-response relationship of prenatal mer- cury exposure and IQ: an integrative analysis of epidemiologic data. Environ. Health Perspect. 115:609–15

Barkay T., & Irene W.D., 2005. “Microbial Transformations of Hg: Potentials, Challenges, and Achievements in Controlling Hg Toxicity in the Environment.” Advances in Applied Microbiology 57 (SUPPL. A):1–52

Barnes H.L. 1997. Geochemistry of Hydrothermal Ore Deposits, 3rd ed. Wiley, New York

Barriada J.L., Tappin A.D., Hywel Evans E., Achterberg E.P., 2007. Dissolved Silver Measurements in Seawater. TrAC Trends in Analytical Chemistry 26(8):809–17

Barrie C.D., Boyce A.J., Boyle A.P., Williams P.J., Blake K., Lowther J.M., McDermott P., Wilkinson J.J., Prior D.J., 2009, On the growth of colloform textures: A case study of

sphalerite from the Galmoy ore body, Ireland: Journal of the Geological Society of London, v. 166, p. 463-483

Barton Jr. P. B. & Bethke P. M., 1987, Chalcopyrite disease in sphalerite: pathology and epidemiology. Am. Miner. 72, 451– 467

Bur'yanova E.Z., 1960. The mineralogy and geochemistry of cadmium in sedimentary rocks in Tuva. Geokhimiya 2:177–182

Beaudoin G., 2000. Acicular sphalerite enriched in Ag, Sb, and Cu embedded within colour banded sphalerite from the Kokanee Range, BC. Can. Mineral. 38, 1387–1398

Belissont R., Boiron M. C., Luais B., Cathelineau M., 2014. LA-ICP-MS analyses of minor and trace elements and bulk Ge isotopes in zoned Ge-rich sphalerites from the Noailhac - Saint-Salvy deposit (France): Insights into incorporation mechanisms and ore deposition processes. Geochimica et Cosmochimica Acta, 126: 518–540

Belzile N., Chun-Yan L., Yu-Wei C., Mohui W., 2008. "The Competitive Role of Organic Carbon and Dissolved Sulfide in Controlling the Distribution of Hg in Freshwater Lake Sediments." The Science of the total environment 405(1-3):226–38

Benn T.M., & Westerhoff P., 2008. Nanoparticle silver released into water from commercially available sock fabrics. Environ Sci Technol 42:4133–4139

Bernhoft R.A., 2012. Hg toxicity and treatment: a review of the literature. J Environ Public Health. 2012:460508

Berkenbosch H.A., De Ronde C.E.J, Gemmell J.B., et al. 2012. Mineralogy and formation of black smoker chimneys from brothers submarine volcano, Kermadec Arc. Econ Geol 107:1613–1633. doi: 10.2113/econgeo.107.8.1613

Bianchini A., Bowles K.C., Brauner C.J., Gorsuch J.W., Kramer J.R., Wood C.M., 2002. Evaluation of the effects of reactive sulfide on the acute toxicity of silver (i) to Daphnia magna. Part 2: Toxic results. Environ Toxicol Chem 21:1294–300

Bischoff J., Rosenbauer R., Pitzer K., 1986. The system NaCl– H2O: relations of vapor–liquid near the critical temperature of water and of vapor–liquid–halite from 300˚ to 500 ˚C. Geochim. Cosmochim. Acta 50(7):1437–1444

Bischoff J. L. & Rosenbauer R. 1987 Phase separation in seafloor geothermal systems: an experimental study on the effects of metal transport. Amer. J. Sci. 287:953-978

Boyce A.J., Barrie C.D., Samson I.M., and Williams-Jones A.E., 2015. Current perspectives on zinc deposits. S. M. Archibald & S. J. Piercey (Eds.). Dublin: Irish Association for Economic Geology

Broussard L.A., Hammett-Stabler C.A., Winecker R.E., Ropero-Miller J.D., 2002. The toxicology of Hg. Lab Med. 33:614–625

Bull S. HPA compendium of chemical hazards: inorganic Hg/elemental Hg. Environment Protection Agency Reports, 2011. Available from: http://www.hpa.org.uk/webc/HPAwebFile/ HPAweb_C/1194947406874. Accessed March 14, 2014.

Cabri L.J., Campbell J.L., Laflamme J.H.G., Leigh R.G., Maxwell J.A. Scott J.D., 1985. Proton-microprobe analysis of trace elements in sulfides from some massive-sulfide deposits. Can. Mineral. 23, 133–148

Carey S., Bell, K.L.C., Nomikou P., Vougioukalakis G., Roman C.N., Cantner K., Bejelou K., Bourbouli M., Martin J.F., 2011. Exploration of the Kolumbo Volcanic Rift Zone. In: Bell, K.L.C., Fuller, S.A. (Eds.), New frontiers in ocean exploration: The E/V Nautilus 2010 field season. Oceanography 24 (1), pp. 24–25

Carey S., Nomikou P., Croff-Bell K., Lilley M., Lupton J., Roman C., Stathopoulou E., Bejelou K., Ballard R., 2013. CO2 degassing from hydrothermal vents at Kolumbo submarine volcano, Greece and the accumulation of acidic crater water. Journal of Geochemical Exploration 20, 223-302

Carey S. et al., Exploration of the Kolumbo Volcanic Rift Zone. In Bell, K. L. C. & Fuller, S. A. eds. New Frontiers in Ocean Exploration: The E/V Nautilus 2010 Field Season. Oceanography 24(1)

Chen W. W., Zhang J. M., Ardell A. J.. Dunn B., 1988. Solid- state phase equilibria in the ZnS–CdS system. Technical Report No. 1, UCLA, Dept. of Materials Sci. Eng.

Childress J.J., & Fisher C.R., 1992. The biology of hydrothermal vent animals: physiology, biochemistry, and autotrophic symbioses. Oceanogr. Mar. Biol. 30: 337–441

Choi, S.C., Chase, T., Bartha R., 1994. Enzymatic catalysis of Hg methylation by Desulfovibrio desulfuricans LS. Applied Environmental Microbiology, 60: 1342–1346

Christianson E.M., Keeler G., Landis M.S., 2008. Near-field Hg deposition during summertime precipitation events: the impact of coal fired utilities. Eos Trans. AGU 89: Fall Meet. Suppl. Abstr. A53D– 0316

Çiftçi E., 2009. Mercurian sphalerite from Akoluk (Ordu, NE Turkey): Hg as cathodo-luminescence activator. Mineral. Mag. 73 (2): 257–267

Ciobanu C.L., Cook N.J., Utsunomiya S., Pring A., Green L., 2011. Focussed ion beam–transmission electron microscopy applications in ore mineralogy: bridging micro- and nanoscale observations. Ore Geol. Rev. 42: 6–31

Clark A. H.,1970. Arsenian sphalerite from Mina Alcarán, Pampa Larga, Copiapó , Chile. Am. Mineral. 55: 1794–1797

Clarkson T., Cranmer J., Sivulka D., Smith R., 1984. Hg health effects update: health issue assessment. Environment Protection Agency Reports

Colaço A., Bustamante P., Fouquet Y., Sarradin P. M., Serrão-Santos R., 2006. "Bioaccumulation of Hg, Cu, and Zn in the Azores Triple Junction Hydrothermal Vent Fields Food Web." Chemosphere 65 (11):2260–67

Comm. Toxicol. Eff. MethylHg, Board Environ. Stud. Toxicol., Comm. Life Sci., US Natl. Res. Counc. 2000. Toxicological Effects of MethylHg.Washington, DC: Natl. Acad

Compeau G.C., & Bartha R., 1985. Sulfate-reducing bacteria: principal methylators of Hg in anoxic estuarine sediment. Appl. Environ. Microbiol. 50:498–502

Cook Nigel J. et al., 2009. "Trace and Minor Elements in Sphalerite: A LA-ICPMS Study." Geochimica et Cosmochimica Acta 73 (16):4761–91

Cooke D. R. & Simmons S. F., 2000. Characteristics and genesis of epithermal gold deposits. Econ. Geol. Rev. 13, 221–244

Cooper C.F., & Jolly W.C., 1970. Ecological effects of silver iodide and other weather modification agents: A review. Water Resour Res 6: 88–98

Cossa D., Martin J.M., Takayanagi K., Sanjuan J., 1997. The distribution and cycling of Hg species in the western Mediterranean. Deep Sea Res. Part II 44:721–40

CPM Group., 1995. CPM Group's Silver Survey 1995. New York, NY, USA

Craig J. R., 1973. The Cu–Zn–S system. Mineral. Deposita 8: 81– 91

Cronan D.S., & Varnavas S.P., 2001. Metalliferous sediments off Milos, Hellenic volcanic Arc. Explor Min Geol 8:289–297

Dai Z.X., Sheng J.F., Bai Y., 2005. Distribution and Potentiality of Lead and Zn Resources in the World. Earthquake Publishing (in Chinese)

Dando P. R., Steben D., Varnavas S. P., 1999. Hydrothermalism in the Mediterranean Sea. Prog. Oceanogr., 44333–367

de Ronde C.E. et al., 2002. Discovery of active hydrothermal venting in Lake Taupo, New Zealand. Journal of Volcanology and Geothermal Research 115:257-275

de Ronde C. E., Massoth, G. J., Baker, E. T., Lupton, J. E., 2003. Submarine hydrothermal venting related to volcanic arcs. Volcanic, geothermal and ore-forming fluids: Rulers and witnesses of processes within the Earth

Deer W.A., Howie R.A., Zussman J., 1992, The rock forming minerals. Mineralogical Society of Great Britain & Ire- land; 3rd edition edition, 510pp

Dekov V.M., & Savelli C., 2004. Hydrothermal activity in the SE Tyrrhenian Sea: an overview of 30 years of research. Mar. Geol. 204:161–185

Dekov M., Bindi L., Burgaud G., Petersen S., Asael D., Rédou V., Fouquet Y., Pracejus B.,

2013. Inorganic and biogenic As-sulfide precipitation at seafloor hydrothermal fields Vesselin Marine Geology 342:28–38

Deditius A.P., Utsunomiya S., Reich M., Kesler S.E., Ewing R.C., Hough S.E., Walshe J. 2011. Trace metal nanoparticles in pyrite. Ore Geology Reviews, 42:32–46

Dewey J.F., Pitmann W.C., Ryan W.B.F., Bonnin J., 1973. Plate tectonics and the evolution of the Alpine system. Bulletin of the Geological Society of America 84:3137–3180

Di Benedetto F., Bernardini G.P., Costagliola P., Plant D., Vaughan D.J., 2005. Compositional zoning in sphalerite crystals. Am. Mineral. 90:1384–1392

Dickson E. W. & Tunell G., 1968. Hg and antimony deposits associated with active hot springs in the western U.S.A. In: Ore Deposits of the United States. 1933-1967 (Graton-Sales Volume), (Ed. J. D. Ridge), 1675-1700. N.Y. Amer. Inst. Mining Metal. Petroleum Eng.

Dill H.G., Garrido M.M., Melcher F., Gomez M.C., Weber B., Luna L.I. Bahr A., 2013. Sulfidic and non-sulfidic indium mineralization of the epithermal Au–Cu–Zn–Pb–Ag deposit San Roque (Provincia Rio Negro, SE Argentina)—with special reference to the "indium window" in zinc sulfide. Ore Geology Reviews, 51:103-128.

Dominey-Howes D., Papadopoulos G., Dawson A., 2000. Geological and historical investigation of the 1650 Mt. Columbo (Thera Island) eruption and tsunami, Aegean Sea, Greece. Nat. Hazards 21:83–96

Drummond S.E. & Ohmoto H., 1985. Chemical evolution and mineral deposition in boiling hydrothermal systems. Econ. Geol., 80:126-147

Einaudi M.T., Hedenquist J.W., Inan E.E., 2003. Sulfidation state of fluids in active and extinct hydrothermal systems: Transitions from porphyry to epithermal environments: Society of Economic Geologists Special Publication 10, p. 285–313

Emsley J., 1991. The Elements, 2nd ed., p. 116–117. Clarendon Press, Oxford

Erickson R.J., Brooke L.T., Kahl M.D., Vende Venter F., Harting S.L., Markee T.P., et al., 1998. Effects of laboratory test conditions on the toxicity of silver to aquatic organisms. Environ Toxicol Chem 17:572–8

Etris S., 1997. Silver and silver alloys. In Howe-Grant M, ed, Kirk– Othmer Encyclopedia of Chemical Technology, 4th ed, Vol 22, John Wiley & Sons, New York, NY, USA, pp 163–179

Fabrega J., Luoma S. N., Tyler C. R., Galloway T. S., Lead J. R., 2011. Silver Nanoparticles : Behaviour and Effects in the Aquatic Environment. Environment International 37(2): 517–31

Fein J. B., & Williams-Jones A. E., 1997. The role of Hg-organic interactions in the hydrothermal transport of Hg. Economic Geology, 92(1): 20-28

Fisher C.R., 1990. Chemoautotrophic and methanotrophic symbioses in marine-invertebrates. Rev. Aquat. Sci. 2 (3–4), 399–436

Fisher N.S., & Wang W.X., 1998. Trophic transfer of silver to marine herbivores: a review of recent studies. Environ Toxicol Chem 17:562–71

Fitzgerald W.F., & Lamborg C.H., 2005. Geochemistry of Hg in the environment. In Treatise on Geochemistry, ed. BS Lollar, pp. 107–48. New York: Elsevier

Fisher N.S. & Wente M., 1993. The release of trace elements by dying marine phytoplankton. Deep-Sea Res. I, 40(4): 671-694

Fouque F., 1879. Santorin et ses eruptions. Masson et Cie, Paris

Foustoukos D.I., & Seyfried W.E., 2007. Fluid Phase Separation Processes in Submarine Hydrothermal Systems. In: Liebscher, A., Christoph, C.A. (Eds.), Fluid–Fluid Interactions, Reviews inMineralogy and Geochemistry. Min. Soc. Am. 65:213–233

Francesconi K. A., & Edmonds J. S., 1993. Arsenic in the sea In A.D Ansell, R.N. Gibson and M. Barnes Eds., Oceanogr. Mar. Biol. Annu. Rev., 31: 111–151

Friedli H.R., Radke L.F., Prescott R., Hobbs P.V., Sinha P., 2003.Hg emissions from the Aug 2001 wildfires in Washington State and an agricultural waste fire in Oregon and atmospheric Hg budget estimates. Global Biogeochemical Cycles. 17:1039–1047.

Fytikas M., 1977. Geological and geothermal study on Milos Island. Geol. and Geophys. Studies, IGME, 17, 1 (228 pp)

Gaffney J.S. & Marley N.A., 2014. In-depth review of atmospheric Hg: sources, transformations, and potential sinks. Energy and Emission Control Technologies 2014:2 1–21

Gallon C. & Flegal A. R., 2014. Sources , Fluxes , and Biogeochemical Cycling of Silver in the Oceans. (D. M. Whitacre, Ed.) Reviews of Environmental Contamination and Toxicology Volume (Vol. 235). Switzerland

Galobardes J. F., Van Hare D. R., Rogers L. B., 1981. Solubility of sodium chloride in dry steam. J. Chem. Eng. Data 26(4):363–366

Gamaletsos P. et al., 2013. “Geological Sources of As in the Environment of Greece: A Review.” 1–37.

Geranio L., Heuberger M., Nowack B., 2009. The behavior of silver nanotextiles during washing. Environ Sci Technol 43:8113–8118.

Gill G.A., & Fitzgerald W.F., 1988. Vertical Hg distributions in the oceans: Geochimica et Cosmochimica Acta 52:1719–1728.

Gill G.A., Bloom N.S., Cappellino S., Driscoll C.T., Dobbs C., et al., 1999. Sediment-water fluxes of Hg in Lavaca Bay, Texas. Environ. Sci. Technol. 33:663–69

Gilmour C.C., Henry E.A., Mitchell R., 1992. Sulfate stimulation of Hg methylation in freshwater sediments. Environ. Sci. Technol. 26:2281–87

Glasby G. P., Iizasa K., Hannington M., Kubota H., Notsu K., 2008. Mineralogy and composition of Kuroko deposits from northeastern Honshu and their possible modern analogues from the Izu-Ogasawara (Bonin) Arc south of Japan: Implications for mode of formation. Ore Geology Reviews 34:247-560

Gottschalk F., Sonderer T., Scholz R.W., Nowack B., 2009. Modeled environmental concentrations of engineered nanomaterials (TiO2, ZnO, Ag, CNT, fullerenes) for different regions. Environ Sci Technol 43(24):9216–9222

Goulding G.R., Kelly C.A., Sparling R., Loewen P.C., Rudd J.W.M., Barkay T., 2002. Evidence for facilitated uptake of Hg(II) by Vibrio anguillarum and Escherichia coli under anaerobic and aerobic conditions. Limnology and Ocean- ography, 47, 967–975

Gousgouni M., 2014. Antimony fixation in solid phases at the hydrothermal field of Kolumbo submarine volcano (Santorini): deposit model and environmental implications. Unpublished M.Sc. thesis, National and Kapodistrian University of Athens, Greece. 108pp.

Grammatikopoulos T.A.,& Roth T,. 2002. Mineralogical characterization and Hg deportment in field samples from the Polymetallic Eskay Creek Deposit, British Columbia, Canada. Int. J. Surf. Min. Recl. 16:180–195

Grammatikopoulos T.A., Valeyev O., Roth T., 2006. Compositional variation in Hg-bearing sphalerite from the polymetallic Eskay Creek deposit, British Columbia, Canada. Chem. Erde – Geochem. 66:307–314

Gray J.E., Hines M.E., Higueras P.L., Adatto I., Lasorsa B.K., 2004. Hg speciation and microbial transformations in mine wastes, stream sediments, and surface waters at the Almadén mining district, Spain. Environmental Science and Technology, 38:4285–4292

Gustin M.S., Biester H., Kim C.S., 2002. Investigation of the light-enhanced emission of Hg from naturally enriched substrates. Atmos. Environ. 36:3241–54

Haitzer M., Ryan J., Aiken G.R., 2002. Binding of Hg (II) to DOM: the role of Hg(II) to DOM concentration ratio. Environmental Science and Technology, 36:3564–3570

Halbach P., et al., 1989. Probable modern analogue of Kuroko-type massive sulfide deposits in the Okinawa Trough back-arc basin. Nature 338:496-499

Halbach P., Pracejus B., Märten A., 1993. Geology and mineralogy of massive sulfide ores from the central Okinawa Trough, Japan: Economic Geology and the Bulletin of the Society of Economic Geologists, 88:2210–2225

Hannington M.D., 2014, 13.18 - Volcanogenic Massive Sulfide Deposits, in Turekian, K.K., and Holland, H.D. (Eds), Treatise on Geochemistry (Second Edition): Elsevier, Oxford, p. 463- 488

Hannington M. D., de Ronde C. D. J., Petersen, S., 2005. Sea-floor tectonics and submarine hydrothermal systems In: Economic Geology 100th Anniversary Volume., ed. by Hedenquist J. W., Thompson J. F. H., Goldfarb R. J. and Richards J. P. Society of Economic Geologists, Littelton, Colorado, USA, pp. 111-141

Hannington M. et al., 2001. First observations of high-temperature submarine hydrothermal vents and massive anhydrite deposits off the north coast of Iceland. Mar. Geol. 177:199–220

Hannington M.D., Jonasson I.R., Herzig P.M., Petersen, S., 1995. Physical and chemical processes of seafloor mineralization at mid-ocean ridges: Geophysical Monograph 91:115–157

Hannington M.D., Poulsen K.H., Thompson J.F.H., Sillitoe R.H., 1999. Volcanogenic gold in the massive sulfide environment: Reviews in Economic Geology 8:325–356

Harada M., 1995. Minamata disease: methylHg poisoning in Japan caused by environmental pollution. Crit. Rev. Toxicol. 25:1–24

Hazen R. M., Golden J., Downs R. T., Hystad G., Grew E. S., Azzolini D., Sverjensky D. A., 2012. Hg (Hg) mineral evolution: A mineralogical record of supercontinent assembly, changing ocean geochemistry, and the emerging terrestrial biosphere. American Mineralogist, 97(7):1013-1042

Hein J.R., Koschinsky A., McIntyre B.R., 2005. Hg- and silver-rich ferromanganese oxides, Southern California borderland; deposit model and environmental implications Economic Geology and the Bulletin of the Society of Economic Geologists. 100(6):1151-1168

Heinrich C. A., Driesner T., Stefánsson A., Seward T. M., 2004. Magmatic vapor contraction and the transport of gold from the porphyry environment to epithermal ore deposits. Geology 32(9):761

Henley R. W. & McNabb A., 1978. Magmatic vapor plumes and ground-water interaction in porphyry copper emplacement. Econ. Geol. 73(1):1–20

Herzig P.M., 1988. A mineralogical, geochemical and thermal profile trough the Agrokipia "B" hydrothermal sulfide deposit, Troodos Ophiolite Complex, Cyprus, in Friedrich, G.H., and Herzig, P.M., eds., Base metal sulfide deposits: Berlin, Heidelberg, Springer-Verlag, p. 182–215

Herzig P.M., Hannington M.D., Fouquet Y., von Stackelberg U., Petersen S., 1993. Goldrich sulfides from the Lau Back arc and implications for the geochemistry of gold in sea-floor hydrothermal systems of the Southwest Pacific. Econ. Geol. 88: 2182–2209

Herzig P.M. & Hannington M.D., 1995, Polymetallic massive sulfides at the modern seafloor - A review: Ore Geology Reviews. 10: 95-115

Hesterberg D., Chou J.W., Hutchinson K.J., Sayer D.E., 2001. Bonding of Hg(II) to reduced organic sulfur in humic acid as affected by S/Hg ratio. Environmental Science and Technology, 35:2741–2745

Hill W.R., 1941. Argyria: the pharmacology of silver. South Med J. 34:340. Hogstrand

Hogstrand C., & Wood C.M., 1998. Toward a better understanding of the bioavailability, physiology and toxicity of silver in fish: implications for water quality criteria. Environ Toxicol Chem 17:547–61

Hübscher C., Ruhnau M., Nomikou P., 2015. Volcano-tectonic evolution of the polygenetic Kolumbo submarine volcano/Santorini (Aegean Sea). Journal of Volcanology and Geothermal Research. 291:101-111

Huebner A., Rahder E., Rahnera S., Halbach P, Varnavas S.P., 2004. Geochemistry of hydrothermally influenced sediments off Methana (western Hellenic volcanic arc). Chem Erde-Geochem 64:75–94

Huston D.L., Sie S.H., Suter G.F., Cooke D.R., Both R.A., 1995. Trace elements in sulfide minerals from eastern Australian volcanic-hosted massive sulfide deposits: Part I. Protonmicroprobe analyses of pyrite, chalcopyrite, andsphalerite, and Part II. Selenium levels in pyrite: comparisonwith δ34S values and implications for the source of sulfur in volcanogenic hydrothermal systems. Econ. Geol. 90:1167–1196

Huston D. L., Jablonsky W., Sie S. H. 1996. The distribution and mineral hosts of silver in Eastern Australian volcanogenic massive sulfide deposits. Can. Mineral. 34:529–546

Huston D.L., Relvas J.M.R.S., Gemmell J.B., Drieberg S., 2011. The role of granites in volcanic-hosted massive sulfide ore-forming systems: an assessment of magmatic–hydrothermal contributions. Mineral. Deposita 46:473–507

Iizasa K. et al., 1999. A Kuroko-Type polymetallic sulfide deposit in a submarine silicic caldera. Science 283:975-977

Iizasa K., Sasaki M.,Matsumoto K., Shiokawa S., Tanahashi M., on-board scientists., 2004. A first extensive hydrothermal field associated with Kuroko-type deposit in a silicic caldera in a nascent rift zone, Izu-Ogasawara (Bonin), Japan. Oceans '04 MTS/IEEE Techno-Ocean '04 November 9–12, 2004 Kobe, Japan, pp. 991–996

Janes N., & Playle R.C., 1995. Modeling silver binding to gills of rainbow trout (Oncorhynchus mykiss). Environ Toxicol Chem 14: 1847–1858

Jayasekera R. & Rossbach M., 1996. Use of seaweeds for monitoring trace metals in coastal waters. Environ. Geochem. Health, 18:63–68

Jonasson I.R. & Sangster D.F., 1974. Variations in the Hg content of sphalerite for some Canadian sulphide deposits, *in* Proceedings of the Fifth International Geochemical Exploration Symposium, Geochemical Exploration 1974, Developments in Economic Geology, I.L. Elliott and W.K. Fletcher, eds., Association of Explotation Geochemists, Special Publication No. 2, p. 313-331

Kati M., Voudouris P., Valsami-Jones E., et al. 2015. Cinnabar , arsenian pyrite and thallium-enrichment in active shallow submarine hydrothermal vents at Paleochori Bay , Milos Island , Greece. 17:13046.

Kearey P., Klepeis K. A. Vine F., 2009. Global Tectonics (3rd ed), 482 pp. (Wiley-Blackwell, John Wiley & Sons, West Sussex UK)

Keeler G.J., Landis M.S., Norris G.A., Christianson E.M., Dvonch J.T., 2006. Sources of Hg wet deposition in eastern Ohio, USA. Environ. Sci. Technol. 40:5874–81

Keith M., Häckel F., Haase K.M., Schwarz-Schampera U., Klemd R., 2016. Trace element systematics of pyrite from submarine hydrothermal vents. Ore Geology Reviews. 72(1):728–745, doi:10.1016/j.oregeorev.2015.

Keith M., Haase K.M., Schwarz-Schampera U., Klemd R., Petersen S., Bach W., 2014. Effects of temperature, sulfur, and oxygen fugacity on the composition of sphalerite from submarine hydrothermal vents. Geology 42:699–702. doi:10.1130/G35655.1.

Kelley K. D., Leach D. L., Johnson C. A., Clark J. L., Fayek M., Slack J. F., Anderson V. M., Ayuso L. E., Ridley W. I., 2004. Textural, compositional, and sulfur isotope variations of sulfide minerals in the Red Dog Zn–Pb–Ag deposits, Brooks Range, Alaska: implications for ore formation. Econ. Geol. 99:1509–1532

Kharbish S., 2007. A Raman Spectroscopic Investigation of Fe-Rich Sphalerite: Effect of Fe-Substitution. Physics and Chemistry of Minerals 34(8):551–58

Kilias S.P. et al., 2013. "New Insights into Hydrothermal Vent Processes in the Unique Shallow-Submarine Arc-Volcano, Kolumbo (Santorini), Greece." Scientific reports 3:2421

King J.K., Saunders F.M., Lee R.F., Jahnke R.A., 1999. Coupling Hg methylation rates to sulfate reduction rates in marine sediments. Environ. Toxicol. Chem. 18:1362–69

King J.K., Kostka J.E., Frischer M.E., Saunders F.M., 2000. Sulfate-reducing bacteria methylate Hg at variable rates in pure culture and in marine sedi- ments. Applied Environmental Microbiology, 66:2430–2437

Klein D.A. & Mulvey G., 1978. Amounts of silver-derived agents used in weather modification in relation to contributions from other sources. In: Klein, D.A. (Ed), Environmental impacts of artificial ice nucleating agents. Colorado State University, pp. 5-8

Krabbenhoft D.P., Branfireun D.P., Heyes A., 2005. Biogeochemical cycles affecting the speciation, fate and transport of Hg in the environment. In M.B. Parsons and J.B. Percival, Eds., Hg: Sources, Measurements, Cycles, and Effects, Short Course, 34: 139–156. Mineralogical Association of Canada, Québec

Krauskopf K. B., 1951. Physical chemistry of quicksilver transportation in vein fluids. Econ. Geol. 46:498-523

Kritee K., Blum J.D., Barkay T., 2008. Hg stable isotope fractionation during reduction of Hg(II) by different microbial pathways. Environmental Sci- ence and Technology, 42: 9171–9177

Kritee K., Barkay T., Blum J.D., 2009. Mass dependent stable isotope fraction- ation of Hg during mer mediated microbial degradation of monomethyHg. Geochimica et Cosmochimica Acta, 73: 1285–1296

Kucha H., 1988, Biogenic and nonbiogenic concentration of sulfur and metals in the carbonate-hosted Ballinalack Zn-Pb deposit, Ireland: Miner- alogy and Petrology, 38:171–187.

Kucha H., Schroll E., Raith J. G., Halas S., 2010. Microbial sphalerite formation in carbonate-hosted Zn-Pb ores, Bleiberg, Austria: Micro- to nanotextural and sulfur isotope evidence. Economic Geology, 105(5):1005–1023

Kucha H., Van der Biest J., Viaene W. A., 1990, Peloids in stratabound Zn-Pb deposits and their genetic importance: Mineralium Deposita, 25: 132–139

Kucha H., & Viaene W., 1993, Compounds with mixed and intermediate sulfur valences as precursors of banded sulfides in carbonate-hosted Zn-Pb deposits in Belgium and Poland: Mineralium Deposita, 28:13–21.

Lamborg C.H., Fitzgerald W.F., Damman A.W.H., Benoit J.M., Balcom P.H., Engstrom D.R., 2002. Modern and historic atmospheric Hg fluxes in both hemispheres: global and regional Hg cycling implications. Glob. Biogeochem. Cycles 16:1104–14

Lamborg C.H., Fitzgerald W.F., O'Donnell J., Torgerson T., 2009. A non-steady-state compartmental model of global-scale Hg biogeochemistry with interhemispheric atmospheric gradients. Geochim. Cosmochim. Acta 66:1105–18

Large R.R., 1992.Australian volcanic-hosted massive sulfide deposits: Fea- tures, styles, and genetic models: Economic Geology, 87:471–510

Laurier F.J.G., Mason R.P., Gill G.A., Whalin L., 2004. Hg distributions in the North Pacific Ocean— 20 years of observations. Mar. Chem. 90:3–19

Leal-Acosta M. L., Shumilin E., Mirlean N., Delgadillo-Hinojosa F., Sánchez-Rodríguez I., 2013. The impact of marine shallow-water hydrothermal venting on arsenic and Hg accumulation by seaweed Sargassum sinicola in Concepcion Bay, Gulf of California. Environmental Science: Processes & Impacts, 15(2):470-477

LeBlanc G.A., Mastone J.D., Paradice A.P., Wilson B.F., Lockhart H.B. Jr, Robillard K.A., 1984. The influence of speciation on the toxicity of silver to the fathead minnow (Pimephales promelas). Environ Toxicol Chem 3:37–46

Lee S., Kim S. J., Ju S. J., Pak S. J., Son S. K., Yang J., Han, S., 2015. Hg accumulation in hydrothermal vent mollusks from the southern Tonga Arc, southwestern Pacific Ocean. Chemosphere, 127:246-253

Lehmann B., Mao J., Ma D., 2004. Extreme metal enrichment in early Cambrian sulfide-rich black shale in south China: a seawater model [Abstract]. Geological Society of America Abstracts with Programs, 36:199

Le Pichon X., & Angelier J., 1979.The Hellenic Arc and Trench system: A key to the neotectonic evolution of the Eastern Mediterranean area. Tectonophysics 60:1–42

Li Y.H. & Schoonmaker J.E., 2004. Chemical composition and mineralogy of ma- rine sediments. In F.T. MacKenzie, Ed., Sediments, Diagenesis, and Sedimentary Rocks, 7, p. 1–36. Treatise on Geochemistry, Elsevier, Amsterdam

Lindberg S.E., Kim K.H., Meyers T.P., Owens J.G., 1995. Micrometeorological gradient approach for quantifying air/surface exchange of Hg-vapor: tests over contaminated soils. Environ. Sci. Technol. 29:126–35

Lockhart H.B., 1983. Silver compounds. In Grayson M, ed, Kirk– Othmer Encyclopedia of Chemical Technology, 2nd ed, Vol 21, John Wiley & Sons, New York, NY, USA, pp 16–32

Lockington J.A., Cook N.J., Ciobanu C.L., 2014. Trace and minor elements in sphalerite from metamorphosed sulphide deposits. Mineralogy and Petrology, 108(6):873-890

Luoma S.N., Ho Y.B., Bryan G.W., 1995. Fate, bioavailability and toxicity of silver in estuarine environments. Mar. Pollut. Bull. 31:44-54

Luoma S.N., 2008. Silver nanotechnologies and the environment: old problems and new challenges? Washington DC: Woodrow Wilson International Center for Scholars or The PEW Charitable Trusts.

Luoma S.N., Rainbow P.S., 2008. Metal contamination in aquatic environments: science and lateral management. Cambridge: Cambridge University Press

Marani M.P., Gamberi F., Savelli C., 1997.Shallow-water polymetallic sulfide deposits in the Aeolian island arc. Geology 25:815–818

Marsh D.O., Clarkson T.W., Cox C, Myers G.J., Amin-Zaki L., Al-Tikriti S.A.A., 1987. Fetal methylHg poisoning. Relationship between concentration in single strands of maternal hair and child effects. Arch. Neurol. 44:1017–22

Martins I., Costa V., Porteiro F., Cravo A., Santos R.S., 2001. Hg concentrations in invertebrates from Mid-Atlantic Ridge hydrothermal vent fields. J. Mar. Biol. Assoc. UK 81:913–915

Maslennikov V. V., Maslennikova S. P., Large R. R., Danyushevsky L. V., 2009. Study of trace element zonation in vent chimneys from the Silurian Yaman-Kasy volcanic-hosted massive sulfide deposit (Southern Urals, Russia) using laser ablation-inductively coupled plasma mass spectrometry (LA-ICPMS). Economic Geology, 104(8):1111-1141.

Mason R.P., Fitzgerald W.F., 1993. The distribution and biogeochemical cycling of Hg in the equatorial Pacific Ocean. Deep Sea Res. Part I 40:1897–924

Mason R.P., Fitzgerald WF, Morel FMM., 1994. The biogeochemical cycling of elemental Hg: anthropogenic influences. Geochim. Cosmochim. Acta 58:3191–98

Mason R.P., Rolfhus K.R., Fitzgerald W.F., 1998. Hg in the North Atlantic. Mar. Chem. 61:37–53 142

Mavrogenes J., Henley R., Reyes A., Berger B. R., 2010. Sulfosalt melts: evidence of high-temperature vapor transport of metals in the formation of high-sulfidation lode gold deposits. Econ. Geol. 105:257–262

McKenzie D.P., 1972. Active tectonics of the Mediterranean region Geophys. Journal of the Royal Astronomical Society 30:109–185

Mergler D., Anderson H.A., Chan L.H.M., Mahaffey K.R., Murray M., et al., 2007. MethylHg exposure and health effects in humans: a worldwide concern. Ambio: A J. Hum. Environ. 36:3–11

Miedaner M. M., Migdisov A. A., Williams-Jones A. E., 2005. Solubility of metallic Hg in octane, dodecane and toluene at temperatures between 100°C and 200°C. Geochimica et Cosmochimica Acta, 69(23): 5511–5516

Migdisov A. A., Williams-Jones A. E., Suleimenov O. M., 1999. Solubility of chlorargyrite (AgCl) in water vapor at elevated temperatures and pressures. Geochim. Cosmochim. Acta 63(22):3817–3827

Migdisov A. A. & Williams-Jones A. E., 2013. A Predictive Model for Metal Transport of Silver Chloride by Aqueous Vapor in Ore-Forming Magmatic-Hydrothermal Systems. Geochimica et Cosmochimica Acta 104:123–35

Monecke T., Petersen S., Hannington M.D. 2014. Constraints on Water Depth of Massive Sulfide Formation: Evidence from Modern Seafloor Hydrothermal Systems in Arc-Related Settings. Econ Geol 109:2079–2101. doi: 10.2113/econgeo.109.8.2079

Monperrus M., Tessier E., Point D., Vidimova K., Amouroux D., et al., 2007. The biogeochemistry of Hg at the sediment–water interface in the Thau Lagoon. 2. Evaluation of Hg methylation potential in both surface sediment and the water column. Estuar. Coast. Shelf Sci. 72:485–96

Monteiro L.R., Costa V., Furness R.W., Santos R.S., 1996. Hg concentrations in prey fish indicate enhanced bioaccumulation in mesopelagic environments. Mar. Ecol. – Progr. Ser. 141: 21–25

Morel F.M.M., Kraepiel A.M.L., Amyot M., 1998. The chemical cycle and bioaccumulation of Hg. Annu. Rev. Ecol. Syst. 29:543–66

Morford J. L., Kalnejais L. H., Reinard M., 2008. Geochemical Cycling of Silver in Marine Sediments along an Offshore Transect. Marine Chemistry 110(1):77–88

Muntean J. L., Cline J. S., Simon A. C., Longo A. A., 2011. Magmatic-hydrothermal origin of Nevada's Carlin-type gold deposits. Nat. Geosci. 4:122–127

Murakami H., & Ishihara S., 2013. Trace elements of Indium-bearing sphalerite from tin-polymetallic deposits in Bolivia, China and Japan: A femto-second LA-ICPMS study. Ore Geology Reviews, 53:223–243

Navarro E., Baun A., Behra R., Hartmann N.B., Filser J., Miao A.J., et al., 2008. Environmental behavior and ecotoxicity of engineered nanoparticles to algae, plants, and fungi. Ecotoxicology 17:372–386.

Ndung'u K., Thomas M., Flegal A., 2001. Silver in the western equatorial and south Atlantic Ocean. Deep-Sea Research, Part II: Topical Studies in Oceanography, 48: 2933-2945.

Ninkovich D., & Hays J.D., 1972. Mediterranean island arcs and origin of high potash volcanoes. Earth and Planetary Science Letters 16:331–345

Nomikou P., Papanikolaou D., Alexandri M., Sakellariou D., Rousakis G., 2013. "Submarine Volcanoes along the Aegean Volcanic Arc." Tectonophysics 597-598:123–146

Nriagu J.O., 1993. Legacy of Hg pollution. Nature 363:589

Oftedahl I., 1940. Untersuchungen über die Nebenbestandteile von Erzmineralien norwegischer zinkblendführender Vorkommen. Skrift. Norsk Videnskabs Akademi Oslo, Mathematik-Naturvidenskab Kl 8:1–103

Orberger B., Pasava J., Gallien J.-P., Daudin L., Trocellier P., 2003. Se, As, Mo, Ag, Cd, In, Sb, Pt, Au, Tl, Re traces in biogenic and abiogenic sulfides from Black Shales (Selwyn Basin, Yukon territories, Canada): a nuclear microprobe study. Nucl. Instr. Meth. Phys. Res. B210:441–448

Orihel D.M., Paterson M.J., Gilmour C.C., Bodaly R.A.D., Blanchfield P.J., et al., 2006. Effect of loading rate on the fate of Hg in littoral mesocosms. Environ. Sci. Technol. 40:5992–6000

Ozerova N.A., Rusinov V.L., Ozerov Y.K., 1975. The Hg in sulfide deposits emplaced in volcanic suites. Miner. Deposita 10:228–233

Pacyna J., Wilson S., Steenhuisen F., Pacyna E., 2005. Spatially distributed inventories of global anthropogenic emissions of Hg to the atmosphere

Pacyna E.G., Pacyna J.M., Sundseth K., et al., 2010. Global emission of Hg to the atmosphere from anthropogenic sources in 2005 and projections to 2020. Atmos Environ. 40:2487–2499

Panyala N.R., Eladia M.P., Josef H., 2008. Silver or Silver Nanoparticles : A Hazardous Threat to the Environment and Human Health ? J. Appl. Biomed. 6:117–129

Parsons M.B. & Percival J.B., Eds. 2005a. Hg: Sources, Measurements, Cycles, and Effects, vol. 34. Short Course, Mineralogical Association of Canada, Québec

Parsons M.B. & Percival J.B., Eds. 2005b. A brief history of Hg and its environmental impact. In M.B. Parsons and J.B. Percival, Eds., Hg: Sources, Measurements, Cycles, and Effects, 34:1–20. , Short Course, Mineralogical Association of Canada, Québec

Peabody C.E., 1993. The association of cinnabar and bitumen in Hg deposits of the California Coast Ranges. In: Parnell, J., Kucha, H., Landais, P. (Eds.), Bitumen in Ore Deposits. Springer, Berlin, pp. 178–209

Perissoratis C., 1995. The Santorini volcanic complex and its relation to the stratigraphy and structure of the Aegean arc, Greece. Mar. Geol. 128:37–58

Petersen S., Herzig P. M., Hannington M. D., Jonasson I. R., Arribas A. Jr., 2002. Submarine Gold Mineralization Near Lihir Island, New Ireland Fore-Arc, Papua New Guinea. Econ. Geol. 97:1795–1813

Petersen S., Monecke T., Westhues A., Hannington M. D., Gemmell J. B., Sharpe R., Kleeberg R., 2014. Drilling shallow-water massive sulfides at the Palinuro volcanic complex, Aeolian island arc, Italy. Economic Geology, 109(8):2129-2158.

Pfaff K., Koenig A., Wenzel T., Ridley I., Hildebrandt L.H., Leach D.L. Markl G., 2011. Trace and minor element variations and sulfur isotopes in crystalline and colloform ZnS: Incorporation mechanisms and implications for their genesis. Chemical Geology, 286(3):118-134.

Phelps D. & Buseck P. R., 1980. Distribution of soil Hg and the development of soil Hg anomalies in the Yellowstone geothermal area, Wyoming Econ. Geol. 75:730-741

Philips D., 1994. Macrophytes as Biomonitors of Trace Elements, in Biomonitoring of coastal waters and estuaries, ed. K. Kramer, CRC Press, Boca Raton, FL, pp. 85–103

Pirrone N., Cinnirella S., Feng X., et al., 2010. Global Hg emissions to the atmosphere from anthropogenic and natural sources. Atmos Chem Phys. 10:5951–5964

Pongprueksa P., Lin C.J., Lindberg S.E., Jang C., Braverman T., et al., 2008. Scientific uncertainties in atmospheric Hg models III: boundary and initial conditions, model grid resolution, and Hg (II) reduction mechanism. Atmos. Environ. 42:1828–45

Price R. E. & Pichler T., 2005. Potential toxicity of shallow-water hydrothermal systems: distribution, speciation and bioavailability of arsenic in Tutum Bay, Ambitle Island, PNG, Chem. Geol., 224:122–135

Radosavljević S. a., Stojanović J. N., Pačevski A. M., 2012. Hg-bearing sphalerite from the Rujevac polymetallic ore deposit, Podrinje Metallogenic District, Serbia: Compositional variations and zoning. Chemie Der Erde - Geochemistry, 72(3):237–244

Radosavljević S. a., Stojanović J. N., Radosavljević-Mihajlović A. S., Vuković N. S., 2016. (Pb–Sb)-bearing sphalerite from the Čumavići polymetallic ore deposit, Podrinje Metallogenic District, East Bosnia and Herzegovina. Ore Geology Reviews, 72:253–268

Rahman M. A., Hageqava H., Lim R. P., 2012. Bioaccumulation, biotransformation and trophic transfer of arsenic in the aquatic food chain. Environ. Res., 116:z118–135

Ranville M.A. & Flegal, A.R., 2005. Silver in the North Pacific Ocean. Geochemistry Geophysics Geosystems, 6(3): Q03M01

Ratte H.T., 1999. Bioaccumulation and toxicity of silver compounds: A review. Environ. Toxicol. Chem. 18(1): 89–108

Reidy B., Haase A., Luch A., Dawson K., Lynch I., 2013. Mechanisms of Silver Nanoparticle Release, Transformation and Toxicity: A Critical Review of Current Knowledge and Recommendations for Future Studies and Applications. Materials, 6(6):2295–2350

Reinfelder J.R., & Chang S.I., 1999. Speciation and Microalgal Bioavailability of Inorganic Silver. Environ. Sci. Technol. 33(11): 1860-1863

Renner H., 1993. Silver, silver compounds and silver alloys. In Elvers B, Hawkins S, Russey W, Schulz G, eds, Ullmann's Encyclopedia of Industrial Chemistry, 5th ed, Vol A24, VCH, Weinheim, Germany.

Revan M.K., Genç Y., Maslennikov V.V., Maslennikov S.P., Large R.R., Danyushevsky L.V., 2014. Mineralogy and trace-element geochemistry of sulfide minerals in hydrothermal chimneys from the Upper-Cretaceous VMS deposits of the eastern Pontide orogenic belt (NE Turkey). Ore Geol. Rev. 63:129–149

Rosenman K.D., Moss A., Kon S., 1979. Argyria: clinical implications of exposure to silver nitrate and silver oxide. J Occup Environ Med. 21:430–435

Roth T., 2002. Physical and chemical constraints on miner- alization in the Eskay Creek deposit, Northwestern British Columbia: Evidence from petrography, mineral chemistry, and sulfur isotopes. Unpublished Ph.D. Thesis, The University of British Columbia, 401pp

Rowland I.R., Robinson R.D., Doherty R.A., 1984. Effects of diet on Hg metabolism and excretion in mice given methylHg: role of gut flora. Arch Environ Health. 39:401–408

Rudnick R. & Gao S., 2003.Composition of the continental crust. In "The Crust", Holland H.D. & Turekian K.K. eds. Treatise on Geochemistry. Elsevier Pergamon, Oxford 3:1-64

Rudnick R.L. & Gao S., 2004. Composition of the continental crust. In R.L. Rud- nick, Ed., The Crust, 3: 1–64. Treatise on Geochemistry, Elsevier, Amsterdam

Ryall W.R., 1979. Hg in Broken Hill (NSW, Australia) lead–zinc–silver lodes. J. Geochem. Explor. 11: 175–194

Rytuba J.J., 2005. Geogenic and mining sources of Hg in the environment. In M.B. Parsons and J.B. Percival, Eds., Hg: Sources, Measurements, Cycles, and Effects, 34: 21–41. Short Course, Mineralogical Association of Canada, Québec

Sanei H., Grasby S.E., Beauchamp B., 2012. Latest Permian Hg anomalies. Geology, 40:63–66

Saunders J. A. & Brueseke M. E., 2012. Volatility of Se and Te during subduction-related distillation and the geochemistry of epithermal ores of the western United States. Econ. Geol. 107:165–172

Sawosz E., Binek M., Grodzik M., Zielinska M., Sysa P., Szmidt M., et al., 2007. Influence of hydrocolloidal silver nanoparticles on gastrointestinal microflora and morphology of enterocytes of quails. Arch Anim Nutr 61:444–51

Scher S., Williams-Jones A.E., Williams-Jones G., 2013. Fumarolic activity, acid-sulfate alteration, and high sulfidation epithermal precious metal mineralization in the crater of Kawah Ijen Volcano, Java Indonesia. Econ. Geol. 108:1099–1118

Scheuhammer A.M., 1987. The chronic toxicity of aluminum, cadmium, Hg, and lead in birds: a review. Environ. Pollut. 46:263–95

Scow K., et al., 1981. Exposure risk assessment for silver. Technical Report. Office of Water, U.S. Environmental Protection Agency, Washington, DC.

SeaBioTech Report., 2013. Seabiotech: 2-Biotech Kolumbo/Santorini/Ierapetra sampling2-10 September 2013 Report

Selin N.E., 2009. “Global Biogeochemical Cycling of Hg: A Review.” Annu. Rev. Environ. Resour 34:43–63

Sherlock R.L., Roth T., Spooner E.T.C., Bray C.J., 1999. Origin of the Eskay Creek precious metal-rich volcanogenic massive sulfide deposit: Fluid inclusion and stable isotope evidence. Econ. Geol. 94, 803–824.

Sigurdsson H., Carey S., Alexandri M., Vougioukalakis G., Croff K., Roman C., Sakellariou D., Anagnostou C., Rousakis G., Ioakim C., Gogou A., Ballas D., Misaridis T, Nomikou P., 2006. Marine Investigations of Greece’s Santorini Volcanic Field. Eos 87. 337-339

Simon A.C., Ripley E.M., 2011. The Role of Magmatic Sulfur in the Formation of Ore Deposits. In: Behrens, H., Webster, J.D. (Eds.), Sulfur in Magmas and Melts. Min. Scoc. Am. 65: 513–564

Smith P.A., & Cronan D.S., 1983. The geochemistry of metalliferous sediments and waters associated with shallow submarine hydrothermal activity (Santorini, Aegean Sea). Chemical Geology 39 (3), 241-262

Stoffers P., Hannington M.D., Wright I., Herzig P., de Ronde C., 1999. Elemental Hg at submarine hydrothermal vents in the Bay of Plenty, Taupo Volcanic Zone, New Zealand. Geology 27 (10), 931– 934

Strode S., Jaegl´e L., Selin N.E., 2009. Impact of Hg emissions from historical gold and silver mining: global modeling. Atmos. Environ. 43:2012–17

Sunderland E.M., & Mason R.P., 2007. Human impacts on open ocean Hg concentrations. Glob. Bio- geochem. Cycles 21:GB4022

Schwartz M.O., 1997. Hg in zinc deposits: economic geology of a polluting element. Int. Geol. Rev. 39:905–992

Hein J. R., Stamatakis M. G., & Dowling J. S. 2000. Trace metal-rich Quaternary hydrothermal manganese oxide and barite deposit, Milos Island, Greece. Applied Earth Science. 109(2):67-76

Tagirov B.R. & Seward T.M., 2010. Hydrosulfide/sulfide complexes of Zn to 250°C and the thermodynamic properties of sphalerite: Chemical Geology 269:301-311

Tarasov V. G., Gebruk A. V., Mironov A. N., Moskalev L. I., 2005. Deep-sea and shallow-water hydrothermal vent communities: two different phenomena? Chem. Geol. 224:5–39

Tauson V.L. & Abramovich M.G., 1980. Hydrothermal study of the ZnS-HgS system. Geochemistry International, v. 72, p. 117-128.

Taylor C. M. & Radtke A. S., 1969 Micromineralogy of silver- bearing sphalerite from Flat River, Missouri. Econ. Geol. 64: 306–318.

Taylor P., Ullrich S. M., Tanton T. W., & Abdrashitova S. A., 2001. Technology Hg in the Aquatic Environment : A Review of Factors Affecting Methylation Hg in the Aquatic Environment : A Review of Factors Affecting Methylation. Critical Reviews in Environmental Science and Technology, 31(3): 241–293

The Silver Institute., 1995. World Silver Survey 1995.Washington, DC, USA.

Tivey M.K., 1995. The influence of hydrothermal fluid composition and advection rates on black smoker chimney mineralogy: Insights from modeling transport and reaction. Geochim. Cosmochim. Acta 59:1933–1949

Tufar W.,1991 Paragenesis of complex massive sulfide ores from the Tyrrhenian Sea. Mitteilungen der Österreichischen Geologischen Gesellschaft 84, 265–300

Tunell G., 1964. Chemical processes in the formation of Hg ores and ores of Hg and antimony. Geochim. Cosmochim. Acta 28. 1019-1037

Tunell G., 1970. Hg: Behavior in magmatogenic processes. In: Handbook of Geochemistry (Ed. H. K. Wedepohl), Section 80-F. Springer

Ulrich T., Günther D., Heinrich C. A., 1999. Gold concentrations of magmatic brines and the metal budget of porphyry copper deposits. Nature 399(6737):676–679

United Nations Environmental Program., 2013. Global Hg Assessment 2013: Sources, Emissions, Releases, and Transport. Geneva, Switzerland: United Nations Environmental Program Chemicals.

Urcell T. Homas W.P and J Ennifer J. P. Eters., 1998. Sources of silver in the enviromnent. Environmental Toxicology and Chemistry 17(4): 539–46.

US Environ. Prot. Agency (EPA)., 2001. Water quality criterion for the protection of human health: methylHg. Rep. EPA-823-R-01-001, US EPA Off. Sci. Technol./Off.Water,Washington, DC

US Environ. Prot. Agency (EPA)., 2007. 2005/2006 National listing of fish advisories. EPA-823-F-07-003 fact sheet. Off. Water, Washington, DC

US Environ. Prot. Agency (EPA)., 2009. Hg: controlling power plant emissions: emissions progress

Valsami-Jones E., Baltatzis E., Bailey E.H., Boyce A.J., Alexander J.L., Magganas A., Anderson L., Waldron S., Ragnarsdottir K.V., 2005, The geochemistry of fluids from an active shallow submarine hydrothermal system: Milos island, Hellenic volcanic arc: Journal of Volcanology and Geothermal Research, v. 148, p. 130–151

Varnavas S.P., & Cronan D.S., 1988. Arsenic, antimony and bismuth in sediments and waters from the Santorini hydrothermal field, Greece. Chem. Geol. 67, 295–305

Varnavas S.P., & Cronan D.S., 1991. Hydrothermal metallogenic processes off the islands of Nisiros and Kos in the Hellenic Volcanic Arc. Marine Geol. 99 (1):109-113

Varnavas S.P., & Cronan D.S., 2005. Submarine hydrothermal activity off Santorini and Milos in the Central Hellenic Volcanic Arc: A synthesis. Chemical Geology 224, 40– 54.

Varekamp J. C. & Buseck P.R., 1981. Hg emissions from Mount St Helens during September 1980. Nature 293, 555-556

Varekamp J.C. & Buseck P.R., 1984. "The Speciation of Hg in Hydrothermal Systems, with Applications to Ore Deposition." Geochimica et Cosmochimica Acta 48(1):177–85

Varekamp J.C. & Buseck P.R., 1986. Global Hg flux from volcanic and geothermal sources. Appl. Geochem. 1:65–73

Vasil'ev V.I. 2011. New data on the composition of metacinnabar and Hg-sphalerite with an isomorphous Cd admixture. Russ Geol Geophys 52:701–708. doi: 10.1016/j.rgg.2011.06.002

Vetriani C., Chew Y.S., Miller S.M., et al., 2005. Hg Adaptation among Bacteria from a Deep-Sea Hydrothermal Vent. Appl Environ Microbiol 71(1):220–26

Voudouris P., et al. 2014. "Silver-Rich Sulfide Mineralization at Vani, Western Milos Island, Greece: New Mineralogical Evidence for Epithermal Ore Deposition in a Shallow

Submarine Environment." In XX Congress of the Carpathian-Balkan Geological Association,.

White D. E., 1967. Hg and base-metal deposits with associated thermal and mineral waters. In: Geochemisrry of Hydrothermal Ore Deposits (ed. H. L. Barnes), 575- 631. Wiley

White D. E., 1981. Active geothermal systems and hydrothermal ore deposits. 75th Ann. Vol. Econ. Geol. 392-423

Wilkinson J.J., 2014, 13.9 - Sediment-Hosted Zinc–Lead Mineralization: Processes and Perspectives, in Turekian, K.K., and Holland, H.D. (Eds), Treatise on Geochemistry (Second Edition): Elsevier, Oxford, p.219-249

Williams-Jones A. E., Migdisov A. A., Archibald S. M., Xiao Z., 2002. Vapor-transport of ore metals. In Water–rock interactions, ore deposits, and environmental geochemistry. A Tribute to David A. Crerar: Geochemical Society Special Publication (eds. R. Hellmann and S.A. Wood). The Geochemical Societ. 7: 279–305

Williams-Jones A. E. & Heinrich C. A., 2005. Vapor transport of metals and the formation of magmatic-hydrothermal ore deposits. Econ. Geol. 100(7):1287–1312.

Wohlgemuth-Ueberwasser C.C., Viljoen F., Petersen S., Vorster C., 2015. "Distribution and Solubility Limits of Trace Elements in Hydrothermal Black Smoker Sulfides: An in-Situ LA-ICP-MS Study." Geochimica et Cosmochimica Acta 159:16–41

Wolfe M.F., Schwarzbach S., Sulaiman R.A., 1998. Effects of Hg on wildlife: a comprehensive review. Environ. Toxicol. Chem. 17:146–60

Woodrow W., 2009. Consumer products inventory Projecton Emerging Nanotechnologies, a project of the Woodrow Wilson International Center for Scholars

Xia K., Skyllberg U.L., Bleam W.F., Bloom P.R., Nater E.A., Helmke P.A., 1999. X-ray absorption spectroscopy evidence for the complexation of Hg(II) by reduced sulfur in soil humic substances. Environmental Science and Technology, 33, 257–261

Xu Q., Scott S.D., 2005. Spherulitic pyrite in seafloor hydrothermal deposits: products of rapid crystallization from mixing fluids. In: Mao J, Bierlein FP (eds) Mineral deposit research: meeting the global challenge, vol 1. Springer, Berlin, 711–713.

Yang K. & Scott S. D., 1996. Possible contribution of a metal- rich magmatic fluid to a sea-floor hydrothermal system. Nature 383, 420–423

Ye L. et al., 2011. "Trace and Minor Elements in Sphalerite from Base Metal Deposits in South China: A LA-ICPMS Study." Ore Geology Reviews 39(4):188–217

Zhang Y., Amakawa H., Nozaki Y., 2001. Oceanic profiles of dissolved silver: precise measurements in the basins of western North Pacific, Sea of Okhotsk, and the Japan Sea. Marine Chemistry, 75(1-2): 151-163

Yin R., Feng X., Li Z., Zhang Q., Bi X., Li G., … Wang J., 2012. Metallogeny and environmental impact of Hg in Zn deposits in China. Applied Geochemistry, 27(1), 151-160

Internet Sources

http://rruff.info

users.metu.edu.tr/lunel/lecture3.doc

Appendix